The structure and spectra of irradiated secondaries in close binaries (pre-CVs)

Dissertation
zur Erlangung des Doktorgrades
des Departments Physik
der Universität Hamburg

vorgelegt von

Alexander Christopher Wawrzyn

aus Hamburg

Hamburg
2009

Gutachter der Dissertation:	Prof. Dr. P.H. Hauschildt
	Prof. Dr. S. Dreizler
Gutachter der Disputation:	Prof. Dr. J.H.M.M. Schmitt
	Prof. Dr. D. Reimers
Datum der Disputation:	26. 03. 2009
Vorsitzender des Prüfungsausschusses:	Dr. R. Baade
Vorsitzender des Promotionsausschusses:	Prof. Dr. R. Klanner
Dekan des Departments Physik:	Prof. Dr. H. Graener

Zusammenfassung:

Viele Sterne entwickeln sich nicht einzeln, sondern gemeinsam mit einem oder mehreren Begleitern. Während die Entwicklung isolierter Sterne theoretisch gut vorhergesagt werden kann, ist die Vorhersage für enge Doppelsterne deutlich schwieriger. Dafür ermöglicht aber gerade diese Doppelstern-Konstellation eine genaue Bestimmung der Größe und Masse. Einer der Mechanismen, von dem man annimmt, dass dadurch enge Doppelsterne enstehen, ist die 'Common Envelope Evolution' (CEE). Besonders junge post-CEE Doppelsterne zeigen z.T. einen Temperaturunterschied von einem Faktor 10 zwischen beiden Komponenten bei nur wenigen Sonnenradien Abstand.

Diese Arbeit konzentriert sich auf enge Doppelsterne, die eine heiße Primärkomponente (z.B. einen Unterzwerg vom Typ O (sdO)) und eine kalte Sekundärkomponente (z.B. einen K/M Hauptreihenstern) enthalten, welche massiv durch die externe Einstrahlung der ersteren beeinflusst wird. Das Verfahren wie die externe Einstrahlung in dem Sternatmosphären Code PHOENIX gehandhabt wird, insbesondere die Änderung der äußeren Randbedingung und der Temperaturkorrekturmethode, wird im Detail beschrieben.

Um den Fokus auf Einstrahlungseffekte zu setzen, werden andere Unwägbarkeiten wie tränenförmige Sterne, Massenakkretion oder Schatten von einer umgebenden Scheibe umgangen, indem pre-kataklysmische Variablen (pre-CVs) aus der Gruppe der engen Doppelsterne als Testobjekte verwendet werden. Das bedeckungsveränderliche System UU Sagittae wird als ein Beispiel für massive Einstrahlung herangezogen und beobachtete optische Spektren werden theoretisch angepasst. Für die Primärkomponente (den sdO) werden Effektivtemperatur, Oberflächenbeschleunigung und eine Abschätzung für die Stickstoffanreicherung an der Oberfläche abgeleitet. Für die Sekundärkomponente werden eine von außen stark beeinflusste Temperaturstruktur, hohe Abweichungen in den Elementhäufigkeiten (besonders für Kohlenstoff und Stickstoff) und starke, induzierte Emissionslinien gefunden, welche auffällig auf Änderungen der Elementhäufigkeiten reagieren und in vergleichbarer Form in V477 Lyrae beobachtet werden.

Da auf einem eingestrahlten Objekt Zonen verschiedener Temperaturen entstehen, welche nicht ausreichend durch ein 1D Modell beschrieben werden können, wird eine Methode präsentiert, die 1D zu quasi 1.5D Modellen verbessert. Diese Methode setzt nur voraus, dass das angestrahlte Objekt als Kugel genähert werden kann, was für pre-CVs hinreichend erfüllt ist. Es wird gezeigt, dass sich für unterschiedliche Einstrahlungswinkel Temperaturen und Ionisationsgrade unterscheiden. Mit einem entsprechend gewichteten 'Patchwork'-Modell können phasenabhängige Spektren erklärt werden.

Abstract:

Many stars evolve not alone but along one or more companions. While the evolution of isolated stars is well predicted by theoretical calculations, close binary systems are on the one hand far more difficult to handle due to their interactions, but on the other hand they are well constrained in their masses and sizes. One mechanism thought to produce such close binaries is the Common Envelope Evolution (CEE). Especially young post-CEE binaries show great temperature differences between both components of about a factor 10 at a separation of a few solar radii.

This work focuses on close binary systems with a hot primary component (e.g. a subdwarf O-type star (sdO)) and a much cooler secondary component (e.g. a main-sequence star), which is heavily influenced by external radiation originating from the first. The technique to include external radiation into the stellar atmosphere code PHOENIX, i.e., the deviation of the outer boundary condition and the change in the temperature correction method, is described in detail.

To concentrate on the irradiation effect, other difficulties such as asymmetric effects due to tear-drop shaped stars, ongoing mass accretion or shadows of a circumbinary disc, are avoided by selecting pre-cataclysmic variables (pre-CVs) out of the class of close binaries as laboratory. The total eclipsing binary system UU Sagittae is used as an example for massive irradiation and observed spectral features in the optical are fitted. For the primary component (the sdO) we constrain the effective temperature, surface gravity and give an estimate for the nitrogen enrichment on its surface. For the secondary component we find a greatly influenced temperature structure, a strong elemental abundance deviation (especially in carbon and nitrogen) and induced strong emission lines, which react unique to the abundance deviation and are comparable in shape to observed emission lines in V477 Lyrae.

Since zones of different temperature can develop on an irradiated star that are not well described by single 1D model, an upgrade from 1D to a quasi 1.5D model is presented as further improvement. This only requires that the irradiated object is reasonably well approximated by a sphere, which is fulfilled for pre-CVs. It is demonstrated that for varying irradiation angles different ionization stages prevail. A proper weighted 'patchwork' can explain phase dependent spectra.

*"The universal aptitude for ineptitude
makes any human accomplishment
an incredible miracle."*

-Col. John P. Stapp's Ironical Paradox

Contents

Chapter 1

Introduction

There is a huge number of stars[1] in the universe, which are themselves only thinly distributed tiny spots in the even more unimaginable infinity of space. Although only very few compared to the wide space, these stars all form inside giant molecular gas clouds and are hence a lot more often found in binary (respectively multiple) systems than one would expect for an equal distribution in space. And, though probably more complex in evolution, this binarity offers a great opportunity to constrain physical parameters very accurately using light curves and radial velocity measurements in the case of close or even eclipsing systems. These methods are not applicable to far-separated binaries, which behave more like single stars.

Most stars are dwarfs[2] and less massive than our Sun, but all intermediate mass stars $(1 - 8 \; M_\odot)$ suffer a similar fate as the Sun at the end of their lifetime: Once there is not enough hydrogen left in the core to fuel the fusion, the hydrogen burning of the star ceases and it leaves the main sequence (MS). Without the radiation pressure there is no longer an equilibrium with the gravitational force and the star collapses until a Fermi-Dirac degenerated electron gas reestablishes the pressure equilibrium.

At this state the remaining material is heated by the contraction to the temperature necessary for hydrogen burning in shells around the core. This restart of fusion in a hydrogen layer removes the degeneracy of the electron gas by inflating the star again, while the core contains inactive helium. Since the luminosity in this post-main sequence phase is higher the inflation by the radiation pressure of the hydrogen shell burning is much greater, thus the star is on the red giant branch (RGB). Once the helium in the core reaches temperatures high enough for fusion (via the triple α reaction) there is a second energy source next to the hydrogen shell burning and the star is on the horizontal branch.

After the star has consumed enough helium in its core a double shell burning of helium and hydrogen initiates on the Asymptotic Giant Branch (AGB) and layers fusion continues in nested shells burning consecutively more massive elements, C , O and so forth. The heaviest element produced by fusion depends on the mass of the star, where a star with $8 - 10 \; M_\odot$ possibly is massive enough to fuse C to Ne and Mg , but not Ne to Fe .

The Herzsprung-Russel (H-R) diagram correlates temperature with luminosity and radius in stellar evolution. This is shown in the illustration 1.1. Illustration 1.2 displays the evolutionary track. The star:

- leaves the main-sequence (H -core exhaustion)

---

[1] Some guesses say at least 70 sextillion $(7 \cdot 10^{22})$ stars.
[2] About 80% of all stars observed are 'low mass stars'.
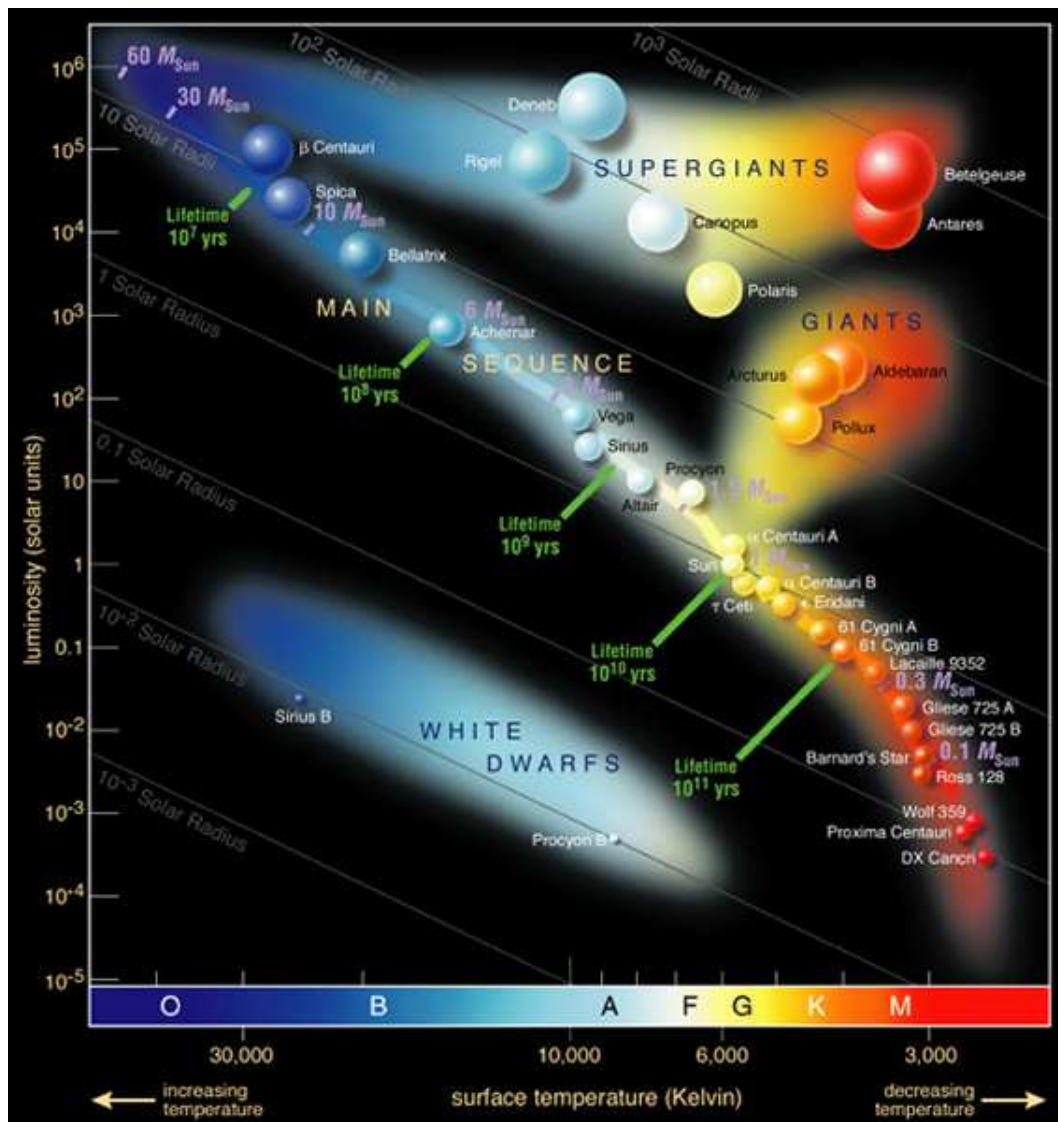
Figure 1.1: Herzsprung-Russel diagram (taken from the homepage of UC Berkeley (cse.ssl.berkeley.edu))

- follows the RGB branch and Horizontal Branch (the 'curl' between RGB and AGB)

- reaches the AGB (which is paralleling the original red giant evolution, but with even faster energy generation, which thus lasts for a shorter time)

- becomes a post-AGB, loses the envelope and becomes a planetary nebula nucleus (a hot subdwarf O- or B-type (sdO/sdB), where the ejected material of the planetary nebula greatly decreases the star's mass left)

- and finally colapses and cools to a white dwarf (if the mass remaining is less than the Chandrasekar mass of 1.4 $M_\odot$).

Figure 1.2: The stellar evolution of intermediate mass stars in the H-R diagramm (illustration from Engels 2005)

At the end of this phase, when the fusion stops and the radiation pressure does no longer compensate the gravitation, the star collapses until the quantum mechanically degenerated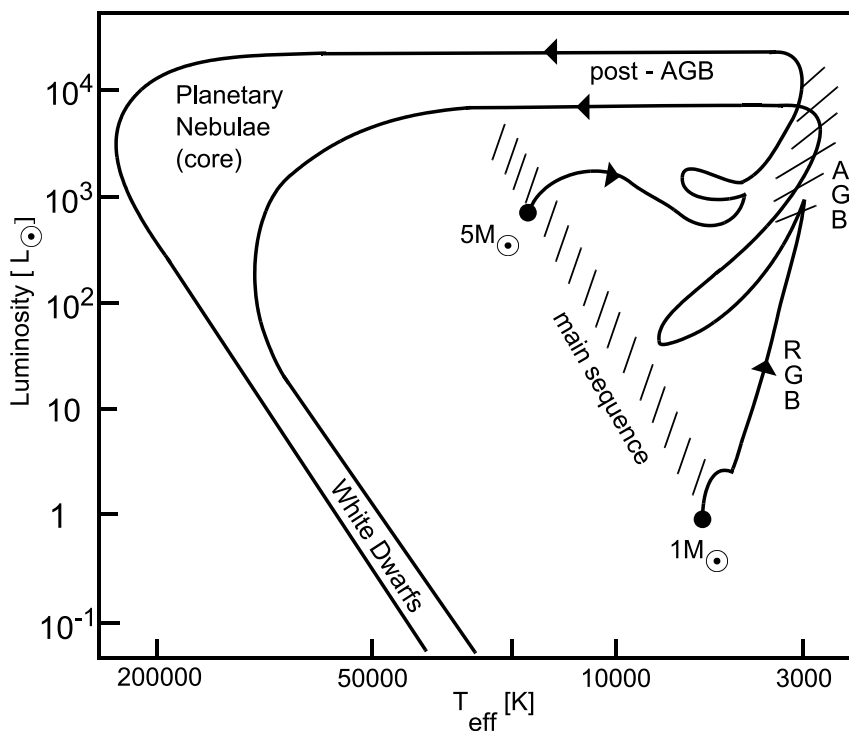 electron gas stops the compression. It cools down by radiating the heat generated in the compression, i.e., it is a white dwarf (WD).

In a medium-separated or close binary system ($a \lesssim 600\,R_\odot$) there is a fork in the evolution at the point of RGB or AGB. Once the primary evolves into a red giant (or a super red giant) and expands sufficiently to fill its Roche lobe, it begins mass transfer on a dynamical time-scale at a rate of about $0.1\,M_\odot$ per year. The accreting secondary, a low-mass main sequence star, cannot adjust its structure at that high rate. Thus the transferring material, instead of accreting on the secondary, passes through the outer Lagrangian point (L_2) and fills the outer Roche lobe (Chen *et al.* 1995; Warner 1995). The less massive and hence slower evolving secondary companion gets engulfed by the inflating envelope of the primary, whose radius can increase a hundred times compared to the earlier MS phase. Eventually the mass of this common envelope is expelled, when angular momentum is lost and rotation becomes differential, i.e., the outer layers, the inner layers and the nucleus itself do not possess the same period anymore. A planetary nebula (PN) is formed by this expelled material, leaving the nucleus of the PN as a close binary behind.

Some steps of this evolutionary scenario are not well understood. The most important un-solved questions are probably the outcome of a common envelope phase (see chapter 2.1) and the existence of an efficient mechanism to extract orbital angular momentum in close binaries containing a MS star, which is mainly inferred from observed mass transfer rates

in cataclysmic variables (CVs) (de Kool and Ritter 1993). Studying the properties of binaries that have gone through these phases can give an indication whether the scenario is correct. The binaries containing a sdO (or sdB) star are important for the study of common envelope evolution (CEE), because it can be safely assumed that the lifetime of the sdO star is much shorter than the orbital evolution timescale of the binary, thus their orbital angular momentum directly reflects the situation at the end of the CEE.

Another indicator for a recent CEE are PNe, which have a very short lifetime before they disperse, $\tau_{\rm PN}$ about 10^4 yrs. The presently observed orbital parameters in PNe nuclei, preferably containing a sdO, did not change since the CEE. The short timescale $\tau_{\rm PN}$ implies that only few of these long living systems are observed in their PN phase. Other types of post-CEE systems such as CVs, low mass X-ray binaries (LMXBs) or detached close WD+MS binaries, will have undergone significant orbital evolution since the CEE phase which can not be retraced (de Kool and Ritter 1993).

Whether the detached, evolved, yet close systems actually come from a 'common envelope' origin or not, they can be expected to be rather common (Pringle and Wade 1985), since there are already two observed in the Hyades cluster (the nearest stellar cluster) and a couple more at greater distance, but they are hard to recognize, because they are faint (CVs being several magnitudes brighter, because of accretion energy), and WD spectral lines are too broad for modest orbital radial velocity variations to show up in anything else than high resolution spectra.

1.1   Binary stars in history

The term 'binary stars' was first used by William Herschel, the amateur astronomer who founded modern cosmology (Wilson 1976), to designate double stars which are so close together in space that they move in orbits around their center of mass due to their gravitation. Or as he stated in his paper to the Royal Society : "[..] will go to prove that many of them are not merely double in appearance, but must be allowed to be real binary combinations of two stars, [..] held together by the bonds of mutual attraction." (Herschel 1802)

Many naked-eye double stars, such as α Capricorni and ϵ Lyrae, were probably noticed long ago. The one most easily seen, Mizar (ζ UMa, 2nd magnitude) in the Plough with its companion Alcor (80 UMa, 4th magnitude, is said to have been used by the ancient Arabs as a test of keen eyesight[3].

After the invention of the telescope by Hans Lipperhey and its improvement by Galileo Galilei 400 years ago, Mizar was itself the first telescopic double star to be noted, as consisting of two almost equal stars separated by 14 arc seconds, easily visible in a one-inch telescope.

But before Herschel's demonstration that some are 'binary', double stars were generally regarded as merely accidental cases of *apparent* closeness, 'optical' pairs for which the fainter companion is probably much more distant from us the the brighter one. Indeed, it was based on this incorrect assumption that William Herschel formed his plan to make frequent accurate measurements of close double stars having components of unequal brightness. He expected such measurements to show the relative annual trigonometric parallax of the brighter star, an annual apparent elliptical orbit reflecting the motion of the observer around the sun. If such

---

[3]The companion is 11 arc minutes northeast, i.e., separated by $\frac{1}{3}$ the apparent diameter of the sun.

Figure 1.3: Wilhelm Herschel (1738-1822) (taken from the homepage of the Armagh Observatory (www.arm.ac.uk))

measurement of the stellar parallax could be made, it would be an information on the scale of the universe, for which no measured observational evidence existed at his time.

Herschel was not successful in his objective of observing annual parallax (Herschel and Banks 1782), so his immediate accomplishment was only that of making the first catalogues (Herschel and Watson 1782; Herschel 1785) and fairly accurate measurements of several hundred double stars. His interest in double stars therefore was small after the publication of his second catalogue until about 1797, when he began to remeasure the relative positions of some pairs which he had first measured nearly 20 years ago. Comparisons showed that for several double stars, especially Castor of the Twins, there was clear evidence of relative motion, but not in an annual period as parallax should be. The changes where slow and in curved arcs, as in a big orbit.

This discovery was of great importance, since it indicated that Newtonian gravitation (Newton 1687) was a truly universal property of matter, not just in our solar system.

Binary stars such as those first recognized by Herschel can be seen as double by the eye, using sufficiently powerful optical aid. They are therefore called 'Visual Binary Stars'.

In 1842 Christian Andreas Doppler predicted that spectral lines from stars, displayed by the then recently developed spectrograph, would show a shift, i.e., a change in wavelength, $\Delta\lambda$, which is proportional to the velocity v towards or away from the observer given by the equation:

$$\frac{\Delta\lambda}{\lambda} = \frac{v}{c} \qquad (1.1)$$

where λ ist the wavelength of the spectral line in question and c is the speed of light.

Thus for any binary star, with an orbit not perpendicular to the observers line-of-sight, there would be a change in its spectrum due to change in radial velocity in the period of its orbit. By coincident it was the first discovered telescopic double star, Mizar, for which one component was first shown to be a 'Spectroscopic Binary Star' by Pickering in 1889. He observed that the spectral lines, usually double, became single in a uniform period of 20 days. Most orbital periods of these spectroscopic binaries are only a few hours or days, and only very few are more than a year, because short periods imply higher relative velocity and therefore easier discovery and investigation by observing Doppler spectral shifts.

From ancient times it has been known that there are a few peculiar stars which have changing brightness, and are therefore called variable stars. For most of these variables the brightness increases to a peak and then dimishes, either periodically or, for such as the 'new stars' or novae, just once or at irregular intervals of a year or more. However, for the star Algol[4] in Perseus the opposite kind of change occurs. i.e., it is usually constant, but at very regular intervals of 3 days it declines two magnitudes in brightness, but then at the same rate, returns to normal brightness, all within a few hours.

In 1750 Goodricke suggested eclipses by a companion star revolving around it as the explanation for the variation of Algol. There was no proof, however, until Vogel examined the spectrum of this star in 1889 and demonstrated that this 'Eclipsing Binary Star' hypothesis was correct, by showing that Algol is also a spectroscopic binary, having the same period as the occultation and whose relative radial velocity is equal to zero at the times of its eclipse.

1.1.1 Eclipsing, spectroscopic binaries

Most eclipsing binary light-curves show two eclipses in each period, the primary (or darker) eclipse being due to the cooler secondary star of the pair covering up an equal but brighter area of the hotter primary star. Likewise the secondary (or less dark) eclipse is induced by the primary covering up a part of the secondary's surface.

If the orbit is circular, the secondary eclipse will be exactly half way between successive primary eclipses, and any deviations from this will give the eccentricity and the phase of closest approach of the elliptical orbit. If the eclipses have a nearly flat bottom, i.e., some interval of almost constant minimum brightness, we may conclude that one minimum is due to total eclipse of the smaller star by the larger one, and the other minimum is due to transit of the smaller star over than the disc of the larger one. However, for a transit eclipse the minimum is usually not perfectly flat due to the fact that all stars naturally have limb darkening caused by the longer path of radiation through the star's atmosphere at the edge of its disc.

By using a spectrograph on a close binary star, its varying velocity of approach and recession can be determined throughout its orbital period, to give its velocity-curve. This is a sinusoidal curve that best represents all scattered points of various phases of the star's stellar orbit. From this the orbital elements are deducible, i.e., period, eccentricity, orbital longitude of periastron, date of the closest passage and semi-major axis of the orbit multiplied by the sine of the orbital inclination ($a \sin i$). For the semi-major axis there will always only be a lower boundary, since the inclination of the orbit to the plane of sky cannot be determined by this

---

[4]Arabic meaning: 'the demon', short form of *ra's al-ghūl* = 'the head of the demon' by its position in Perseus, representing the head of the gorgon 'Medusa', in later English sources sometimes referred as 'blinking demon'.

method and $\sin i \leq 1$. Using Kepler's laws as derived by Newton, the minimum masses of the components may also be computed.

If the pair is a visual/eclipsing and spectroscopic binary, the inclination can be determined, so that definitive values for the dimensions, masses and luminosities can be established. This is the only method to determine stellar parameters, upon which theories must be depend. Therefore eclipsing binaries are excellent cases for study.

1.2   Outline

Chapter 1 contained a motivation why analyzing close binary systems, containing an sdO inside of a PN, is important to test theories about an angular momentum loss mechanism, the influence on the evolution of its companion and the CEE in general. The history of binary stars was briefly covered in section 1.1 and explained what is special about them compared to single stars.

In the upcoming chapter 2 an overview on how the common envelope evolution (CEE) mechanism might work is given. The chapter includes a simple example to make the idea of the CEE more comprehensible.

The tools for the analysis of irradiated stars in close binaries will be presented in chapter 3, which contains a brief introduction to the general purpose of the stellar atmosphere code PHOENIX and explains explicitly the modifications which were required, to the general radiative transfer equation (RTE) and the temperature correction (TC) to include an external radiation field and obtaining a converging solution.

In chapter 4 an upgrade from the standard 1D towards a quasi 1.5D patchwork geometry is presented. For the isotropic case an analytic solution is given, while the non-isotropic case requires a numerical solution. An example of different incoming irradiation angles is given, which is connected to the analyzes in the next chapter.

An example on how PHOENIX can be applied to analyze the physical parameters of UU Sagittae (UU Sge) is given in chapter 5.

Finally in chapter 6 conclusions and an outlook of possible future work is discussed.

Given in the appendix of this thesis is auxiliary material for more insight and probably future work, in detail:

- a list of input parameters for the PHOENIX irradiation mode

- a list of parameters and references for known young pre-CVs

- a comparison of the photospheric abundances by Asplund *et al.* (2005) to older values and how this effects the analysis

- an IDL code of the method described in chapter 4, which allows to calculate the weight of patches for an 1.5D approach.

Chapter 2

Close binary stars

In a binary system, stars can evolve differently than they would in isolation because the gravitational influence of one of the components can limit the radius of the other. Mass beyond this radius can be transferred to the binary companion and/or lost from the system. This transfer or loss of mass and angular momentum is central to understanding all classes of close binary systems. The critical radius is referred as the Roche radius for components in synchronous rotation and circular motion about their common center of mass. For fast spinning components in eccentric orbits this critical radius is difficult to determine, because more parameters are of importance, but the effective synchronization by tidal force (Zahn 1977, 1989) justifies the above simplification. For a binary system of orbital separation R, the Roche radius R_{L} of a mass m_{p} (primary) with a companion of mass m_{s} (secondary) is given to a good approximation by the equation:

$$R_{\mathrm{L}} = R\frac{0.49q^{2/3}}{0.6q^{2/3} + \log\left(1 + q^{1/3}\right)} \tag{2.1}$$

where q is the mass ratio $m_{\mathrm{p}}/m_{\mathrm{s}}$ of the system (Eggleton 1983). Using the inverse ratio $m_{\mathrm{s}}/m_{\mathrm{p}}$ in equation 2.1 yields the R_{L} of the secondary companion.

The orbital separation is related to the orbital angular momentum, J, of the system by:

$$R = \frac{J^2(m_{\mathrm{p}} + m_{\mathrm{s}})}{Gm_{\mathrm{p}}^2 m_{\mathrm{s}}^2} \tag{2.2}$$

where G is the gravitational constant. Mass loss of the star in the response of the imposition of such a radius constraint, coupled with the orbital evolution determines the outcome of the system.

Depending on the separation and the Roche lobes of both components one distinguishes between:

- detached: well separated, no mass transfer possible

- semidetached: one components fills its Roche lobe and transfers mass to the other

- overcontact: both components have radii larger than their Roche lobe and material can flow both ways
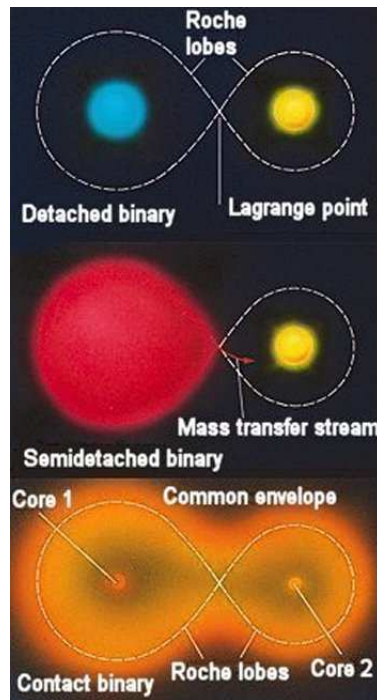
as can be seen in illustration 2.1.

Figure 2.1:   Close   binary   configurations   (illustration   by   David   Darling
(www.daviddarling.info))

For fundamental reviews of the binary star evolution, see Paczyński (1971); Thomas (1977);
Vanbeveren *et al.* (1998). A general description of orbital variations in the presence of mass
and angular momentum loss can be found in Soberman *et al.* (1997).
In the following section 2.1 one mechanism, that can transform far separated binaries into
close binaries, will be described in more detail.

2.1   Common envelope evolution

Even though it is mainly the outcome, i.e., the close binaries (CBs) or more precisely the
pre-cataclysmic variables (pre-CVs), that we are interested in, it is useful to have at least a
brief look on the mechanism proposed to produce them, the common envelope evolution
(CEE). The possibility of forming a common envelope binary was first discussed in the
1970's by Sparks and Stecher (1974); Refsdal *et al.* (1974); Chau *et al.* (1974); Webbink
(1975a,b); Alexander *et al.* (1976); Paczynski (1976) suggesting that cataclysmic binaries
may be products of some common envelope binaries with very long initial periods.
In the 1990's the topic was revived by Iben and Livio (1993); Warner (1995); Livio (1996)
believing that this mechanism is able to expel the envelope of a Asymptotic Giant Branch
(AGB) star (Rasio and Livio 1996; Sandquist *et al.* 1998) and due to this momentum loss
produce CBs.
However, there are ongoing discussions upon this topic until now and also alternative mech-
anisms (see e.g. Nelemans and Tout (2005); Taam and Ricker (2006); Webbink (2008); Beer
et al. (2007) and references therein) are under investigation.

2.1.1   Basic approach

Let us do a very basic analysis and consider a binary system moving in a circular orbit in a low density medium. Let us further assume for simplicity that the circumbinary medium is at rest and the components of the binary of mass M have the orbital velocity v:

$$v = \left(\frac{GM}{R}\right)^{\frac{1}{2}} \tag{2.3}$$

where G is the gravitational constant and R is the separation between the components. The geometrical cross-section of the binary Roche surface is proportional to R^2 and the drag force D experienced by the binary may be estimated as:

$$D \sim R^2 v^2 \rho \sim GMR\rho \tag{2.4}$$

where ρ is the density of the circumbinary matter.

Friction due to the drag generates heat proportional to Dv. Using the same geometry as before we can estimate the drag luminosity L_D:

$$L_{\mathrm{D}} \sim Dv \sim D\frac{R}{P_{\mathrm{orb}}} \sim \frac{GMR^2}{P_{\mathrm{orb}}}\rho \tag{2.5}$$

where P_{orb} is the orbital period of the binary.

The heat is generated at the cost of gravitational binding energy of the binary. Therefore we get a relation:

$$L_{\mathrm{D}} \sim \frac{\mathrm{d}}{\mathrm{d}t}\frac{GM^2}{R} \sim \frac{GM^2}{\tau_{\mathrm{D}}R'} \tag{2.6}$$

where τ_{D} is the time scale on which the drag force lets the components of the binary spiral in on each other. Using the relation 2.5 and 2.6 we obtain:

$$\frac{\tau_{\mathrm{D}}}{P_{\mathrm{orb}}} \sim \frac{M}{R^3\rho} \sim \frac{<\rho>}{\rho} \tag{2.7}$$

Where $<\rho>$ is the mean density of matter within the binary system. If the mass of the two cores is much larger than the mass of the circumbinary matter within the cube of volume R^3, then $<\rho>$ is much larger than ρ and τ_{D} is longer than the orbital period.

Figure 2.2 shows the Lagrangian points and illustrates unique stationary positions for a third object of negligible mass in this two-body-problem. When the surface of the primary expands so much that it moves beyond L_1 then the secondary can accrete mass. Once the Roche lobe of the secondary is filled, too, and the surface of the primary moves beyond the outer Lagrangian point L_2, additional mass can not be captured by the secondary anymore but flows around it and due to changing rotational velocity, is unbound from the primary and secondary, forming a common envelope. It is suggested that while the two dense stellar nuclei spiral towards each other, the envelope expands and is eventually lost completely, resulting in a planetary nebula. Most of the angular momentum is lost with the envelope, therefore the final orbital period may be orders of magnitude smaller than the initial one, explaining how far separated binaries can become close binaries in such a short time scale.
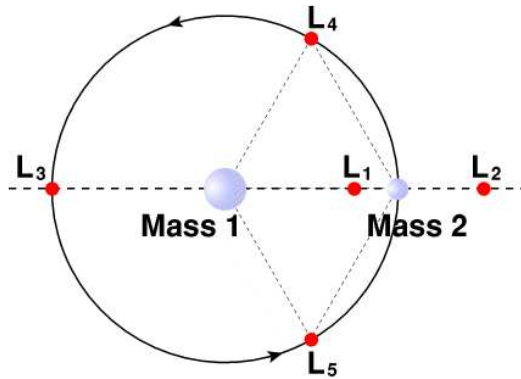
Figure 2.2: Illustration of Lagrangian points in a two-body-problem.

2.1.2   Example

Let us assume that we have a primary with initial mass of $2\,M_\odot$ that reaches a double shell source burning phase. According to stellar evolution tracks this means a luminosity of $16\,000\,L_\odot$ and a radius of $600\,R_\odot$, it is a red supergiant. It shall fill its Roche lobe and its companion, a main sequence star, shall be inside its surface, so that the initial orbital period is about 10 years.

If the core has about $0.8\,M_\odot$, then the extended low density envelope contains about $1.2\,M_\odot$ of hydrogen rich matter. With the radius of the red giant as large as $600\,R_\odot$ the density throughout the envelope is fairly uniform, $\rho \approx 10^{-8}$ g cm^{-3}. This is the circumbinary density which appears in equation 2.7. By the time the two nuclei spiral in to a separation of $R = 60\,R_\odot$ the mean density within the binary system is $< \rho > \approx 10^{-5}$ g cm^{-3} and therefore $\tau_D \approx 10^3\,P_{\mathrm{orb}}$. That means that the spiral is very tight and the binary orbit almost circular. As the mean density within the binary system varies as R^{-3} while the density of the matter in the envelope of the red supergiant is almost constant the spiraling may be expected to be rapid initially and to slow down as the two nuclei approach each other.

As the two nuclei come closer and closer, their orbital angular momentum decreases as the square root of the separation, R. The same is true for the angular momentum per unit mass in the binary. The angular momentum accumulates in the extended envelope. At some point the angular moment per unit mass will be so much larger in the envelope than in the binary that it will be increasingly difficult to transfer the angular momentum out. This shows in equation 2.4 as a decrease in the relative velocity of the binary with respect to the surrounding matter. The circumbinary envelope will rotate differentially and this will decrease the drag force, too. If the drag force luminosity becomes comparable to the luminosity of the red giant then the envelope will expand in order to increase the radiating surface at the photosphere to compensate for the extra luminosity. As a result the density of matter in the envelope will decrease and this in turn will decrease the drag force and the heat dissipation, i.e. the drag luminosity, until a new equilibrium is reached.

Eventually at some point of evolution the extended envelope will be lost. What is left are two small stars accreting whatever hydrogen rich material is left in within their Roche lobes. So at this time the degenerate core of the remaining envelope has the typical structure of a nucleus of a planetary nebula. The hot star will ionize the expanding envelope, which will

be visible due to its induced emission.

2.2   pre-CV to CV

The above mechanism is believed to produce detached close binary systems. This is the class that we are interested in. But how is the final step from pre-CV to CV accomplished or in other words, what happens after the common envelope evolution (CEE)?

If the binary system is close enough for tidal forces to distort one or both components, then the gravitational potential is no longer a simple r^{-1} but contains additional terms. The extra terms produce a small error in the equation of Kepler's law $P = 2\pi \sqrt{\frac{a^3}{G(m_\mathrm{p}+m_\mathrm{s})}}$ (at most a few percent) and give rise to apsidal motion by ensuring that the orbit is no longer a close ellipse. However, the effect of the tidal interaction is eventual to circularize the orbit and make both stars corotate with the orbital period. This is because stars in eccentric orbits and non-corotating stars in circular orbits are subject to tidal forces of varying amplitude. Thus the stars in a binary system which has an eccentric orbit and/or in which non-corotating occurs are forced to pulsate[5]. Such pulsations are damped out by viscous effects, and the dissipation of energy caused ensures that the system eventually ends up in a minimum energy state. It is a generally a reasonable assumption that a close binary system has a circular orbit and a synchronously rotating components (Pringle and Wade 1985).

The theory for stars with convective envelope (CE), where the dissipation is caused by turbulent friction in the CE and the stars with convective core (CC), whereas it is due to radiative damping in the non-adiabatic layers located near surface is discussed by Zahn (1977, 1989). It is worth noting, however, that within the framework of Zahn's theory, the synchronization timescales are several orders of magnitude smaller than the circularization timescales (Toledano *et al.* 2007). This will be important in our models to justify a uniform irradiation at a constant distance and on the same side of the secondary, which itself is convective at least in in deeper layers than the irradiation can penetrate.

Also worth noting is that Zahn (1977, 1989) found the characteristic timescale for synchronization as a function of a, the major semi-axis of the orbit, to be $\tau_{sync} \sim a^6$ for stars with convective envelopes and $\tau_{sync} \sim a^{8.5}$ for stars with with radiative envelopes. This might explain why some primaries show rotational broadening even if in very close orbits around their companion. They are smaller, more compact and, for very young cases, still contracting and have therefore not yet reacted to synchronization with their radiative envelope as most secondary main-sequence stars have.

---

[5]I.e., they get deformed by tidal forces at the substellar point at periastron and relax at apastron for an eccentric orbit, respectively the deformation at the substellar point needs to move for the non-corotating case.

Chapter 3

Model setup in PHOENIX

In most binary systems the orbital separation is so large that the only significant interaction between them is gravitational. However, there are systems where the separation is comparable to the dimensions of the components. In such a situation the radiation field of each component will influence the other. In the literature this effect is known as 'irradiation' or sometimes 'reflection' effect and has been recognized for decades. It plays an important role in close binary star systems, e.g. pre-cataclysmic variables (pre-CVs). It is also of importance in our own solar system and nowadays considered in extrasolar planets that orbit their parent star very closely. The first theoretical study of irradiation was performed by Eddington (1926) who points out that all incident radiation on a star must be absorbed and re-emitted as thermal radiation (or scattered light) if a static solution and energy conservation is assumed. Therefore, the 'heat-' or 'bolometric-albedo' is equal to one for purely radiative atmospheres. Eddington (1926) also pointed out that the interior of the star should not be altered by the irradiation. Most later works that dealt with irradiation focused on the construction of synthetic light curves for close binaries, where the irradiation was merely treated as a correction to the bolometric flux. Vaz and Nordlund (1985) give a good review about the efforts to understand and model irradiation in stars prior to 1985.

In the last two decades there have been many improvements in the modelling of binary stars and the construction of synthetic light curves. Orosz and Hauschildt (2000) use model atmospheres to better describe the monochromatic flux (or at least narrow bands) of binary systems. The treatment of the irradiation has also progressed steadily in model atmospheres over the years and several important achievements have been made. Nordlund and Vaz (1990) constructed the first convective non-grey irradiated atmosphere. They demonstrated that for convective atmospheres the same entropy at depth must be maintained if irradiated and non-irradiated case shall describe the day-side and simultaneous the night-side of the same star. A consequence of this entropy matching is that the heat-albedo will be less than one and will depend on the efficiency of convection, i.e., the convection will transfer some heat to the night-side so there is no full reradiation on the day-side. Nordlund and Vaz (1990) also showed that the presence of absorption lines in the incident spectrum and orientation of these lines in respect to those in the spectrum of the irradiated star can play an important role in determining the atmospheric structure. Shortly after Brett and Smith (1993) calculated the first irradiated model atmospheres for cool M dwarfs (3000 - 3500 K) located very close to a 10 000 K blackbody, which is used as source of irradiation. These models confirmed the basic results of Nordlund and Vaz (1990) and also demonstrated that horizontal energy flux from the day-side to the night-side is likely to be important in irradiated atmospheres.

Many of the earlier model atmosphere calculations were limited to plane parallel geometry and, in some instances, did not satisfy energy conservation. Also opacity[6] sources, i.e., laboratory measurements and theoretical calculations of line positions and strengths, were inaccurate and incomplete. This is why opacity distribution functions or straight mean opacities were often used. These crude opacities were scaled to give the correct wavelength integrated opacity but were insufficient for high resolution synthesis. As a result, both impinging radiation and the spectrum of the irradiated star lacked many important atomic and molecular features. Over the past decade, several large atomic and molecular line lists for many of the important species have been measured in the laboratory and calculated by theorists. Now calculations of detailed line-blanketed models for broad ranges of temperature are possible. For this work we:

- use the newest extensive set of opacities currently available for the modeling of both extrinsic and intrinsic radiation fields

- use a customized temperature correction procedure that fulfills energy conservation in the calculated models even with extreme irradiation

- explicitly include the incident flux in the solution of the radiation transfer equation in a self-consistent, i.e., energy conserving, manner

- use spherical geometry for a more realistic approach to the problem of irradiation on the heated object

- produce high resolution spectra for direct comparison with observations of known pre-CVs

3.1   Model atmospheres in general

The general model atmosphere problem involves a self-consistent solution of many coupled physical and chemical problems with the ultimate goal to describe all properties of an atmosphere at any time. Even today with high speed computer clusters, like the new HLRN-II, this task is still beyond our capabilities. It requires simplifying approximations to make the problem more traceable while still trying to be close to the real situation. Analytic solutions of model atmospheres only exist for extremely simplified approximations and are, while sometimes good for very basic test cases, usually far from describing a real atmosphere. Numerical calculations are the only means to produce realistic models that can be compared to observations.

Even though there are finally two- and three-dimensional model atmosphere codes in development, since the computational power increased greatly over the last years and will probably keep growing, the current state-of-the-art codes treat the atmosphere as a one-dimensional collection of homogeneous semi-infinite plane parallel slabs or spherically symmetric concentric shells. The plane parallel approximation is considered to be appropriate if the mean free path of a photon is much smaller than the thickness of the atmosphere, which itself must be much smaller than the overall radius. For objects like white dwarfs or M dwarfs these criteria are often fulfilled. However, we will use the spherically symmetric

---

[6]$\chi = \kappa + \sigma$, the sum of absorption and scattering coefficients

approximation for the irradiated object, to take the special geometry of this problem directly into account.

The structure of a model atmosphere is often based on two assumptions. First the atmosphere needs to be in hydrostatic equilibrium and must have a pressure gradient to support itself. This leads to:

$$\nabla P(r) = -\rho(r)g \tag{3.1}$$

where P is the total pressure, ρ the density, r the radius, i.e., the distance to the center of the star and g the gravitational acceleration given by:

$$g(r) = GM(r)/r^2 \tag{3.2}$$

where $M(r)$ is the mass of the star inside the radius r and G the gravitational constant. Secondly, the atmosphere is assumed to be in thermal equilibrium and conserves energy. This means that the gradient of the luminosity L must be zero:

$$\nabla L = 0 \tag{3.3}$$

The luminosity constancy of the atmosphere in spherical geometry is also used to define an *effective* temperature (T_{eff}) of the atmosphere by:

$$4\pi r^2 \sigma T_{\text{eff}}^4 = L \tag{3.4}$$

with σ as the Stefan-Boltzmann constant.

T_{eff} and g (or $\log g$) are often used as model parameters. A great reduction to the complexity of the model atmosphere problem is achieved if one can assume that the material in each layer is in local thermal equilibrium (LTE). If the material is in LTE, the chemical equilibrium, ionization fraction and level populations for each species are completely determined by the local gas temperature and electron gas pressure at a specific layer. However, decoupling the local state of the material from the depth dependent radiation field can be a very poor approximation in several different environments, including white dwarfs. In conditions where the level population and ionization of atoms and molecules are mostly determined by collisional processes, the LTE assumption is valid. Even if this assumption is not fulfilled, a LTE approximation is still a useful tool for testing a stellar atmosphere and for comparison to a non local thermal equilibrium (NLTE).

3.1.1   The radiative transfer

PHOENIX has two modes for the radiative transport. These are the time independent one dimensional plane parallel radiative transfer equation (PPRTE) and the also time independent one dimensional but spherical symmetric radiative transfer equation (SSRTE):

$$\text{PPRTE:} \qquad \mu\frac{\mathrm{d}I_\nu}{\mathrm{d}r} = \chi_\nu(S_\nu - I_\nu)$$

$$\text{SSRTE:} \qquad \mu\frac{\partial I_\nu}{\partial r} + \frac{1-\mu^2}{r}\frac{\partial}{\partial\mu}I_\nu = \chi_\nu(S_\nu - I_\nu) \tag{3.5}$$

With the variables above being:

- I_ν the specific intensity with frequency ν and direction μ

- $\mu = \cos\theta$, where θ is the angle between I_ν and the vector normal to the surface

- χ_ν is the extinction coefficient and with $\mathrm{d}\tau_\nu = -\chi_\nu\,\mathrm{d}r$ correlated to the optical depth τ_ν and the physical depth r with origin at the center of the object, i.e., $r = 0$ at the center and $r = R$ at the surface. Note that therefore τ decreases as r increases.

- $S_\nu = \frac{\eta_\nu}{\chi_\nu}$ is the source function, the ratio of emissivity η_ν and extinction χ_ν

For thermal emission and isotropic coherent scattering we can write:

$$S = \frac{\sigma}{\kappa + \sigma}J + \frac{\kappa}{\kappa + \sigma}B = (1 - \epsilon)J + \epsilon B \qquad (3.6)$$

where is:

- $B_\nu = \frac{2h\nu^3}{c^2}\frac{1}{e^{\frac{h\nu}{kT}} - 1}$: the Planck function

- $J_\nu = \frac{1}{2}\int_{-1}^{1} I_\nu\,\mathrm{d}\mu$: the mean intensity

- κ the absorption and

- σ the scattering coefficient.

The solution to either the PPRTE or the SSRTE is carried out along many characteristics at discrete values of τ (in radial direction) and many frequency points. Because the source function depends on the specific intensity, the radiative transport equation (RTE) is normally solved iteratively by applying successive corrections to the intensity (or mean intensity) until a desired accuracy is achieved. The ability to converge on the correct solution depends strongly on the iteration scheme used. The classical Λ-iteration will not work (Mihalas 1970, 1978). By far the most efficient method is the so called accelerated Λ-iteration (ALI) (Cannon 1973; Olson and Kunasz 1987; Rybicki and Hummer 1991; Hauschildt 1992).

Since the RTE depends on the opacity (χ_ν), the opacity is determined by the equation of state (EOS) and the EOS depends indirectly on the RTE due to temperature changes, it is necessary to solve RTE and EOS in an iterative process simultaneously while holding to the constraints in equation 3.1 and 3.3. Therefore the entire model atmosphere problem must also be solved iteratively. Once the mass, radius, T_{eff} and chemical composition are specified, the atmosphere problem is well defined and this specific situation may be modeled. At the start of the first iteration an initial guess for the temperature structure, i.e., the temperature in each radial layer, is given or, if none is available, obtained from the grey approximation, which assumes that opacity is independent of frequency. With this temperature structure the EOS and RTE are solved and the energy conservation constraint is tested. If the prescribed accuracy for the total energy conservation is not reached, a correction to the temperature at each layer is made so that the source function produces the correct flux. This process is repeated until the temperature correction is smaller that the prescribed accuracy and hence the total energy is conserved in the model. The important steps of the modeling in PHOENIX can be also be seen in the flow chart of figure 3.1.

3.2   The model atmosphere code PHOENIX

There are quite a few model atmosphere codes available nowadays of which ATLAS (Kurucz 1996), TLUSTY (Hubeny 1988), MARCS[7] (Gustafsson *et al.* 2008) and PHOENIX

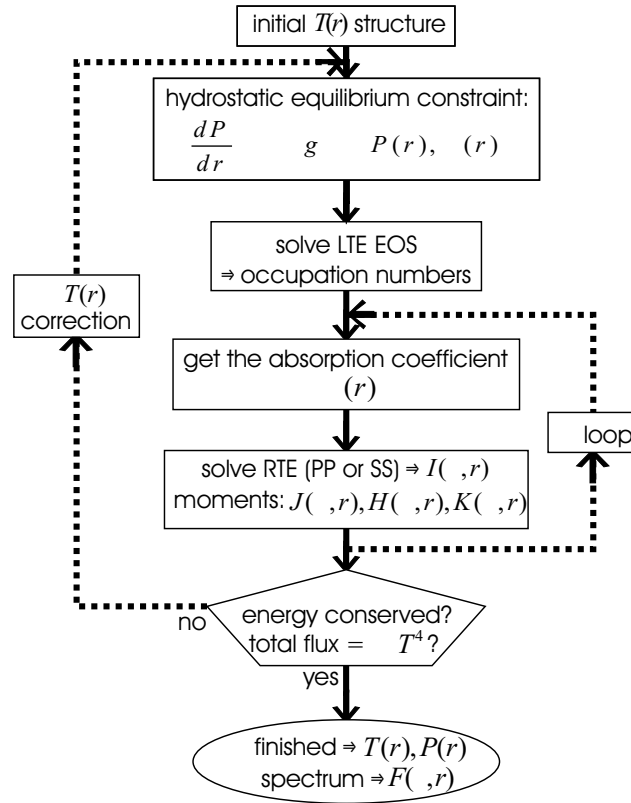[7]A merger of UMA (Gustafsson *et al.* 1975) and SSG (Bell 1970, 1973)

Figure 3.1: The basic method of solving the LTE model atmosphere problem is displayed in this flow chart (adapted from Schweitzer (1999)).

(Hauschild and Baron 1999a) are a few of the more popular ones. Each code follows the same physical recipe for constructing a model atmosphere but they greatly vary in assumptions, techniques, ingredients and also generality. PHOENIX is the only code that is general enough to construct atmospheric models for objects across the entire Hertzsprung-Russel (H-R) diagram in either LTE or NLTE. This flexibility makes PHOENIX the obvious choice for modeling irradiated atmospheres, since we need to model one hot as well as one rather cool object for this task.

PHOENIX is capable of solving plane parallel radiation transport equation (PPRTE) or spherically symmetric radiation transport equation (SSRTE) with the accelerated Λ-iteration (ALI) method on a standard optical depth grid (τ_{std} defined at 5000 Å for hot and 1.2 μm for cooler objects) with typically 64 to 128 layers. The PPRTE is solved along 16 angles while the the SSRTE is solved along $\sim$ 100 to 200 characteristics[8] which enables an angle dependent view for the later irradiation treatment. There are roughly 150 000 frequency points from 10 Å to 1000 μm used for the model calculation. For the final production of a synthetic spectrum for comparison to observation the resolution of the wavelength region of interest is increased to approximately 0.2 Å, but nearly any value is possible.

---

[8]Depends directly on the number of layers -1, plus twice the selected extra number of core characteristics, for which a typical value is 15 or 50.

PHOENIX includes 83 of the most important atomic elements from hydrogen (H) to uranium (U), i.e., atomic numbers 1 through 92, as well as many of their important ions. The atomic data for the energy levels and bound-bound transition are taken from Kurucz (see Kurucz (1993a)[9], Kurucz (1994), Kurucz and Bell (1995a), Kurucz and Bell (1995b) and Kurucz and Bell (2006)). The photo-ionization cross sections are from Mathisen (1984) and Verner and Yakovlev (1995).

PHOENIX contains a huge collection of line data for molecular opacities, since these are crucial in cool stars to reproduce realistic spectra. For M stars and later these are TiO, VO and H_2O in the optical and near infrared region (Merrill *et al.* 1962). For stars with lower than solar abundance also hydrides like CaH, MgH and FeH are important in the spectrum (Schweitzer 1999). While quality (accuracy) and quantity (frequency and energy range) for many molecules have greatly improved in the last decade there is still work to do for some molecules like FeH for which theoretical predictions are still incomplete.

These are line lists so far included and available for atmosphere model calculations:

- collision induced absorption opacities for H, H_2, He, N_2, Ar, CH_4 and CO_2 (Borysow *et al.* 1997; Borysow and Frommhold 1986a,b,c, 1987a,b; Borysow and Tang 1993; Samuelson *et al.* 1997; Gruszka and Borysow 1997, and references therein),

- 'ab initio' calculations for H_2O (Miller *et al.* 1994; Schryber *et al.* 1995; Barber *et al.* 2006) and TiO (Partridge and Schwenke 1997; Jorgensen 1994; Schwenke 1998),

- CO (Goorvitch and Chackerian 1994a,b; Goorvitch 1994),

- MgH, OH and other diatomics (Kurucz 1993b),

- VO and CrH (R.D. Freedman 1999, private communication),

- FeH (Phillips and Davis 1993),

- CaH in line approximation (described in Tsuji 1995; Tsuji *et al.* 1996a,b, and references therein) and as line list (Weck *et al.* 2003),

- for TiO, VO and CaH (B. Plez (2004), private communication, following the scheme of older work described in Plez 1998; Langhoff 1997),

- all molecules from the GEISA (Husson *et al.* 1992), HITRAN92 (Rothman *et al.* 1992) and HITRAN2004[10] database (Rothman *et al.* 2005),

- hydrides FeH, TiH and CrH (P. Bernath (2007), private communication, see also Bernath 2006, 2007).

At very low effective temperatures, below 2500 K, PHOENIX (Allard *et al.* 2001) includes dust grains assuming an interstellar size distribution with diameters ranging from 0.00625 to 0.24 μm. The numbers densities for each grain species are calculated using the method of Grossmann (1972) and the Gibbs free energies of formation from the JANAF database (Chase *et al.* 1985). There is a new stand-alone module, called Drift (Helling *et al.*

---

[9]Contains more than $4.3 \cdot 10^7$ atomic transitions.

[10]Already containing 38 different simple and complex molecule types.

2008a,b,c), which calculates nucleation in a self-consistent manner and uses an interface[11] from and to `PHOENIX` for data transfer.

The total number of atomic and molecular lines currently available in `PHOENIX` exceeds 1.2 billion of which water with more than 500 million lines contributes the most by far. The opacity in the infrared of M dwarfs is a typically around 60% produced by H_2O, which demonstrates the importance of this molecule in particular.

All lines in LTE are treated with the direct opacity sampling (dOS) method, since `PHOENIX` does *not* use precalculated opacity sampling tables, but instead dynamically selects all relevant LTE background lines from the above described atomic and molecular master line lists at the beginning of each iteration at several depth points (or at least for the very first iteration if the selection is voluntary disabled). The total contribution of every selected line within a search window is used to compute the total line opacity at *arbitrary* wavelength points. Therefore this method allows detailed and depth-dependent line profiles during each iteration. The selection criterion for lines from the master line list is a threshold value $\Gamma \equiv \chi_l / \kappa_c$, which is typically set to 10^{-4}, where χ_l is the extinction coefficient at the line center and κ_c the total continuous absorption coefficient. Both are calculated at typically three representative standard optical depths, namely $\tau_{\mathrm{std}} = 10^{-4}$, 10^{-2} and 10. The profiles of these lines are assumed to be depth-dependent Voigt or, for very weak lines, Doppler profiles.

3.2.1 Line profiles

Even though the line transition energy (in contrast to continuum processes) should be, in classical view, very accurate, the quantum mechanical uncertainty leads to a small variation in the energy transition. This broadening of the natural line width depending upon frequency is described by the natural line or Lorentzian profile:

$$L(\nu - \nu_0) = \frac{\gamma}{4\pi^2(\nu - \nu_0)^2 + \gamma^2/4} \tag{3.7}$$

where γ is a specific dampening constant and ν_0 the central frequency. Analogous to the natural broadening there is pressure broadening, which originate from (elastic and inelastic) collisions of atoms during line transitions and therefore is directly scaled with the pressure. It is approximated by a Lorentzian profile and usually the dominant effect of these two broadening mechanisms. The combined line profile due to natural broadening and pressure broadening is referred to as damping profile (see figure 3.2).

Not only the natural broadening and pressure broadening have an influence on the line profile, but also the thermal motion of the atom, which results in a Doppler shift and therefore an additional broadening. This is taken into account by a Doppler or Gauß profile if the problem is approximated by a Maxwell distribution:

$$D(\nu - \nu_0) = \frac{1}{\sqrt{\pi}} \frac{1}{\nu_{\mathrm{D}} - \nu_0} \exp\left[-\left(\frac{\nu - \nu_0}{\nu_{\mathrm{D}} - \nu_0}\right)^2\right] \tag{3.8}$$

where the Doppler parameter is given by $\frac{\nu_{\mathrm{D}} - \nu_0}{\nu_0} = \frac{v}{c}$. The convolution of Lorentzian and Doppler profile gives the Voigt profile which includes both effects and is illustrated in figure 3.2):

$$H(\nu - \nu_0) = L(\nu - \nu_0) * D(\nu - \nu_0) \tag{3.9}$$

---

[11]The incorporation was started by Matthias Dehn and is continued by Sören Witte in a parallel `PHOENIX` project.

Using the temperature it is decided during runtime of `PHOENIX` whether the more time consuming Voigt or the computationally cheaper Doppler profile is used for each line independently. If lines are very weak, so that their wings have no great influence on the outcome, this selection criterion can save a lot computation time.
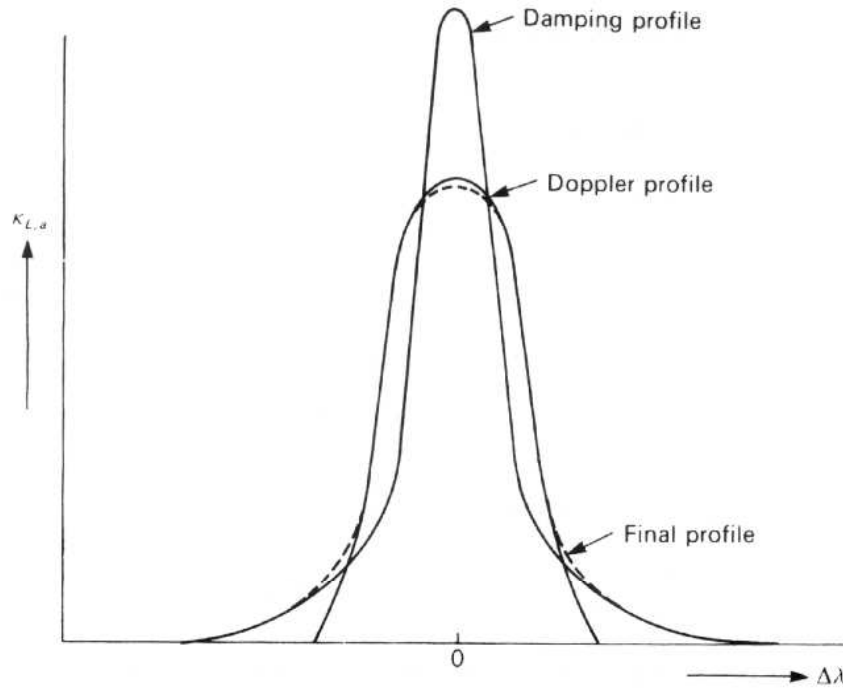

Figure 3.2: Shown is the convolution of a Lorentzian profile (Damping profile) and Doppler profile to a Voigt profile (Final profile) (taken from Böhm-Vitense 1989).

Test calculations, however, have shown that the details of the line profiles and threshold Γ do not significantly affect either the model structure or the synthetic spectra for sufficiently small values of Γ (Schweitzer 1995; Schweitzer *et al.* 1996).

3.3   Modifications for irradiation

One crucial point of this work is the structure of irradiated atmospheres and the spectral energy distribution. It all starts with producing synthetic light curves which, however, will not be discussed here. Instead the following chapter directly presents the basic geometry of irradiated secondaries in close binaries and focuses on the construction of model atmospheres. Since the method is applicable not only to close binaries but also to extrasolar planets the irradiated object will simply be referred to as the *secondary* while the source of irradiation is the *primary*. In the following the variations to the general model construction of `PHOENIX` in order to include irradiation will be described in more detail.

3.3.1 Boundary conditions

The solution of the RTE is a two-point boundary value problem in spatial coordinates. For stellar and substellar atmosphere calculations it is assumed that at large optical depth, i.e., where photon migration is dominated by scattering, the diffusion approximation is valid and defines the lower boundary condition. Also it is usually sufficient to set the upper boundary condition to zero incoming intensities, since most objects are well separated from any external radiation source, i.e., the ratio of external and intrinsic flux on the star's surface is $<< 1$. Therefore all incoming intensities at the surface are zero or more precisely $I_\nu(\tau = 0, \mu)$ for $\mu < 0$.

Of course this *isolated* upper boundary condition is no longer valid in a close binary system and therefore must be replaced by a new boundary condition that accounts for the incoming radiation originating from the nearby companion. Hence, for irradiated plane parallel atmospheres, we take a new upper boundary condition, i.e., at $\tau = 0$:

$$\int_0^{2\pi} d\phi \int_{-1}^0 I_\nu(\phi, \mu)\mu \, d\mu = F_\nu^{\mathrm{inc}}(\tau = 0) \tag{3.10}$$

where F^{inc} is the monochromatic flux from the primary incident upon the secondary surface. For the plane parallel case extrinsic radiation incident at angles μ_{inc} and ϕ_{inc}, so that:

$$I_\nu(\phi, \mu) = I_\nu^{\mathrm{inc}} \, \delta(\phi - \phi_{\mathrm{inc}}) \, \delta(\mu - \mu_{\mathrm{inc}}) \tag{3.11}$$

From equation 3.10 we get directly:

$$I_\nu^{\mathrm{inc}} = F_\nu^{\mathrm{inc}} \tag{3.12}$$

And if the incoming radiation is assumed to be isotropic then we get:

$$I_\nu^{\mathrm{inc}}(\phi, \mu) = I_\nu^{\mathrm{inc}} = \frac{1}{\pi} F_\nu^{\mathrm{inc}} \tag{3.13}$$

Most stellar and substellar objects are well approximated by spheres. Hence the irradiation from the primary can be treated as if it originated from a point source located at the center of the primary (Wilson 1990).

For spherical symmetric irradiation equation 3.10 is, strictly speaking, no longer valid, because due to the geometry of the problem the flux does not equal the intensity anymore as in equation 3.12, i.e., the radius no longer cancels out. One can, however, directly use the intensity of the primary reaching the secondary surface and integrate it for a total incoming flux.

Figure 3.3 illustrates the irradiation on the point on the secondary surface closest to the primary. This spot is often called the substellar point or sometimes hot spot and labeled as S_1. The flux, which is measured in erg sec^{-1}cm^{-2}Hz^{-1}, received by the secondary at $S1$ is:

$$F^{\mathrm{inc}}(\tau = 0) = \left(\frac{r_{\mathrm{p}}}{d}\right)^2 F_{\mathrm{p}} \tag{3.14}$$

where r_{p} is the radius of the primary, F_{p} the flux from the primary surface and d the distance from the primary center (P_0) to S_1. In this case $d = R - r_{\mathrm{s}}$, i.e., the center to center distance minus the radius of the secondary.
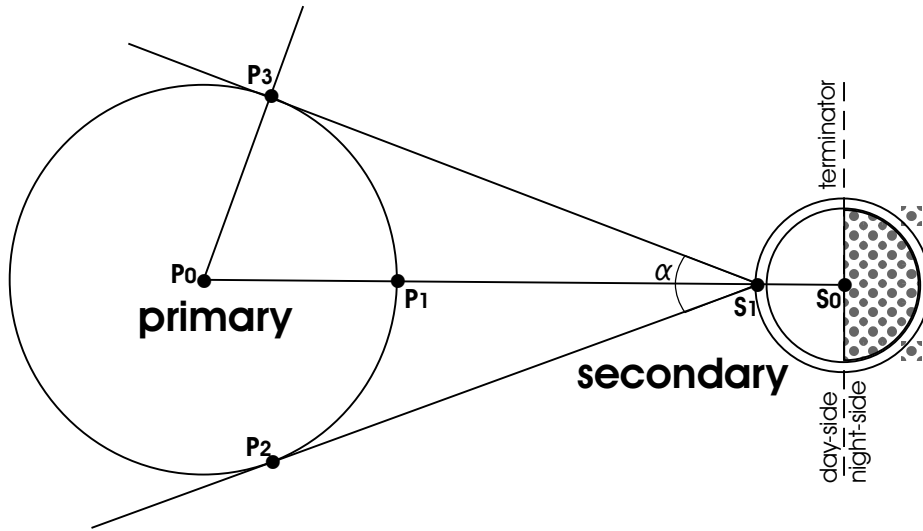
Figure 3.3: Basic geometry of a secondary irradiated by a primary on the substellar spot S_1. Light from P_2 over P_1 to P_3 reaches S_1 with an angle of up to $\alpha/2$. This figure is not to scale (geometry layout adapted from Barman 2002).

Please note that even though the total incident flux may be approximated as if it originating from a point source, the incident angles for the incident intensities will vary over a range equal to the angular size α of the primary measured at S_1 (see figure 3.3 for a sketch of α). For example, intensities originating from near the primary limb (P_2 or P_3 in figure 3.3) will have incident angles at S_1 equal to $\alpha/2$. Due to the well known limb darkening effect these intensities will differ from those originating from P_1. However for most systems $\alpha < 10°$, so this effect will be small (at a few percent at most).

There is yet another simplification. Since it is generally not possible to resolve individual surface elements of the secondary (or the primary by that), we will always observe the flux averaged over the entire visible hemisphere (which will be discussed in chapter 4.2 in more detail). At this point, the angular extension of the primary will not be observable and is ignored here.

Figure 3.4 illustrates the situation for a point S_2 at latitude θ, which is located somewhere between the substellar point and the terminator (defined as the plane separating the *day*- and *night*-side of the secondary). Only radiation incident at an angle δ (measured from the surface normal at S_2) is intercepted by the secondary, since rays with higher angles are not penetrating the atmosphere deep enough to be absorbed, but are just transmitted through[12]. Of course, even a glancing ray can deposit a small amount of energy in the outermost layer, but unless it does not penetrate down to $\tau = 1$ its energy contribution is insignificant to the total energy absorbed. If we therefore assume that $\theta \approx \delta$ then the distance between P_0 and S_2 is given by:

$$d^2 = r_\text{s}^2 + R^2 - r_\text{s}\,R\,\cos(\theta) \tag{3.15}$$

This simplification is strictly valid for $r_\text{s} \ll R$, where r_s is the radius of the secondary

---

[12]Transmitted spectra are currently under investigation by Mariana Wagner in a parallel PHOENIX project. However they are more important in extrasolar planets than close binary secondaries and are neglected here.
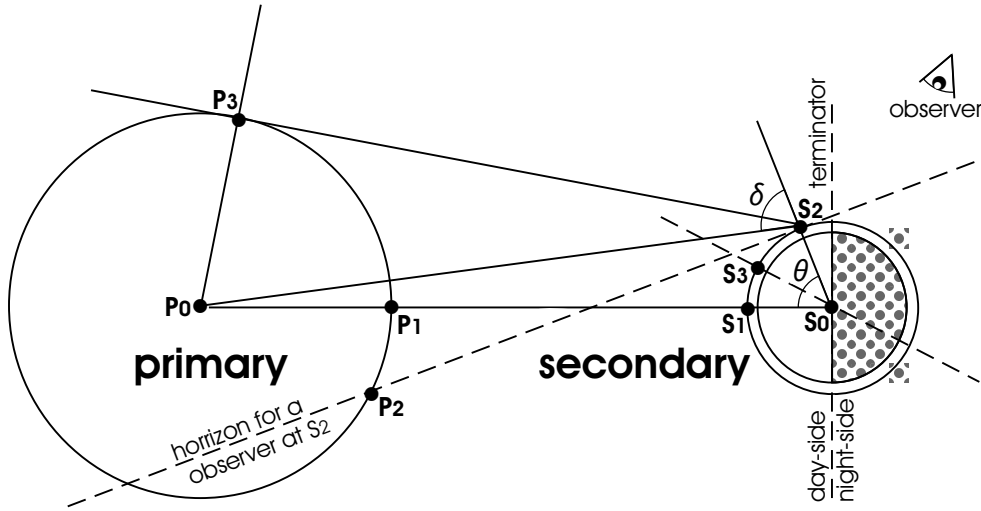
Figure 3.4: More detailed geometry of a secondary irradiated at a point S_2 by the primary (see also figure 3.3 for a simple case). In this case we get a penumbra-like effect, since an observer at S_2 can only see regions above his horizon (dashed intersecting line going through P_2 and S_2). An observer in the top right corner, who can only see light originating from from the upper half of the secondary (divided by the dashed intersecting line going through S_0 and S_3). This figure is not to scale (geometry layout adapted from Barman 2002).

and R the distance between primary and secondary centers, but even for $r_\mathrm{s} < R$ it is still acceptable.

The flux directed radially towards the center of the secondary (S_1) is therefore simply:

$$F^{\mathrm{inc}} = \left(\frac{r_\mathrm{p}}{d}\right)^2 F_\mathrm{p}\, \mu \qquad (3.16)$$

Note that at hight latitudes, i.e., θ close to $90°$, a small portion of the primary will be below the horizon of an observer at S_2. Normally this penumbra effect is negligibly small and hence not included in our models.

In some situations energy may be effectively redistributed across the surface of the secondary. This 'heat flux' could, e.g. happen due to winds or convection inside the atmosphere if there are strong variations in the irradiation. In this case a single model that produces an 'average' structure of the atmosphere can be used as approximation for the entire surface or portions of the surface. It is also possible to combine several models, each representing the 'average' structure of the atmosphere of a smaller portions of the surface, for an even more realistic 'patchwork' model if strong temperature variations are to be expected[13].

---

[13]See chapter 4.2 for a weighting of these patches and a demonstrations of different irradiation angles.

From equation 3.16 the total energy received on the secondary (per second) is simply:

$$\int_0^1 F(\mu)\, \mathrm{d}\mu = (\pi r_\mathrm{s}^2) F^\mathrm{inc}(\mu = 1) \tag{3.17}$$

If the energy is uniformly redistributed over the day hemisphere then the secondary effectively receives on average:

$$F_\mathrm{avg}^\mathrm{inc} = \frac{1}{2} F^\mathrm{inc}(\mu = 1) \tag{3.18}$$

Similarly if the energy is redistributed over the entire surface (day- and night-side) we get:

$$F_\mathrm{avg}^\mathrm{inc} = \frac{1}{4} F^\mathrm{inc}(\mu = 1) \tag{3.19}$$

And if there is no redistribution whatsoever due to a 'heat flux', then it is:

$$F_\mathrm{avg}^\mathrm{inc} = F^\mathrm{inc}(\mu = 1) \tag{3.20}$$

Defining a redistribution factor Q, which has a value between 1 (no redistribution), $\frac{1}{2}$ (half sphere = day-side) and $\frac{1}{4}$ (full sphere), we can write the average incident flux as:

$$F_\mathrm{avg}^\mathrm{inc} = Q \left(\frac{R_\mathrm{p}}{d}\right)^2 F_\mathrm{p} \tag{3.21}$$

3.3.2   Temperature correction

Our model atmosphere problem has an iterative nature that requires to apply a correction to the temperature at the end of each iteration so that the energy conservation constraint is satisfied. One simple but powerful technique for determining the correction is the Unsöld-Lucy (U-L) procedure (Lucy 1964), which was originally intended for plane parallel LTE atmospheres with the traditional 'isolated' upper boundary condition.
Requiring a time independent spherically symmetric solution for the correction method (Barman 2002) we start with that SSRTE:

$$\mu \frac{\partial}{\partial r} I_\nu + \frac{1 - \mu^2}{r} \frac{\partial}{\partial \mu} I_\nu = (\kappa_\nu + \sigma_\nu)\, \rho \left(S_\nu - I_\nu\right) \tag{3.22}$$

where most variables have been already defined after equation 3.5 in chapter 3.1.1, κ_ν is the absorption and σ_ν the scattering coefficient respectively.
The moments of the transfer equation are obtained by applying the operators $\frac{1}{2}\int_{-1}^{1} \mathrm{d}\mu$ and $\frac{1}{2}\int_{-1}^{1} \mu \mathrm{d}\mu$ to equation 3.22. These moments are:

$$-(\kappa_\nu + \sigma_\nu)\rho H_\nu = \frac{\partial}{\partial r}(K_\nu) + \frac{(3K_\nu - J_\nu)}{r} \qquad \text{and} \tag{3.23}$$

$$\frac{\partial}{\partial r}(r^2 H_\nu) = -(\kappa_\nu + \sigma_\nu)\rho r^2 (J_\nu - S_\nu) \tag{3.24}$$

where H_ν is the Eddington flux:

$$H_\nu = \frac{1}{2} \int_{-1}^{1} I_\nu \mu\, \mathrm{d}\mu \tag{3.25}$$

K_ν is the second moment of the radiation field:

$$K_\nu = \frac{1}{2} \int_{-1}^{1} I_\nu \mu^2 \, \mathrm{d}\mu \tag{3.26}$$

and J_ν is the mean intensity:

$$J_\nu = \frac{1}{2} \int_{-1}^{1} I_\nu \, \mathrm{d}\mu \tag{3.27}$$

Integrating over frequency and inserting the mean opacities:

$$\kappa_P = \frac{1}{B} \int_0^\infty \kappa_\nu B_\nu \, \mathrm{d}\nu \qquad \text{Planck mean}$$

$$\kappa_J = \frac{1}{J} \int_0^\infty \kappa_\nu J_\nu \, \mathrm{d}\nu \qquad \text{absorption mean}$$

$$\kappa_H = \frac{1}{H} \int_0^\infty (\kappa_\nu + \sigma_\nu) H_\nu \, \mathrm{d}\nu \qquad \text{flux mean}$$

and dropping the subscript ν to indicate wavelength integrated quantities, equation 3.23 and equation 3.24 become:

$$-\rho \, \kappa_H \, H = \frac{\partial}{\partial r}(K) + \frac{(3K - J)}{r} \qquad \text{and} \tag{3.28}$$

$$\frac{\partial}{\partial r}(r^2 H) = -\rho \, \kappa_P \, r^2 \left(\frac{\kappa_J}{\kappa_P} J - B \right) \tag{3.29}$$

where B_ν is the Planck function:

$$B_\nu = \frac{2h\nu^3}{c^2} \frac{1}{e^{\frac{h\nu}{kT}} - 1} \tag{3.30}$$

In the step above the expression for the source function has been used:

$$S_\nu = \frac{\kappa_\nu B_\nu + \sigma_\nu J_\nu}{\kappa_\nu + \sigma_\nu} \tag{3.31}$$

Equation 3.28 can be transformed into a first order linear equation by introducing the variable Eddington factor $f = \frac{K}{J}$. Afterwards equation 3.28 and equation 3.29 can be solved by introducing an integrating factor q, which is given by:

$$\ln(r^2 q) = \int_{r_c}^{r} \frac{3f - 1}{r' f} \, \mathrm{d}r' + \ln(r_c^2) \tag{3.32}$$

q is often called the *sphericality* function which was first introduced by Auer (1971). After applying the integration factor the equation 3.28 and equation 3.29 become:

$$\frac{\partial}{\partial \tau}(q \, f \, \mathbf{J}) = q \, \frac{\kappa_H}{\kappa_P} \, \mathbf{H} \qquad \text{and} \tag{3.33}$$

$$\frac{\partial}{\partial \tau}(\mathbf{H}) = \left(\frac{\kappa_J}{\kappa_P} \mathbf{J} - \mathbf{B} \right) \tag{3.34}$$

where the new variables are defined as:

- $\mathbf{J} = r^2 J$,

- $\mathbf{H} = r^2 H$,

- $\mathbf{B} = r^2 B$ and

- $\partial\tau = -\rho\ \kappa_P\ \partial r$.

The moment equations have now been reduced to functions of only a single independent variable, namely the Planck mean optical depth τ.

Let $\Delta\mathbf{B}(\tau)$ be the correction to the source function so that in the next iteration the correct target flux, i.e., $\mathbf{H}_{\text{target}}$, is obtained in each layer. The moment equations then become:

$$\frac{\partial}{\partial\tau}(q'\ f'\ \mathbf{J}') = q'\ \frac{\kappa'_H}{\kappa'_P}\ \mathbf{H}_{\text{target}}\qquad\text{and}\tag{3.35}$$

$$\frac{\partial}{\partial\tau}(\mathbf{H}_{target}) = \left(\frac{\kappa'_J}{\kappa'_P}\mathbf{J}' - \mathbf{B} - \Delta\mathbf{B}\right)\tag{3.36}$$

where $'$ denotes quantities to be determined at the end of the next iteration.

One of the benefits of introducing the means defined above is that their ratios do not change as much from one iteration to the next as the former variables do. Therefore one may assume that:

$$\frac{\kappa'_H}{\kappa'_P} = \frac{\kappa_H}{\kappa_P}\qquad\text{and}\qquad\frac{\kappa'_J}{\kappa'_P} = \frac{\kappa_J}{\kappa_P}\tag{3.37}$$

Using these approximations and further assuming $f = f'$ we may subtract equation 3.35 and 3.36 from 3.33 respectively 3.34 to obtain two equations with two unknowns:

$$\frac{\partial}{\partial\tau}(q\ f'\ \Delta\mathbf{J}) = q\ \frac{\kappa_H}{\kappa_P}\ \Delta\mathbf{H}\qquad\text{and}\tag{3.38}$$

$$\frac{\partial}{\partial\tau}(\Delta\mathbf{H}) = \left(\frac{\kappa_J}{\kappa_P}\Delta\mathbf{J} + \Delta\mathbf{B}\right)\tag{3.39}$$

where we use $\Delta\mathbf{J} = \mathbf{J} - \mathbf{J}'$ and $\Delta\mathbf{H} = \mathbf{H} - \mathbf{H}_{\text{target}}$. Note that by explicitly assuming $f = f'$, we are also automatically assuming $f = \frac{\Delta\mathbf{K}}{\Delta\mathbf{J}}$, which will be important later.

Now we can solve equation 3.38 for $\Delta\mathbf{J}$:

$$\Delta\mathbf{J}(\tau) = \frac{1}{q(\tau)f(\tau)}\left(q(0)f(0)\Delta\mathbf{J}(0) + \int_0^\tau q(\tau')\frac{\kappa_H(\tau')}{\kappa_P(\tau')}\Delta\mathbf{H}(\tau')\,\mathrm{d}\tau'\right)\tag{3.40}$$

We can now insert this $\Delta\mathbf{J}$ into the equation 3.39, solving it for $\Delta\mathbf{B}$, which yields an expression for the correction of the source function:

$$\begin{aligned}\Delta\mathbf{B}(\tau)\ =\ &\frac{\mathrm{d}\Delta\mathbf{H}}{\mathrm{d}\tau} + \\ &\frac{\kappa_J}{\kappa_P}\left(q(0)f(0)\Delta\mathbf{J}(0) + \int_0^\tau q(\tau')\frac{\kappa_H(\tau')}{\kappa_P(\tau')}\Delta\mathbf{H}(\tau')\,\mathrm{d}\tau'\right)\frac{1}{q(\tau)f(\tau)}\end{aligned}\tag{3.41}$$

Instead of computing the gradient of the flux it is a simple approach to use the fact that:

$$\frac{\mathrm{d}\Delta\mathbf{H}}{\mathrm{d}\tau} = \frac{\mathrm{d}\mathbf{H}}{\mathrm{d}\tau} = \frac{\kappa_J}{\kappa_P}\mathbf{J} - \mathbf{B}\tag{3.42}$$

Using the second Eddington approximation, i.e., $2\mathbf{H}(0) = \mathbf{J}(0)$, and inserting equation 3.42 into equation 3.41, the correction to the source function becomes:

$$\Delta\mathbf{B}(\tau) = \frac{\kappa_J}{\kappa_P}\mathbf{J}(\tau) - \mathbf{B}(\tau) + \tag{3.43}$$

$$\frac{\kappa_J}{\kappa_P}\left(2\,q(0)f(0)\Delta\mathbf{H}(0) + \int_0^\tau q(\tau')\frac{\kappa_H(\tau')}{\kappa_P(\tau')}\Delta\mathbf{H}(\tau')\,\mathrm{d}\tau'\right)\frac{1}{q(\tau)f(\tau)}$$

All quantities on the right hand side of equation 3.43 are available on completion of each iteration and hence the correction itself can be determined. The correction is then applied to the gas temperature directly and hence adjusts $\mathbf{B}(T)$.

One can use the Stefan-Boltzmann law and differentiate $\mathbf{B}$ with respect to T to obtain a temperature correction at each layer:

$$\Delta T(\tau) = \frac{\Delta\mathbf{B}(\tau)}{4\sigma T^3(\tau)r^2} \tag{3.44}$$

The first expression on the right hand side of equation 3.43, $\frac{\kappa_J}{\kappa_P}\mathbf{J}(\tau) - \mathbf{B}(\tau)$, is always small at large optical depth where the gas pressure and densities are high and $S \to B$. Therefore this first term only generates a correction in the optically thin parts of the atmosphere.

The second term on the right hand side of equation 3.43 in contrast is more important in optically thick regions and also ties the thermal structure to the prescribed target flux.

In the presence of irradiation, the atmosphere's upper boundary condition is altered to account for the incident flux as described in section 3.3.1. Since PHOENIX is supposed to conserve energy within its calculations, this implies that all of the energy received by the secondary due to irradiation from the primary must be reradiated into space again, either as a contribution to the thermal flux or as reflected light. As a result the target flux (H_{target}) is now given by:

$$H_{\mathrm{target}} = H_\nu^{\mathrm{ext}}(\tau) + \sigma T_{\mathrm{eff,\,s}}^4 \tag{3.45}$$

where H_ν^{ext} is the extrinsic Eddington flux ($H_\nu^{\mathrm{ext}} = \frac{1}{4\pi}F_\nu^{\mathrm{inc}}$) that has penetrated the secondary's atmosphere down to optical depth τ and $\sigma T_{\mathrm{eff,\,s}}^4$ is the total flux due solely to the secondary's intrinsic energy source.

The U-L temperature correction procedure that is derived above is formally correct even in the case of strong irradiation, as long as the correct target flux is supplied. However, the correction scheme can become unstable as discussed below when $H_\nu^{\mathrm{ext}}(\tau) >> \sigma T_{\mathrm{eff,\,s}}^4$. We need a few modifications to achieve stability in these cases.

The first modification concerns the Eddington approximation used to relate ΔJ with ΔK. If the total intensities are separated into intrinsic and extrinsic components then similarly the moments of the radiation field can also be separated into intrinsic and extrinsic components:

$$J = J_{\mathrm{ext}} + J_{\mathrm{int}} \quad , \quad K = K_{\mathrm{ext}} + K_{\mathrm{int}} \quad \text{and} \quad H = H_{\mathrm{ext}} + H_{\mathrm{int}} \tag{3.46}$$

Since the radiation from the primary is constant, i.e., no re-reflection effects are taken into account, the extrinsic components will also be constant from one iteration to the next apart from changes that will occur in the opacities due to changes in T. Therefore we get for the moments:

$$\Delta J = J_{\mathrm{int}}' - J_{\mathrm{int}} \quad , \quad \Delta K = K_{\mathrm{int}}' - K_{\mathrm{int}} \quad \text{and} \quad \Delta H = H_{\mathrm{int}}' - H_{\mathrm{int}} \tag{3.47}$$

Thus in the case of irradiation the equation 3.38 and equation 3.39 should involve only intrinsic mean intensities ($\mathbf{J}_{\text{int}}$). Since we used f to relate $\Delta\mathbf{J}$ with $\Delta\mathbf{K}$, f must also involve intrinsic quantities. Therefore f in equation 3.43 should be replaced by $f_{\text{int}} = \left(\frac{\Delta J}{\Delta K}\right)_{\text{int}}$ and assume that $f_{\text{int}} = f'_{\text{int}}$.

There is yet another modification necessary involving κ_H, which was defined as:

$$\kappa_H = \frac{1}{H}\int_0^\infty (\kappa_\nu \sigma_\nu) H_\nu \; \mathrm{d}\nu \tag{3.48}$$

The second correction term in equation 3.43 applies a "*torque*" on the temperature structure in a direction determined solely by the sign of ΔH, i.e., if $\Delta H(\tau) = H(\tau) - H_{\text{target}}(\tau) < 0$ then the temperature is too cool and must be increased. Generally this is true since all other quantities besides ΔH in the second term are normally positive. However, in the irradiated case this is not always true, especially for κ_H.

In the presence of large extrinsic flux the total flux ($H_{\text{total}} = H_{\text{int}} + H_{\text{ext}}$) may be negative. Since $|H_{\text{ext}}| \gg H_{\text{int}}$ and $H_{\text{ext}} < 0$, this will lead to $\Delta H < 0$. In case of cool secondaries the intrinsic flux and the opacities peak in the IR, while the extrinsic flux from the much hotter primary peaks in the optical or UV. Therefore it is possible that the total flux may be negative while $\int_0^\infty (\kappa_\nu + \sigma_\nu) H_\nu \; \mathrm{d}\nu$ is positive. In a situation where $H < 0$, $\Delta H < 0$ and $\kappa_H < 0$ the second term on the right hand side of equation 3.43 will lead to corrections in the wrong direction. This causes numerical instabilities.

The solution to the problem is rather straight forward if we consider the following changes. $\kappa_H H$ may be separated into intrinsic and extrinsic components as it was done for ΔJ and ΔK earlier already, leading to:

$$\kappa_H H = \kappa_H^{\text{int}} H_{\text{int}} + \kappa_H^{\text{ext}} H_{\text{ext}} \tag{3.49}$$

where the κ's are a short version for:

$$\kappa_H^{\text{int}} = \frac{1}{H_{\text{int}}}\int_0^\infty (\kappa_\nu + \sigma_\nu) H_\nu^{\text{int}} \; \mathrm{d}\nu \qquad \text{and} \tag{3.50}$$

$$\kappa_H^{\text{ext}} = \frac{1}{H_{\text{ext}}}\int_0^\infty (\kappa_\nu + \sigma_\nu) H_\nu^{\text{ext}} \; \mathrm{d}\nu \tag{3.51}$$

We assume that $(\kappa_H^{\text{ext}} H_{\text{ext}}) = (\kappa_H^{\text{ext}} H_{\text{ext}})'$, since this is the external flux. This changes the integrand in equation 3.43 which becomes:

$$\int_0^\tau q(\tau') \frac{\kappa_H^{\text{int}}(\tau')}{\kappa_P(\tau')} \Delta H(\tau') \; \mathrm{d}\tau' \tag{3.52}$$

where $\Delta H = H_{\text{int}} - H_{\text{target}}$ contains now only the intrinsic flux. κ_H^{int} will always be positive, since $H_{\text{int}} > 0$.

In principle κ_J in equation 3.39 could also be reduced to κ_J^{int} as described above for κ_H, but this does not lead to any major improvements in test cases.

When solving the radiation transfer equation (RTE) normally the entire, i.e., intrinsic and extrinsic, radiation field is considered and the total intensities are solved. In order to apply the above described modifications PHOENIX is solving the RTE *twice* per global iteration, once without and once including the external radiation field. The difference between the monochromatic intensities with and without the the extrinsic radiation gives the intrinsic

radiation. So once the separate intensities are known, the separate moments of the radiation field can be calculated and the proper temperature corrections determined.

For $\tau < 1$ the second correction term on the right hand side of equation 3.43 (entire bottom line) becomes more important with increasing external radiation and the modifications are crucial for the U-L procedure to work. For large external flux and an initial guess that is far from the correct structure, the unmodified U-L scheme will produce large oscillating temperature corrections and usually not converge. Sometimes even when the correct solution is used as the initial guess, the unmodified scheme moves away from the correct solution and stabilizes on a different structure, which does not satisfy radiative equilibrium. In contrast the modified scheme converges smoothly and normally reaches prescribed energy conservation accuracy.

Chapter 4

Geometry of irradiated stars[14]

The physical conditions in a variety of objects, e.g. hot extrasolar planets and close binaries, are fundamentally influenced by external irradiation. Often average spectra are used to model the heated day-side of such objects. This chapter presents a better approximation for extreme irradiation, especially if the day-side is very inhomogeneous and consists of much hotter and cooler 'patches' than the average model. Each patch results in a very different spectrum in that case. Therefore we construct a patch system that is able to represent such a situation more precisely.

If a standard spherical coordinate system is adopted, with the origin located at the center of the secondary and positive z-axis intersecting the center of the primary, then lines of constant latitude (measured from the z-axis) receive the same amount of incident flux from the primary. Points near the terminator (which lies in the $z = 0$ plane) receive less incident flux than the substellar point because of shallower incident angles and larger distances from the primary. Consequently, a single model atmosphere cannot be used to represent the entire irradiated face. PPRTE does not accurately treat radiation incident onto or emerging from regions near the limb. The SSRTE, however, ensures that the correct lower boundary conditions are met. Another major difference between PPRTE and SSRTE is that the incident radiation is not isotropic - extrinsic flux is only allowed to enter the atmosphere along a specific angle ω, which roughly corresponds to the latitude being modeled.

In static cases this latitude dependence leads to the development of patches of different temperatures on the 'day-side'. In order to combine spectra from all patches to a full visible stellar disk and to obtain a '1.5D' spectrum we need to calculate the weight of each of these patches. In the following we calculate the observed projected area from purely geometrical considerations. We take specific irradiation angles into account, this allows non-isotropic models to be used. We supply an IDL code to calculate the observed projected area for any patch given the phase and angle between surface and line of sight as well as a proper weighting for each by numerical integration. We end up with a simple approach to upgrade a 1D irradiation model to a quasi 1.5D model. This is a general method and can be applied to irradiated secondaries in close binaries.

---

[14]Parts of this chapter are published in Wawrzyn *et al.* (2009b).

4.1 Model / Geometry

A phase-resolved study can provide more information than a single spectrum of an isolated star. To construct phase-resolved model spectra we think of rings with constant θ as zones of constant temperature and show our set up of the geometry in figure 4.1.
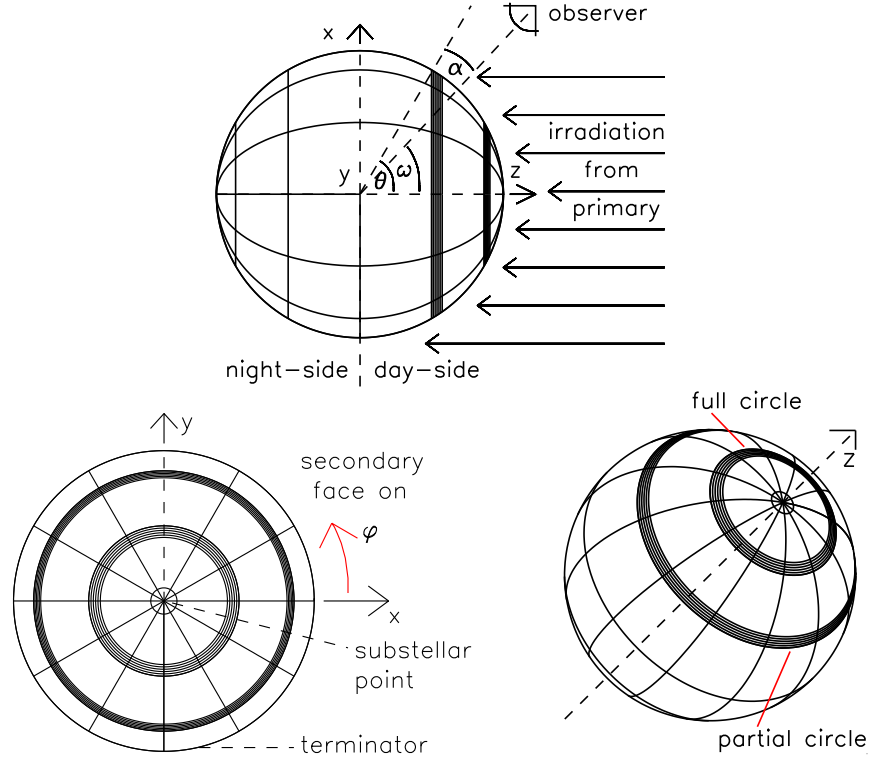

Figure 4.1: Some variables used to describe the problem. The substellar point is the closest point to the primary, rings around the substellar point receive the same incoming flux. The terminator is the border between day- and night-side. *Top:* side-view, *left:* the secondary seen from the center of the primary, *right:* another side-view to show one full and one partial circle on the surface.

Any point on the surface of the secondary is given in Cartesian coordinates by $\vec{r} = \begin{pmatrix} 1 \\ \theta \\ \varphi \end{pmatrix}$, normalizing the radius as $r_{\mathrm{s}} = 1$, and the observer's line-of-sight on this point $\vec{r}_{obs}$ (setting the observer in the xz plane):

$$\vec{r} = \begin{pmatrix} x \\ y \\ z \end{pmatrix} = r_{\mathrm{s}} \begin{pmatrix} \sin\theta\cos\varphi \\ \sin\theta\sin\varphi \\ \cos\theta \end{pmatrix} \quad \text{and} \quad \vec{r}_{obs} = \begin{pmatrix} x_{obs} \\ y_{obs} \\ z_{obs} \end{pmatrix} = \begin{pmatrix} \sin\omega \\ 0 \\ \cos\omega \end{pmatrix} \tag{4.1}$$

The angle α between both vectors in equation 4.1 is hence simply given by:

$$\cos\alpha = \sin\theta\cos\varphi\sin\omega + \cos\theta\cos\omega \tag{4.2}$$

We want to calculate the surface area A between the latitudes θ_1 and θ_2, which is itself seen under the angles between α_1 and α_2:

$$A(\theta_1, \theta_2, \alpha_1, \alpha_2) = \int_{\theta_1}^{\theta_2} \int_{\varphi(\alpha_1)}^{\varphi(\alpha_2)} r_{\rm s}^2 \sin\theta \cos\alpha(\varphi) \; {\rm d}\varphi \; {\rm d}\theta \tag{4.3}$$

The problem is assumed to be symmetric to the xz-plane so we integrate only over one hemisphere ($\alpha \geq 0$) and multiply the result by 2.

Grazing views happen under $\alpha = -\frac{\pi}{2}$ or $+\frac{\pi}{2}$ and we need to distinguish between full, partial and not visible circles of latitude. Therefore, the integration boundaries for any 'patch' to be observable are:

$$|\omega - \theta| \leq \alpha \leq \min(|\omega + \theta|, \pi/2) \tag{4.4}$$

If the conditions are fulfilled we get our $\varphi(\alpha)$ simply from equation 4.2:

$$\varphi(\alpha) = \arccos\left(\frac{\cos\alpha - \cos\theta \cos\omega}{\sin\theta \sin\omega}\right) \text{ for } \theta \neq 0, \omega \neq 0 \tag{4.5}$$

4.2 Isotropic radiation

If the resulting spectra are radiated isotropically, i.e. the observed spectrum is independent of α, the integration goes over all visible areas of φ and equation 4.3 can be simplified:

$$A_{\rm total}(\theta_1, \theta_2) = A_{\rm full\ circles\ day-side}(\theta_1, \theta_2) + A_{\rm partial\ circles}(\theta_1, \theta_2)$$
$$+ A_{\rm full\ circles\ night-side}(\theta_1, \theta_2) \tag{4.6}$$

Angles θ belong to fully visible circles on the day-side for

$$0 \leq \theta \leq \left|\frac{\pi}{2} - \omega\right| \quad \text{with } \omega < \frac{\pi}{2} \text{ , on the night-side for}$$

$$\left|\frac{3\pi}{2} - \omega\right| \leq \theta \leq \pi \quad \text{with } \omega > \frac{\pi}{2} \text{ and to partial circles for}$$

$$\left|\frac{\pi}{2} - \omega\right| < \theta \leq \left|\frac{\pi}{2} + \omega\right| \quad \text{with } \omega < \frac{\pi}{2} \text{ and}$$

$$\left|\omega - \frac{\pi}{2}\right| < \theta \leq \left|\frac{3\pi}{2} - \omega\right| \quad \text{with } \omega > \frac{\pi}{2} \text{ .} \tag{4.7}$$

There are, however, always only full circles visible on either the day- or the night-side. The others are, together with the missing part of the partially visible circles, on the opposite hemisphere, turned away from the observer.

For only partially visible circles the φ integration goes up to $\alpha = \frac{\pi}{2}$, since there is always a 'grazing shot' when the circle moves out of sight, simplifying equation 4.5 to:

$$\varphi_1 = \arccos(-\cot\theta \cot\omega) \tag{4.8}$$

Using this to decompose equation 4.6 in separate integrals for full and partial circles, where the boundaries θ_1 and θ_2 are either split and adjusted according to the conditions above or both are within one type of circle, we get:

$$A_{\text{total}} = \underbrace{2 \cdot \int_{\theta_1}^{\theta_2} \int_0^\pi r_{\text{s}}^2 \sin\theta (\sin\theta \cos\varphi \sin\omega + \cos\theta \cos\omega) \mathrm{d}\varphi \, \mathrm{d}\theta}_{A_{\text{full circles}}}$$

$$\underbrace{+ 2 \cdot \int_{\theta_1}^{\theta_2} \int_0^{\varphi_1} r_{\text{s}}^2 \sin\theta (\sin\theta \cos\varphi \sin\omega + \cos\theta \cos\omega) \mathrm{d}\varphi \, \mathrm{d}\theta}_{A_{\text{partial circles}}} \qquad (4.9)$$

We now treat the two integrals of equation 4.9 separately, skipping the factor 2 for now and resolving the first part, where $A_{\text{full circles}} = A_{\text{fc}}$:

$$\begin{aligned}
A_{\text{fc}} &= \int_{\theta_1}^{\theta_2} r_{\text{s}}^2 \sin^2\theta \sin\omega \sin\varphi + r_{\text{s}}^2 \sin\theta \cos\theta \cos\omega \, \varphi \, \mathrm{d}\theta \\
&= \int_{\theta_1}^{\theta_2} r_{\text{s}}^2 \sin^2\theta \sin\omega [0 - 0] + r_{\text{s}}^2 \sin\theta \cos\theta \cos\omega [2\pi - 0] \mathrm{d}\theta \\
&= r_{\text{s}}^2 2\pi \cos\omega \, \frac{1}{2} \sin^2\theta \, \Big|_{\theta_1}^{\theta_2} \qquad (4.10)
\end{aligned}$$

For the second part of the integral $A_{\text{partial circles}} = A_{\text{pc}}$ we put in the integration limits of φ, but we end up with a more difficult expression:

$$\begin{aligned}
A_{pc} &= \int_{\theta_1}^{\theta_2} r_{\text{s}}^2 \sin^2\theta \sin\omega [\sin(\arccos(-\cot\theta\cot\omega)) - \sin(-\arccos(-\cot\theta\cot\omega))] \\
&\qquad + r_{\text{s}}^2 \sin\theta \cos\theta \sin\omega [\arccos(-\cot\theta\cot\omega) - (-\arccos(-\cot\theta\cot\omega))] \, \mathrm{d}\theta \\
&= \int_{\theta_1}^{\theta_2} r_{\text{s}}^2 \sin^2\theta \sin\omega \, 2\sqrt{1 - \cot^2\theta \cot^2\omega} \\
&\qquad\qquad + r_{\text{s}}^2 \sin\theta \cos\theta \cos\omega \, 2[\pi - \arccos(\cot\theta\cot\omega)] \, \mathrm{d}\theta \qquad (4.11)
\end{aligned}$$

Using $\arccos x = \arcsin\sqrt{1+x^2}$ for $0 \le x \le 1$ and $\arccos(-x) = \pi - \arccos(x)$ in the last step.
The θ integration in equation 4.11, however, can be solved numerically.

4.3 Coverage

Since there might be an eclipse by the primary, we check for this situation and subtract covered parts of the secondary. This is illustrated in figure 4.2 respectively figure 4.3.
When the primary transit over the secondary surface begins, then coverage first happens to full circles on one side which thus become partial circles and are eventually covered completely. We need a function $\varphi(\theta)$ that uses radii, distance and angle in the plane of motion to adjust the integration limits accordingly. We parameterize the edge of the primary as projected on the secondary in the plane of sky with x', y', z' for a circle, where r_{p} is the radius of the primary and R the distance between both components:

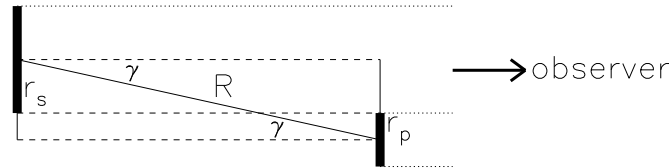$$y' = \sqrt{r_{\text{p}}^2 - (x' + R\sin\omega)^2} \qquad (4.12)$$

Figure 4.2: A sketch of a beginning or ending secondary eclipse, where both stars are only seen as flat discs represented as thick lines from this side-view. r_p, r_s and R give the radii respectively separation, while γ is the total angle between primary-secondary-axis and the line-of-sight, a combination of phase and inclination, which are perpendicular and independent of each other.
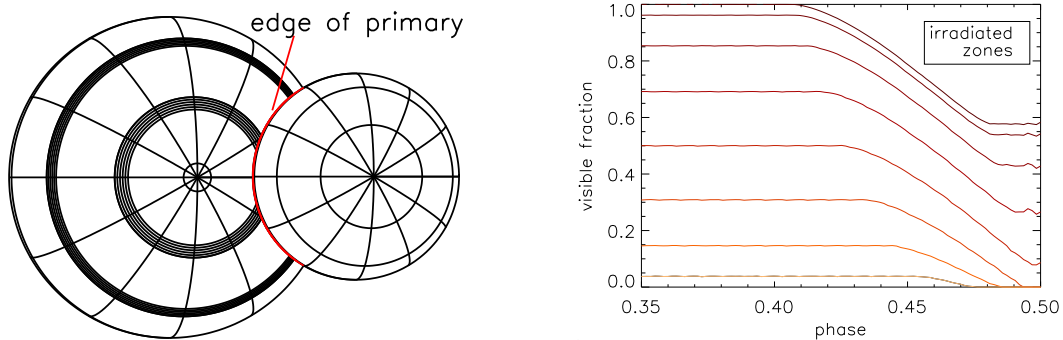

Figure 4.3: *Left:* The smaller primary covers some circles on the larger secondary, requiring an adjustment to the integration boundaries. This sketch could represent either start or end of an eclipse, since this problem is symmetric to the substellar point. *Right:* The visible fraction of different rings close to and during primary eclipse (phase $p = 0.5$). Outer rings are covered first, inner ones later. Full coverage depends on inclination and size ratio. Exemplary parameters are: $r_s = 1$, $r_p = 0.65$, $R = 3$ and $i = 90°$ The color-code is similar to the example in figure 4.4, so yellow is the hottest area (the substellar point) and cooler areas are becoming redder and darker.

Then we rotate this system around the y-axis to our old set of coordinates:

$$\begin{pmatrix} x' \\ y' \\ z' \end{pmatrix} = \begin{pmatrix} \sin\theta\cos\varphi\cos\omega + \cos\theta\sin\omega \\ \sin\theta\sin\varphi \\ \cos\theta\cos\omega - \sin\theta\cos\varphi\sin\omega \end{pmatrix} \tag{4.13}$$

We calculate ω, the angle between line-of-sight and the line between the centers of mass of both stars, i.e., the z-axis, from the phase p and the inclination i by[15]:

$$\begin{pmatrix} \cos p \ \cos i \\ \sin p \\ \cos p \ \sin i \end{pmatrix} \begin{pmatrix} 0 \\ 0 \\ 1 \end{pmatrix} = \cos p \sin i = \cos \omega \quad \Longrightarrow \quad \omega = \arccos(\cos p \cos i) \quad (4.14)$$

No coverage occurs if:

$$\sqrt{(R \ \sin i)^2 + (R \ \sin p)^2} \geq \ r_{\mathrm{p}} + r_{\mathrm{s}} \quad \Longrightarrow \quad p \geq \arcsin \sqrt{\left(\frac{r_{\mathrm{p}} + r_{\mathrm{s}}}{R}\right)^2 - \sin^2 i} \quad (4.15)$$

where r_{s} is the radius of the secondary.
R is usually significantly larger than the sum of r_{p} and r_{s}, hence an eclipse only happens for inclinations i close to $90°$, which can be approximated as:

$$p \ \geq \ \arcsin\left(\frac{r_{\mathrm{p}} + r_{\mathrm{s}}}{R}\right) \quad\quad\quad\quad (4.16)$$

4.4   Applications

Using the presented formalism we will attempt to model close binaries combining spectra with different irradiation angles. We will add them up using phase specific weights in order to match observations like the one in figure 4.4.

Three synthetic models, with varying irradiation angles of $\cos \theta = 1$, 0.75 and 0.5, which represents $\theta = 0°$, $40°$ and $60°$ measured toward the normal vector of the secondary surface, are shown in figure 4.5. All models use a $125\,000$ K hot primary at a center-to-center distance of roughly 2.5 R$_\odot$ to irradiate a much cooler secondary component (3400 K). Model parameters are identically to the fit of UU Sagittae presented by Wawrzyn *et al.* (2009a) (see chapter 5), except for abundances which were kept at solar photospheric values. The species H , He , C , N and O are handled in NLTE, while all others are LTE. The wavelength range was selected, because it is rich in emission lines and covers the "broad emission feature" which is also discussed in chapter 5.

All emission lines of the same ion type in LTE behave the same, e.g. Ne II, Si IV or Fe IV all show the same angle dependence, since they are only determined by the temperature structure. In NLTE there are differences in the emission of C , N and O for varying angles. Compare, e.g. N III $\lambda\,4641.9$ Å versus $\lambda\,4643.2$ Å or C III $\lambda\,4648.7$ Å versus $\lambda\,4652.8$ Å.

As one can see not only the different temperature structure due to steeper irradiation angles in LTE, but also NLTE effects can influence the outcome of the spectrum. This indicates that the presented method is necessary to acquire accurate results in the situation of massive irradiation.

---

[15]The phase is named p here to avoid confusion with the angle φ. An inclination of $90°$ means edge-on.
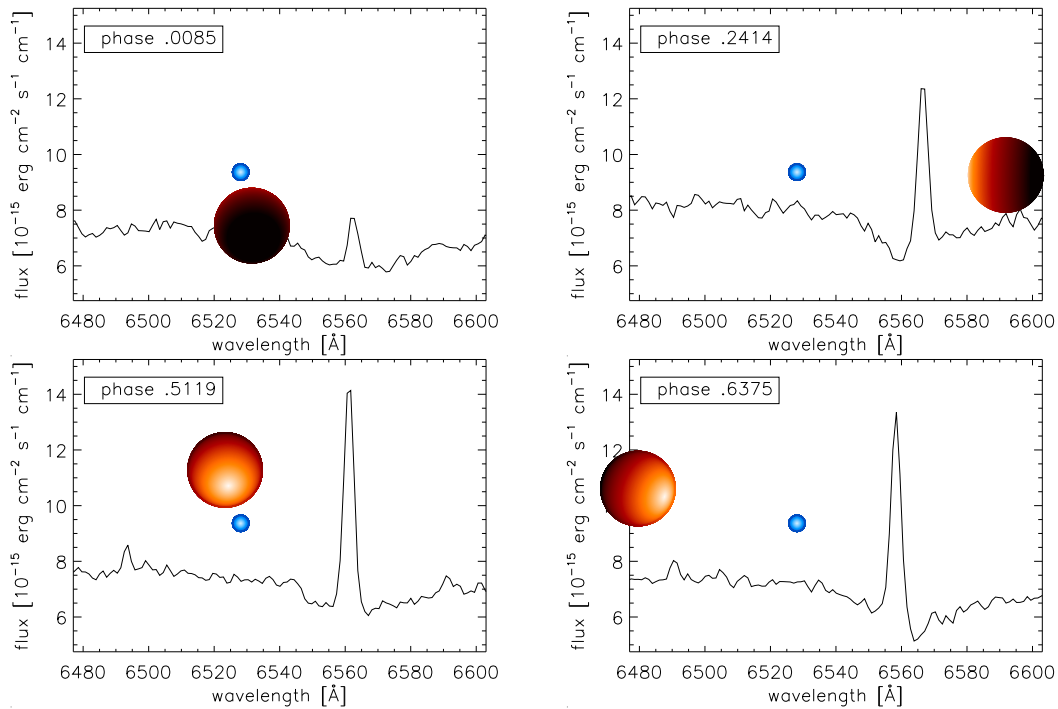
Figure 4.4: Observed phase variation in H_α in GD245 (Schmidt *et al.* 1995) shown for four selected configurations. Sizes of sketch are not to scale, though no eclipse occurs in this case as can be seen on the left figures.

Figure 4.5: Three spectra with different irradiation angles ($0°$, $40°$ and $60°$ measured toward the normal vector of the secondary surface) on the same object, using an $125\,000$ K irradiation source at roughly 2.5 R$_\odot$ distance.

4.5   Prerequisites and scenarios

Model prerequisites are purely geometrical:
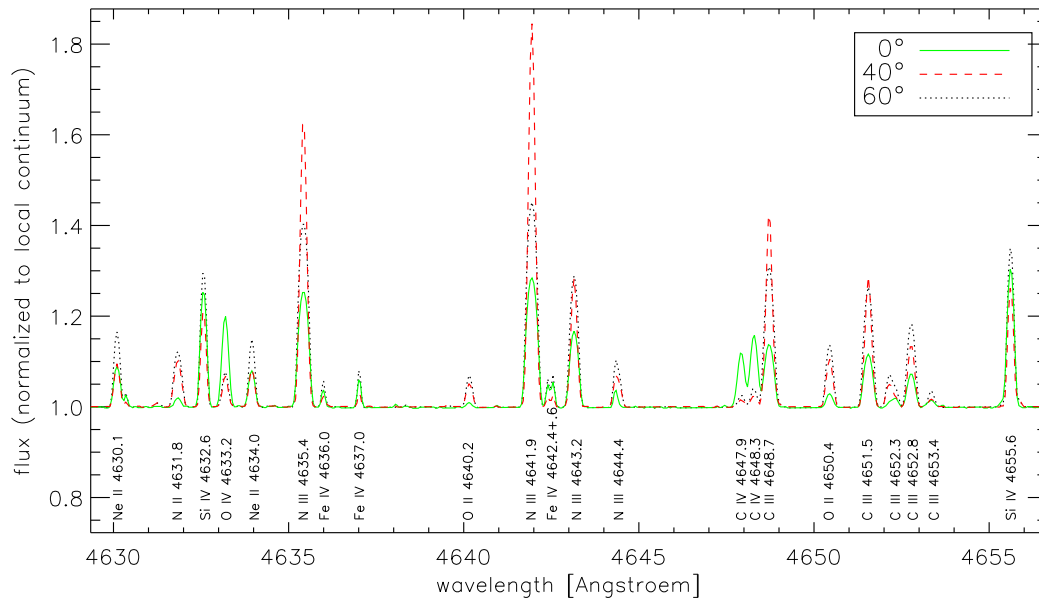The objects in question must be spherical and their structure rotationally symmetric to the z-axis. Otherwise this is a purely geometric solution.

Astrophysical scenarios:
We consider irradiated objects, e.g. secondaries in close binary systems, where rings of $\theta = \mathrm{const}$ represent areas of $T_{\mathrm{eff}} = \mathrm{const}$ in the atmospheric structure. This requires either a rapid response of the secondary to changing irradiation conditions or a tidally locked system on circular orbit, where the irradiation angle and the incoming flux stays the same for each patch all the time and hence an equilibrium has been reached. The irradiation on the secondary does not have to be uniform, as long as it has rotational symmetry around the z-axis, in other words only rings of constant θ need to have the same temperature everywhere. Furthermore, energy transport along the system by winds or radiation is allowed, as long as its strength does not depend on the angle φ. Complications of this kind have to be taken into account by the model code, which generates spectra emitted by each patch under the viewing angle α. With the geometrical considerations presented here, different 1D spectra can be combined to generate a 1.5D patchwork, a better approximation to real multi-dimensional situations.
This work complements earlier models (Eddington 1926; Kopal 1959; Napier 1968; Wood 1973), which consider the problem from a point of view on the secondary object.

4.6   Code

The IDL code for this calculation is included in Appendix D. It is also available in electronic form at the following web address:
`ftp://ftp.hs.uni-hamburg.de/pub/outgoing/wawrzyn/geom.pro`

Chapter 5

UU Sagittae[16]

The standard stellar model atmosphere ignores the influence of external radiation. This assumption, while sufficient for most stars, fails for many short-period binaries.

Setting up combined model atmospheres for close binaries, we want to constrain the parameters of both components, especially in the case of a hot primary component strongly influencing its cool secondary companion. This situation can be found after common envelope evolution (CEE). The status of both components today allows to retrace the CEE itself. We use our stellar atmosphere code PHOENIX, which includes the effect of irradiation in its radiation transport equation to investigate the close binary star UU Sge. We combine our calculated spectra of both components, weighted by their visible size, and adjust the input parameters until reasonable agreement with observations is reached.

We derive a range of $80\,000$–$85\,000$ K for the effective temperature of the primary ($T_{\mathrm{eff,\,p}}$) and give a rough estimate for the primary's abundances, particularly the nitrogen enrichment. The heated day-side of the secondary has an apparent 'effective' or equilibrium temperature of $24\,000$–$26\,000$ K, nearly independent of its intrinsic luminosity. It shows an enhancement in nitrogen and carbon.

The evolution the primary and secondary stars were greatly influenced by the presence of the other. Radiation from the primary on the secondary's day-side is still an important factor in understanding the secondary's atmospheric structure.

5.1   Introduction

UU Sagittae (UU Sge) is the central nucleus of the old planetary nebula (PN) Abell 63 (Abell 1966). This nucleus is a total-eclipsing close binary (CB) that has passed through the common-envelope phase and is currently a pre-cataclysmic variable (pre-CV). The primary has been classified as an O subdwarf (sdO) that has not yet contracted to a white dwarf (WD) (Bond *et al.* 1978). The secondary companion is thought to be an unevolved main-sequence star (MS) by its mass, probably a mid K- to mid M-dwarf (dKV–dMV), but the luminosity of the night-side, due to horizontal heat transfer beyond the terminator, is comparable to that of a late A- to early F-star (dAV–dFV). The PN is faint but still detectable, where a typical PN lifetime before dispersion is about $3 \cdot 10^4$ years (de Kool and Ritter 1993; Iben and Tutukov 1993). The PN spectrum is unusual in that the H Balmer series, O III (5007, 4959, and

---

[16]Content of this chapter in Wawrzyn et al. 2009, submitted to A&A, layout changed to match dissertation one-column style, currently in referee stage with minor corrections required

4363 Å) and He I 5876 Å are the only strong lines (Miller *et al.* 1976). It should hence not contaminate the observed spectra of the nucleus. UU Sge's unique 'totally eclipsing' nature allows the determination of well-constrained light-curve solutions and, in combination with accurate radial velocity data, the derivation of reliable geometrical parameters for the system. Even though the geometry is well constrained, different quality measurements and diverse physical implications have produced a variety of mass and temperature estimates in the past, as discussed in Sect. 5.2.

The reasonably well constrained geometry and observationally accessible nature of UU Sge makes this system a useful laboratory for studying the effects of irradiation in a close binary. The system's hot primary, the cooler secondary and the proximity of both components make the effects of irradiation an important feature. A crucial aspect of UU Sge is that none of the indications associated with mass transfer (e.g. accretion disk, bright spot, or boundary layer) are observed, which would otherwise make the irradiation geometry asymmetric and far more difficult to characterise.

Another important feature of UU Sge is that the primary sdO is much larger than a fully evolved WD; the size of the primary is almost comparable to that of the companion. Therefore the estimated T_{eff} ratio of $\sim 90\,000$ K : $6\,000$ K by Pollacco and Bell (1993, hereafter PB93) and Bell *et al.* (1994, hereafter BPH94) leads directly to a luminosity ratio of approximately 10^4 between the primary and the (faint) night-side of the secondary close to the primary eclipse.

The geometry allows the fundamental parameters of the primary, i.e., $T_{\mathrm{eff,\,p}}$, $\log g_{\mathrm{p}}$ and chemical composition, to be decoupled from the secondary, even though they are not spatially resolved in the observation. The primary near its eclipse can be dealt with in a first step, neglecting the very small influence of the secondary for the moment. The primary spectrum can then be used to irradiate the secondary to model its day-side in a second step, since reflection and heating effects from the secondary on the primary should be negligible.

The sum of primary and secondary spectrum must reproduce the emission near the secondary eclipse; this defines the properties of the secondary.

In the following we do not concentrate on the common envelope evolution (CEE) (e.g. Paczynski 1976; Iben and Livio 1993; Warner 1995; Livio 1996; Taam and Sandquist 2000). This is the mechanism that is thought to expel the envelope of the Asymptotic Giant Branch (AGB) star (Rasio and Livio 1996; Sandquist *et al.* 1998) and due to this momentum loss produce CBs; though the CEE surely has influenced what we observe in UU Sge today.

UU Sge has conserved its properties basically unaltered since the end of the CEE, because it is a pre-CV and no other major physical processes such as additional mass accretion has taken place yet. However, there are ongoing discussions upon this topic and alternative momentum loss mechanisms are suggested by e.g. Nelemans and Tout (2005); Taam and Ricker (2006); Webbink (2008); Beer *et al.* (2007).

For a review about detached binaries, physical processes in close binary systems, and general three-dimensional fluid dynamics in binary systems see Marsh (2000); Claret and Giménez (2001); Beer and Podsiadlowski (2002).

The paper is structured as follows: In Sect. 5.2 we summarise the properties of UU Sge and in Sect. 5.3 show the observation that we model. Section 5.4 contains a short description of the stellar atmosphere code used and the assumptions made for starting values. Section 5.5 presents the primary and secondary results, followed by a discussion in Sect. 5.6. Section 5.7 concludes with a summary.

5.2 Properties of UU Sge

The first to suggest that UU Sge was an eclipsing binary was Hoffleit (1932), who found it only twice at minimum on 25 plates. More than 30 years later UU Sge was listed as an eclipsing binary in the PN catalogue of Abell (1966); however, not until Bond (1976) found the PN Abell 63 and the variable star UU Sge at the same position was the true nature of the system established. Early predictions for the system parameters were published by Budding and Kopal (1980), Budding (1981), and Ritter (1986). Others followed shortly after. Further improvements were made by PB93 who measured the effective temperature ($T_{\mathrm{eff,\,p}}$) of the primary to be $87\,000$ K and improved radial velocities that indicated an oversized secondary ($\sim 2.0 - 2.5$ times larger than a corresponding zero-age MS star) leading to important changes to the inferred geometry.

One year later the secondary was, for the first time, observed directly during a primary eclipse, which lasts some 14 minutes. This measurement provided an intrinsic temperature of 6250 K for the secondary's unilluminated night-side (BPH94). There is an ongoing effort to constrain system parameters further (e.g. more recent work by Afşar and Ibanoğlu 2004; Pustynski and Pustylnik 2005) since the uncertainties still do not allow the evolutionary status to be pinpointed.

Table 5.1: A selection of former derived values of UU Sge. (*: see comment of Iben and Tutukov (1993) at the end of Sect. 5.2.)

Parameter	Bond	Ritter	Walton	Pollacco	Afşar	Pustynski	this paper
m_{v} [mag]	15	n.a.	n.a.	14.67	n.a.	n.a.	n.a.
d [pc]	150–2000	n.a.	~ 3600	2400 ± 400	n.a.	n.a.	[2400]
L [L$_{\odot}$]	100	n.a.	~ 2400	$(19\,000)^{*}$	n.a.	n.a.	[3000–6000]
m_{P} [M$_{\odot}$]	0.9	0.7	0.565	0.63 ± 0.06	n.a.	0.63 ± 0.06	(0.63)
r_{P} [R$_{\odot}$]	0.4	n.a.	n.a.	0.33 ± 0.01	$(0.145 \pm 0.001) \cdot R$	0.33–0.34	(0.34)
$\log g_{\mathrm{P}}$ [cm s^{-2}]	n.a.	n.a.	5.0	5.18 ± 0.05	n.a.	n.a.	4.5–5.0
$T_{\mathrm{eff,\,p}}$ [K]	14 000–60 000	n.a.	$\sim 50\,000$	$87\,000 \pm 13\,000$	$99\,896 \pm 2850$	80 000–85 000	75 000–85 000
m_{s} [M$_{\odot}$]	0.7	0.5	0.7	0.29 ± 0.04	n.a.	0.29 ± 0.04	(0.29)
r_{s} [R$_{\odot}$]	0.7	0.6	n.a.	0.53 ± 0.02	$(0.229 \pm 0.001) \cdot R$	0.54	(0.53)
$\log g_{\mathrm{s}}$ [cm s^{-2}]	n.a.	n.a.	n.a.	4.43 ± 0.06	n.a.	n.a.	(4.5)
$T_{\mathrm{eff,\,s}}$ [K]	n.a.	n.a.	n.a.	6250 ± 250	7250 (fixed)	5500–5600	[6000]
$T_{\mathrm{eq,\,s}}$ [K]	n.a.	n.a.	n.a.	17000 ± 2000	n.a.	n.a.	23 000–26 000
R [R$_{\odot}$]	~ 3	2.98	n.a.	[2.46]	n.a.	n.a.	(2.46)
$q = m_{\mathrm{s}}/m_{\mathrm{P}}$	n.a.	n.a.	n.a.	0.46	n.a.	n.a.	n.a.
P [h]	11.16	11.161656	n.a.	11.162	n.a.	n.a.	[11.162]
i [$^{\circ}$]	n.a.	n.a.	n.a.	n.a.	87.620 ± 0.124	88	[87.5]

Bond *et al.* (1978); de Kool and Ritter (1993); Walton *et al.* (1993); PB93/BPH94; Afşar and Ibanoğlu (2004); Pustynski and Pustylnik (2005) and this paper

Table 5.1 shows a compilation of previously derived parameters of UU Sge from Bond *et al.* (1978), de Kool and Ritter (1993), Walton *et al.* (1993), PB93/BPH94, Afşar and Ibanoğlu (2004), Pustynski and Pustylnik (2005), and our results for comparison. Radii of both components are available from all but one of the studies, as Afşar and Ibanoğlu (2004) only published a ratio of the primary-secondary separation R from the center-of-mass, rather than the individual separations. We used Kepler's 3rd law to fill in missing separations where possible. The last two columns use the geometry derived by PB93. Numbers in round brackets in the last column are fixed input parameters and not derived by our model. Values in squared brackets are only used outside the model calculation. Note that we do not list a value of $T_{\mathrm{eff,\,p}} = 120\,000$ K by Shimansky *et al.* (2008), which is discussed at a later.

The parameters are (top to bottom) visual magnitude m_V [mag], distance to Earth d [pc], luminosity L [L$_{\odot}$], mass m [M$_{\odot}$], radius r [R$_{\odot}$], logarithmic surface gravity $\log g$ [cm s^{-2}], effective temperature T_{eff} [K] for primary ($_{\mathrm{p}}$) and secondary ($_{\mathrm{s}}$), equilibrium temper-

ature T_{eq} [K] on day-side of secondary, separation R (center to center) [R$_\odot$], mass ratio q of components, period P [h], and system inclination i [°], where $90°$ is edge on. Note that many of these parameters are strongly coupled and, even though most ratios are well determined, an error in, e.g., radial velocity does not only affect the separation but also the radii and masses of the system and, consequently, other parameters such as gravity, luminosity, and irradiation.

The effective temperatures of both components are especially difficult to determine and a case can be made for higher as well as lower temperatures, using e.g. the excitation of the PN or missing opacities of other lines when using Balmer line ratios (Exter *et al.* 2005, and references therein). If cooler estimates are correct, the primary may be a non-degenerate helium remnant of a star of initial mass of about 5 M$_\odot$ (Iben and Tutukov 1989). If instead hotter estimates turn out to be true, the hot component of UU Sge could be a star with a degenerate C O core and a non-degenerate helium envelope which is burning helium at its base (Iben and Tutukov 1993). According to Iben and Tutukov (1993) a luminosity of $19\,000$ L$_\odot$ found by PB93 is likely too high, since it exceeds the Eddington limit for a star of that predicted mass; they suggest $10^3 - 10^4$ L$_\odot$.

5.3   Observations

Figure 5.1 shows two spectra (continuum normalised) of UU Sge obtained during phases close to primary and secondary eclipse along with the difference in flux. The wavelength coverage is 4185–4770 Å.

Data was taken with the spectrograph ISIS of the William Herschel Telescope and first published in PB93, where details on the observations and data reduction procedures are given. Radial velocity shifts at these phases are unimportant since the movement is perpendicular to line-of-sight. Stellar velocity shifts were corrected to the theoretical wavelengths.

We define phase $\varphi = 0.0$ (inferior conjunction) to coincide with primary eclipse, where the larger secondary occults the primary and orients its non-irradiated side to the observer. At phase $\varphi = 0.5$ (superior conjunction) a secondary eclipse occurs as the smaller primary transits the heated day-side of the secondary. The observations were taken close to but not exactly at $\varphi = 0.0$ and $\varphi = 0.5$, so both components were visible during the exposures (PB93). The first spectrum shows the primary and the cold night-side of the secondary. The second spectrum also includes the primary but this time with the hot day-side of the secondary. The bottom panel in Fig. 5.1 displays the difference between hot day-side and cold night-side of the secondary, since the primary should roughly cancel out. Identified H I, He II, and N V absorption features are marked, where 'IS' means the unknown diffuse interstellar band at 4430 Å that was not taken into account for the fitting of our model spectra.

Also indicated are where our synthetic spectra predict lines. In particular, we indicate the lines O IV $\lambda4390.7$, 4555.8, 4633.2 Å, C IV $\lambda4442.7$, $4647.9 + 4648.3$ Å, Si IV $\lambda4632.6$ (blend with O), 4655.6 Å and N V $\lambda4750.1 + 4751.8$ Å.

As is evident in the bottom panel of Fig. 5.1, only two wavelength ranges are especially interesting with strong 'differential' emission remaining from the secondary's day-side: a double feature around 4340 Å, which results from emission 'filling-in' in the H$_\gamma$ wings and a maybe multiple feature between 4630 and 4655 Å. These are investigated in Sect. 5.5.2 in more detail.
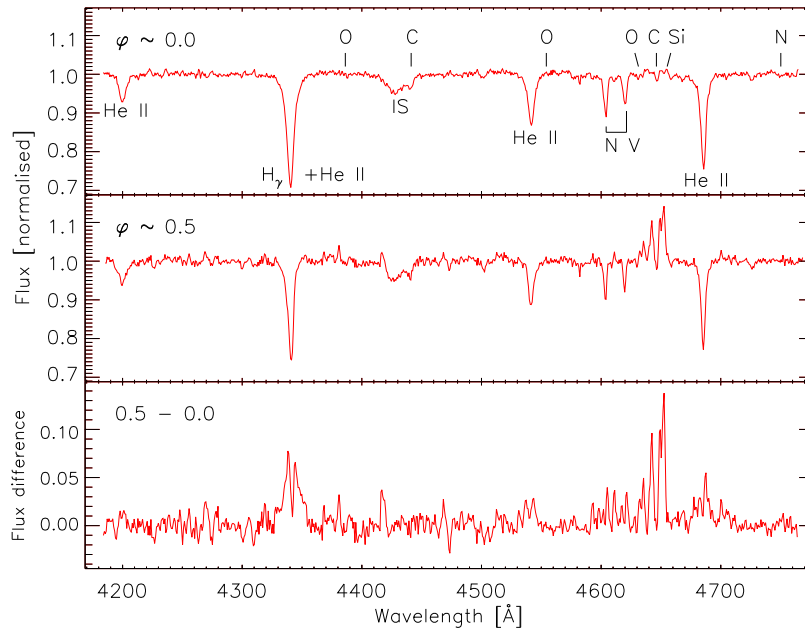
Figure 5.1: Observed spectrum (PB93) close to the primary eclipse (top), close to the secondary eclipse (middle), and the difference spectrum (bottom).

5.4 The model

5.4.1 The code

We use a modified version of the PHOENIX 15.04 stellar atmosphere code (Hauschildt and Baron 1999b) for the calculations presented here. This is capable of modeling both the hot sdO (Aufdenberg 2001) and the cooler MS companion (Allard *et al.* 2001). The code includes an irradiation mode (Barman *et al.* 2004, 2005). This mode allows the outer boundary conditions of the radiation transport equation to include the incoming intensities from a primary star. The primary spectrum is a full stellar spectrum, not a simple black body. The most important lines, namely H, He, C, N, and O, are treated with full non-local thermodynamic equilibrium (NLTE) during the calculations. Other species, e.g. Fe and Mg, were reset to LTE to save computation time once we tested their influence on the model. The model considers the distance between both stellar components, their radii, and the angle between incident flux and surface normal. The parameters were fixed to the set of PB93/BPH94. We use our spherical symmetric radiation transport (SSRT) mode for the secondary, which's atmosphere is divided into 64 concentric shells and τ_{std} is set to 5000 Å.

To obtain the spectrum of the secondary two simulations are independently carried out: the irradiated day-side; and the night-side, which resembles a MS star. The day-side is assumed to re-radiate all the incident flux, so we use a geometric scaling factor of 0.5. The lateral energy transport between the day- and night-side of the secondary is assumed to be negligible. The irradiation heats and expands the photosphere of the day-side, so we assume in our model that thermodynamic variables like entropy and gas pressure are discontinuous at the boundary between day-side and night-side for a given stellar radius. Consequently, small scale turbulence will develop in a boundary layer, which is not included in our model.

5.4.2   Setup

For all currently derived radii and distances between the components the secondary still underfills its Roche lobe by about 30% (see e.g. Eggleton 1983; Pringle and Wade 1985), i.e., there is no mass transfer to the primary. The secondary should hence be reasonably well approximated by a sphere, which justifies the use of our SSRT mode.

The primary most likely lost a large fraction of its H and He envelope during its CEE, while the secondary accreted additional material during that state. Since hotter post-early-AGB stars tend to be sdOs with a normal H/He ratio (Moehler *et al.* 1998) we use the solar standard composition for the initial condition.

The metallicity Z of both components is based on the solar photospheric abundances by Asplund *et al.* (2005). Further variations will be dealt with during the model fit (Sect. 5.5.1 and 5.5.2).

The temperature of sdOs ranges from $T_{\mathrm{eff,\,p}} = 40\,000$ to $100\,000$ K and the surface gravity from $\log g_{\mathrm{p}} = 4.5$ to 6.5 (Dreizler and Murdin 2000). Since UU Sge seems to be a rather young sdO it should tend to higher $T_{\mathrm{eff,\,p}}$ and lower $\log g_{\mathrm{p}}$, i.e., it has neither cooled nor contracted much yet. For the companion it is reasonable to assume an ordinary MS star with $T_{\mathrm{eff,\,s}} = 3400$ K and $\log g_{\mathrm{s}} = 4.5$, where the last value results from the inferred mass and radius of the secondary by BPH94. However, it is heated to higher temperatures on the day-side, where a horizontal heat flux towards the night-side probably also effectively doubles the temperature (BPH94 measure temperatures of the order 6000 K on the night-side). We take these values as an initial guess.

Fundamental parameters of the primary were explored by calculating a grid of effective temperatures ($T_{\mathrm{eff,\,p}}$), surface gravities ($\log g_{\mathrm{p}}$), and metallicities ($Z_{\mathrm{p}} = \log[H/M]$). The fitting was then done by comparing five selected strong features to the observation close to the primary eclipse. We identified residuals and adapted the parameters accordingly, to improve the fit iteratively.

The secondary is assumed to be an ordinary MS star and is then irradiated by primary spectra of different temperatures. The influence of varying T_{eff} of both components and abundances is investigated.

We do not include a wind or chromosphere in the model calculations.

5.5   Results

5.5.1   The primary

We fit the primary model to the observation at $\varphi \approx 0.0$, i.e., close to primary eclipse, where the flux of the secondary's night-side is negligible and virtually all flux originates from the primary.

The lines are rotationally broadened. Velocities were first calculated assuming a tidally locked and circular orbit, simply with $2\pi r_{\mathrm{p}}/P = 36.9$ km s^{-1} for the primary, which, however, requires a $v \sin i = 160 \pm 20$ km s^{-1} depending on the major feature probed. This value is high but still well below the breakup velocity of $v = \sqrt{\frac{GM}{r}} \approx 600$ km s^{-1}.

For the primary this comparison shows that the N v absorption features agree well with the observations for $\log g_{\mathrm{p}} = 5.0 - 5.5$ and $T_{\mathrm{eff,\,p}} = 70\,000 - 75\,000$ K. This is right between the limb darkening solution (57 000 K) and the limb brightening solution (87 000 K) of BPH94. Grid points with higher $T_{\mathrm{eff,\,p}}$, closer to the light curve analysis of Pustynski and Pustylnik

(2005) and compatible with PB93, require an increase of the N abundance ϵ_N by $+1.5$ dex and more. N is normally increased by less than one order of magnitude in AGB evolution (van Winckel 2003). Also emission of C IV from the secondary's day-side suggests that the primary is not much hotter than $85\,000$ K or further away from the secondary than the assumed 2.46 R$_\odot$ separation (see Sect 5.5.2). Note, that our model of the secondary's day-side represents the spectrum of the substellar point only and the constraint on the primary temperature could be less severe if the secondary's day-side is a 'patchwork' of different temperature.

Table 5.2: Primary abundances with respect to solar values*.

	H	He	C	N	O	Si $_{(LTE)}$
Figure 5.2	12.00	10.53	8.19	8.98	8.56	7.81
75 000 K	(fix)	-0.4	-0.2	$+1.2$	-0.1	$\leq +0.3$
Figure 5.3	12.00	10.73	8.19	9.28	8.56	7.81
85 000 K	(fix)	-0.2	-0.2	$+1.5$	-0.1	$\leq +0.3$
Figure 5.4	12.00	10.43	8.19	9.38	8.56	7.81
85 000 K**	(fix)	-0.5	-0.2	$+1.6$	-0.1	$\leq +0.3$

* based on Asplund *et al.* (2005)

** reduced $\log g_p = 4.5$ to match He II $\lambda 4686$

The intensities of the N V $\lambda 4603, 4619$ Å absorption lines in comparison to the C IV $\lambda 4441$ Å and the O IV $\lambda 4631$ Å lines suggest that N is overabundant and C and O are underabundant in the atmosphere of the primary. Si is only a minor species and not handled in NLTE. Our best-fit abundances for a model with $T_{\mathrm{eff, p}} = 75\,000$ K are listed in Table 5.2.

The general abundance pattern is best described by $Z_p = +0.5$, however, our model only derives the ratios of these elemental abundances, so selecting a specific Z_p is somewhat arbitrary. For all our models the N abundance is enormous, while C and O seem to be slightly depleted. Si only requires depletion for a base metallicity of $+0.5$ dex.

Figure 5.2 shows a comparison between the best fit primary synthetic spectrum with $T_{\mathrm{eff, p}} = 75\,000$, $\log g_p = 5.0$ and abundances from Table 5.2, and the observation close to phase $\varphi = 0.0$. The night-side spectrum of the secondary was not calculated at this point and hence not added to the synthetic spectrum of the primary. Displayed are solely the features of the primary.

Figure 5.3 also shows a comparison between observation and synthetic spectrum, but for a model with $T_{\mathrm{eff, p}} = 85\,000$, $\log g_p = 5.4$ and the abundances of Table 5.2. The quality of the fit is similar to the previous model but requires a higher ϵ_N and produces stronger unobserved N lines.

The He II absorption feature at 4686 Å is systematically too strong in our synthetic spectra. This feature is characteristic for most sdOs. In our model it depends only weakly on the He abundance or temperature. Contrary to the other He lines it increases in depth for higher $\log g$ values. It is also not blended with other lines.

Using the mass and radius from PB93 $\log g_p$ of the primary is constrained to 5.2. However, the $\lambda 4686$ He line fits the observation best for $\log g_p = 4.5$, as can be seen in Fig. 5.4. This fit also requires a He depletion of -0.5 dex to match the other two He lines. All important
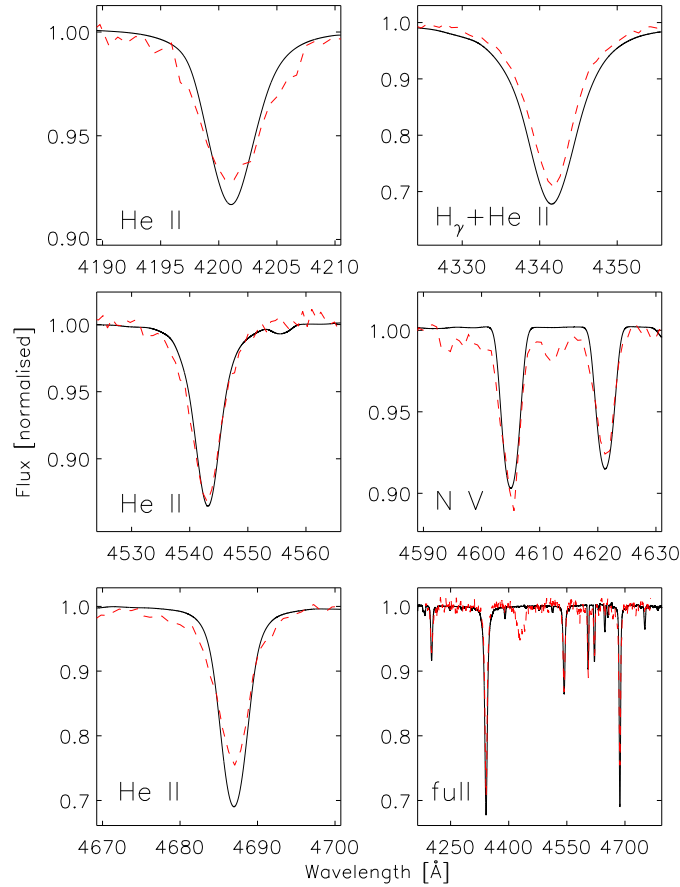
Figure 5.2: A synthetic spectrum for the primary with $T_{\mathrm{eff,\,p}} = 75\,000$, $\log g_{\mathrm{p}} = 5.0$ and abundances from Table 5.2. The first five figures show particular absorption features and the sixth displays the full observed range for an overview. Displayed are observation at $\varphi \sim 0.0$ (red dashed) and synthetic spectrum (black solid).

He II absorption features of the primary within the observed spectral range are dealt with using special Stark line profiles (Hubeny and Lanz 2000), so the effect of $\log g$ should be real, suggesting a much lower $\log g_{\mathrm{p}}$ than given by PB93. Note, that adding the day-side spectrum of the secondary contributes some emission that reduces the problem, while the night-side spectrum influence can be neglected as expected.

In Fig. 5.5 the variation of the absorption line depth with $T_{\mathrm{eff,\,p}}$ is shown. In order to match the observed line depth, the N abundance had to be increased greatly with increasing $T_{\mathrm{eff,\,p}}$. This allows us to constrain the allowed temperature range to values of $70\,000$–$85\,000$ K: the N V (3s-3p) doublet starts to go into emission for higher $T_{\mathrm{eff,\,p}}$. The other two features not displayed in Fig. 5.5, H$_\gamma$+He II $\lambda 4338$ and He II $\lambda 4686$), depend only weakly on temperature. The $\lambda 4338$ absorption decreases slightly with increasing temperature. All He lines, except for $\lambda 4686$, are weakened by increasing $\log g$.

If the primary parameter ranges are fixed, we can get a rough approximation for the equilibrium temperature due to irradiation $T_{\mathrm{eq,\,s}}$ on the secondary's day-side by simple physical considerations (Exter *et al.* 2005), i.e., what temperature of a non-irradiated model repro-
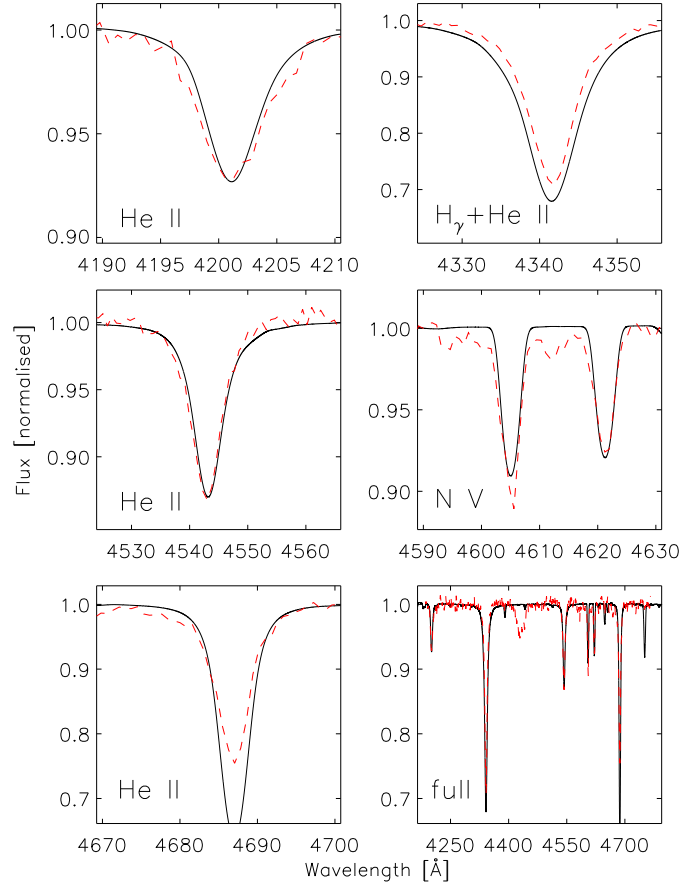
Figure 5.3: As Fig. 5.2, but for $T_{\mathrm{eff,\,p}} = 85\,000$, $\log g_{\mathrm{p}} = 5.4$ and abundance deviations from Table 5.2.

duces the increased luminosity:

$$T_{\mathrm{eq,\,s}} = T_{\mathrm{eff,\,p}}\sqrt{\frac{r_{\mathrm{p}}}{(R - r_{\mathrm{s}})}} \approx 30\,000 \text{ K} \tag{5.1}$$

where we used $T_{\mathrm{eff,\,p}} = 75\,000$ K and the derived geometry of Table 5.1. This is valid if the irradiation influence (extrinsic luminosity) dominates the energy flux from the core (intrinsic luminosity) and the energy is reprocessed, i.e. absorbed and re-emitted. In reality some of the incoming irradiation will be reflected directly and not reprocessed, so lower values for $T_{\mathrm{eq,\,s}}$ are possible.

5.5.2 The secondary

We fit the day-side of the secondary component to the difference spectrum of phase $\varphi \approx 0.5$ minus $\varphi \approx 0.0$, i.e., subtract the primary's influence on the total spectrum. Since there are not many emission lines left, we test the overall influence and then focus on the 'broad emission feature' at 4635–4655 Å. This feature is uniquely sensitive to the abundances used. All absorption lines are Doppler-shifted in anti-phase with the emission features, which shows that the first originate from the primary while the others are due to irradiation on
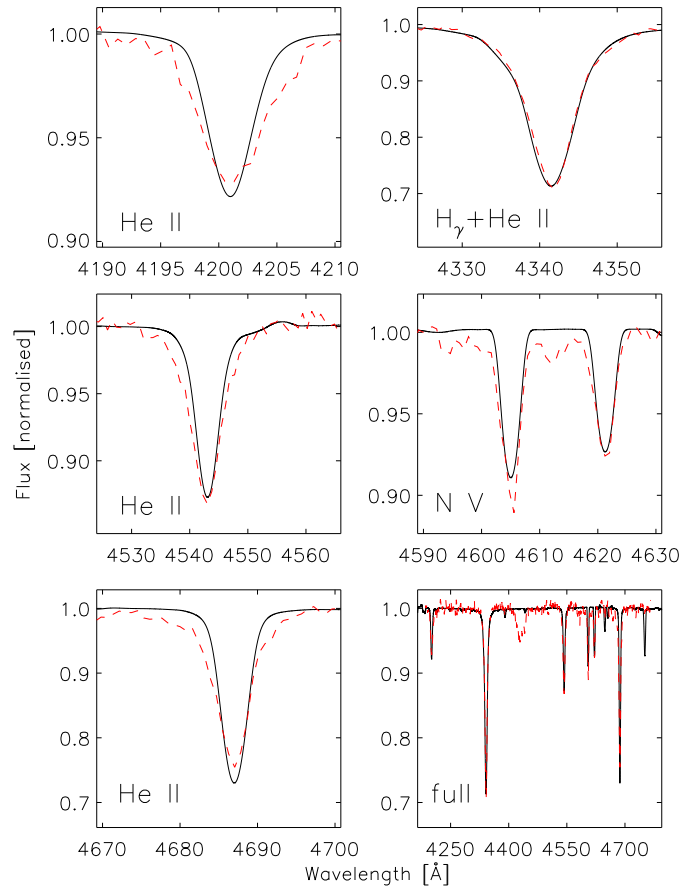
Figure 5.4: As Fig. 5.2, but for $T_{\mathrm{eff,\,p}} = 85\,000$, $\log g_{\mathrm{p}} = 4.5$ and abundance deviations from Table 5.2.
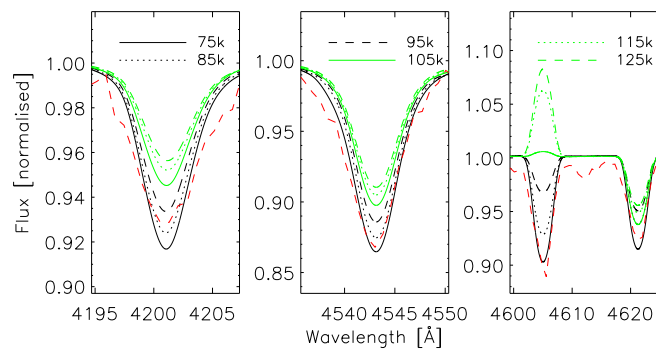

Figure 5.5: Variation in lines due to increase of $T_{\mathrm{eff,\,p}}$. All other parameters are fixed to best-fit values of Fig. 5.2. The observation is also shown (red dashed).

the hot side of the secondary. This is confirmed by the phase dependence of the emission lines, which are strongest at phases close to 0.5 and not visible at all near phase 0.0.

In Fig. 5.6 the combined best-fit primary and initial secondary spectrum is shown. The
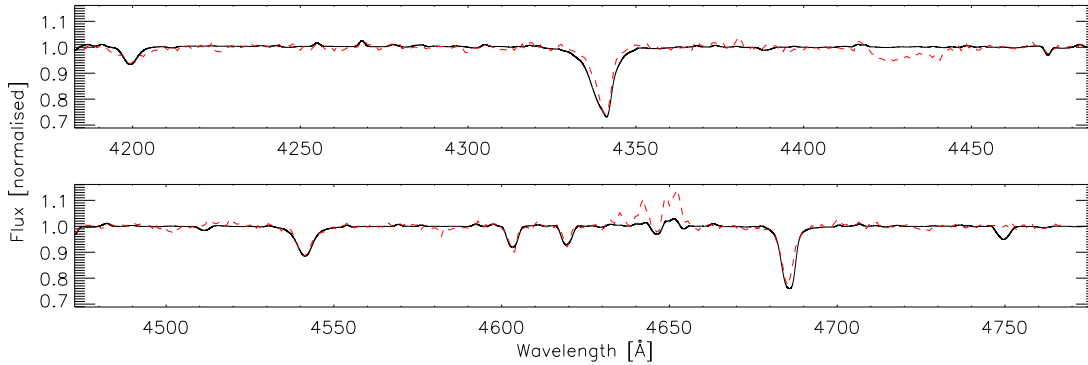
Figure 5.6: Combined theoretical spectrum of the best-fit primary and the initial secondary day-side model, using the primary model ($85\,000$ K, increased abundance from Table 5.2 by another $\epsilon_N = +0.4$ dex and $\epsilon_{He} = +0.1$ dex) to irradiate a $T_{\mathrm{eff,\,s}} = 3400$ K, $\log g_s = 4.5$, $Z_s = 0$ secondary, where C, N, and O are handled in LTE only. The synthetic spectrum (black solid) vs. observation (red dashed). N V absorption at 4600 Å is weakened by N II and C II emission originating from the secondary. The broad emission feature at 4635-4655 Å is not reproduced well by solar abundance in the secondary model.

observed extra emission 'filling-in' the wings of Hγ is too weak (top panel) to explain the differences seen in the bottom panel of Fig. 5.1. There are other small emission lines in the synthetic spectrum which cannot be found in the observation. In the bottom panel of Fig. 5.6 the broad emission feature at $4635 - 4655$ Å is not reproduced well, since important C III and N III lines are too weak (see Fig. 5.7 for details). Also emissions lines such as N II $\lambda 4602.8$, $\lambda 4603.0$, $\lambda 4603.8$, O II $\lambda 4603.3$, and C II $\lambda 4619.9$, $\lambda 4620.5$ start to weaken the primary N V absorptions significantly more than observed.

These all indicate that the heating effect on the secondary is higher than first estimated and that the abundances of C, N, and probably O need to be increased. We used $Z = +0.5$ dex and varied $T_{\mathrm{eff,\,p}}$ to match the broad emission feature.

Figure 5.7 shows a magnification of the wavelength range $4635 - 4655$ Å of a combined primary plus secondary spectrum (weighted for sizes) and the process of applying broadening mechanisms. The broadening is clearly dominated by rotation. Velocities were again calculated assuming a tidally locked and circular orbit with $2\pi r_s/P = 58.6$ km s^{-1} for the secondary. The synthetic spectra match the observation quite well, so no additional rotational broadening is required.

To explain the emission lines of C III at $\lambda 4649$ and 4651 to 4653 Å the C abundance in the secondary needs to be set to $\epsilon_C = +1.5$ dex solar in NLTE and even more in LTE. This seems unreasonable considering that the primary is C depleted during the CEE phase. It is also not compatible with observations outside the 4635–4655 Å broad emission feature, where synthetic spectra with C abundances that high predict unobserved emission lines.

The N abundance is not high enough to reproduce the size of the middle broad emission feature; this indicates that a higher $T_{\mathrm{eff,\,p}}$ is needed and that some N was accreted during the CEE, enriching the secondary's surface by approximately $+1$ dex. This is reasonable, since, in contrast to C, the primary is greatly enriched in N in its photosphere.

The abundance of O on the secondary is difficult to constrain, since the only emission line
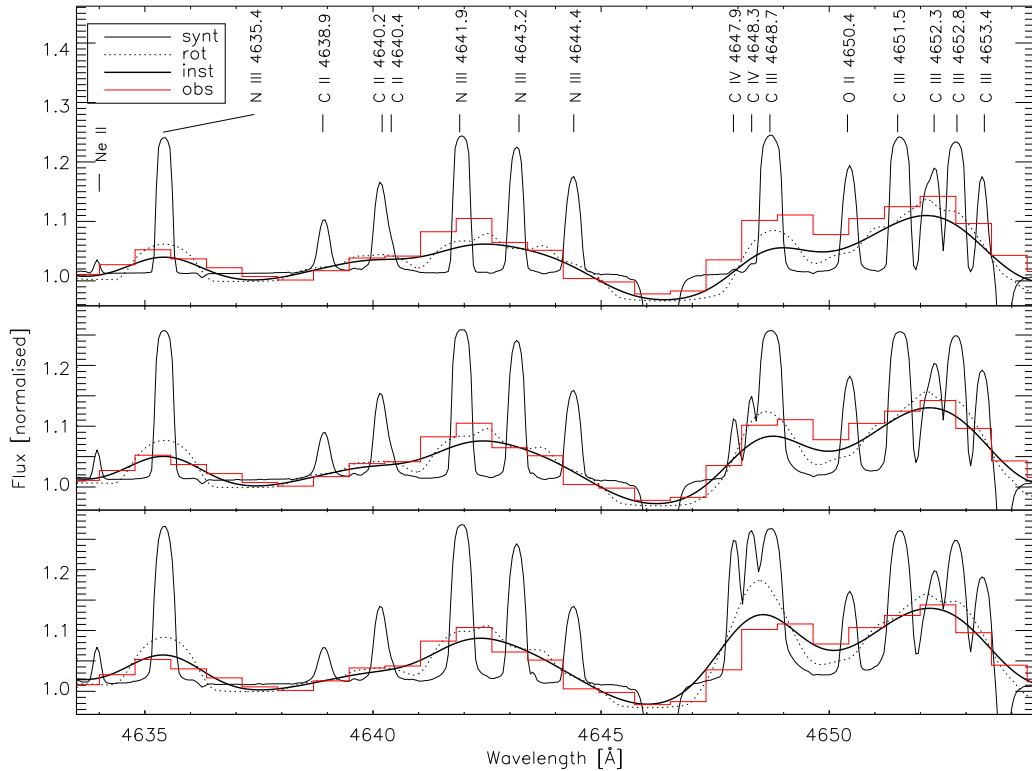
Figure 5.7: Combined theoretical best-fit primary (for each $T_{\mathrm{eff,p}}$) and $Z = +0.5$ dex plus C N O -increased secondary spectrum, weighted for the sizes of the components. The sharp emission features are from the pure synthetic spectrum (solid), to which first rotational (dotted) and then instrumental broadening (thick) is applied. The red histogram is the observation. The primary's effective temperature used for irradiation is $75\,000$ K (top), $85\,000$ K (middle) and $95\,000$ K (bottom), all other parameters of the secondary such as abundances are fixed, though these are increased by more than one order of magnitude relative to solar values in C and N . O is also increased by one order of magnitude to solar, though there is only the O II $\lambda 4650.4$ Å between stronger C lines to match to the observation. An asymmetry arises due to C IV $\lambda 4647.9 + 4648.3$ Å emission for temperatures above $85\,000$ K on the left side of the third broad emission feature, suggesting less heating or larger separation between the primary and secondary to match the energy transport of the other models.

is between stronger C lines (see Fig. 5.7). We use $+1$ dex for the models shown. From evolutionary considerations it need not be enriched.

The instrumental resolution is not high enough to resolve single lines from the broad emission feature originating from the secondary in Fig. 5.7. It might be feasible, however, to analyse the shape if one knows what lines are expected within the broad feature. In case of the double peak in the third broad emission feature, it seems that C IV fits the observation of the secondary's induced emission best for a $85\,000$ K primary, while for the $75\,000$ K and $95\,000$ K model the shape is off-balance on the left. The last model hence suggests less heating or a larger separation. In contrast, there are N II and C II emission lines from the

secondary day-side at the same wavelength as the N V absorption ($\lambda 4603 + 4619$ Å) by the primary that add up to a worse overall fit. Increased heating results in more N III and C III, but the higher continuum changes the shape and hence does not reduce this problem. Combining these two considerations results in a $T_{\mathrm{eff,\,p}}$ value of $80\,000 - 85\,000$ K, comparable to the light curve analysis of Pustynski and Pustylnik (2005) and the revised value of BPH94.

Table 5.3: $T_{\mathrm{eff,\,p}}$ and model predicted $T_{eq,\,s}$.

$T_{\mathrm{eff,\,p}}$	$T_{\mathrm{eq,\,s}}$
75 000 K	23 100 K
85 000 K	26 300 K
95 000 K	29 500 K
105 000 K	32 600 K
115 000 K	35 800 K
125 000 K	39 100 K

using $R = 2.46$ R$_\odot$ and $T_{\mathrm{eff,\,p}} = 3400$ K

Table 5.3 lists the model prediction for $T_{\mathrm{eq,\,s}}$ on the day-side of the secondary depending on $T_{\mathrm{eff,\,p}}$ for a separation of 2.46 R$_\odot$ and $T_{\mathrm{eff,\,s}} = 3400$ K. Results vary in the order of $50 - 100$ K for 1 dex abundance changes.

The typical temperature of the medium where the observed emission lines of heavy elements are formed is 21 000–26 000 K. PB93 gives $25\,300 \pm 1000$ K for the heated day-side of the secondary of UU Sge, which would be consistent with a primary temperature of 78 000–85 000 K in our case and supports our own $T_{\mathrm{eff,\,p}}$ considerations above.

In this case the irradiation of the primary dominates the atmosphere of the secondary completely deeper than optical depth, $\tau = 1$. The variation in $T_{\mathrm{eq,\,s}}$ for changing $T_{\mathrm{eff,\,s}}$, while $T_{\mathrm{eff,\,p}} = 85\,000$ K and $R = 2.46$ R$_\odot$ are kept constant, is negligible. Comparing $T_{\mathrm{eq,\,s}}$ for a model with $T_{\mathrm{eff,\,s}} = 3400$ K and one with $T_{\mathrm{eff,\,s}} = 6000$ K results in a mere change of $20 - 30$ K.

An interesting effect that was already observed by Brett and Smith (1993) in irradiated models (10 000 K blackbody primary) is that the optical depth at a given geometrical depth increases with increasing irradiative flux, i.e., the radiation makes the surface layers more opaque. We see a similar effect for primary temperatures up to roughly 85 000 K, at even higher temperatures the opposite occurs and the surface layers of the secondary start to become less opaque again, because some species become fully ionised.

The high difference between primary and secondary night-side flux contribution to the observed spectrum that allows the decoupling of the primary from the secondary parameters in the first step of this analysis prevents a proper $T_{\mathrm{eff,\,s}}$ estimate for the night-side of the secondary being made. At phase $\varphi \sim 0.0$ the spectrum is dominated by the primary and night-side of the secondary can not be fitted. The heat flux beyond the terminator in convective layers should adjust to a static solution if it is supposed to be the same star. An attempt to match the structure, i.e., the entropy per free particle, of the irradiated model day-side with hotter models of the undisturbed night-side was unsuccessful. The radiation field of the primary dominates the temperature structure of the day-side of the secondary deep into the photosphere, the convection zone is therefore pressed down into deeper layers and no common adiabat was found.
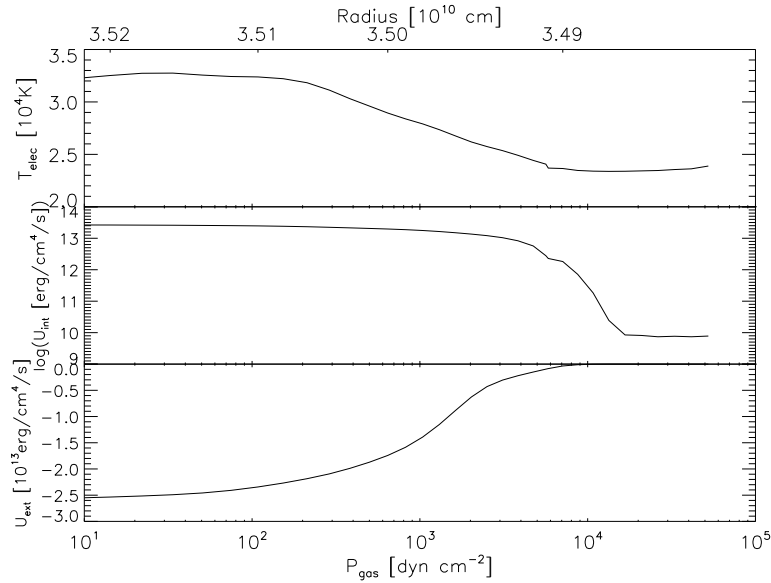
Figure 5.8: The structure of the temperature and radiation field in the irradiated atmosphere at the substellar point. The small kink at $P_{\text{gas}} = 5 \cdot 10^3$ dyn cm^{-2} is due to numerics. The upper panel shows electron temperature T_{elec}, the middle panel the logarithm of the internal radiation flux $u_{\text{H,int}}$, and the lower panel the external radiation flux $u_{\text{H,ext}}$. See text for details of the definition of the fluxes.

Figure 5.8 shows the structure of a secondary atmosphere, irradiated by the best-fit $T_{\text{eff,p}} = 85\,000$ K primary. The temperature rises to just below $34\,000$ K at 30 dyn cm^{-2} and drops again by about a third to deeper layers. Our model is calculated down to $5 \cdot 10^4$ dyn cm^{-2}. The lower panels of that figure characterise the radiation field: The middle panel shows the internal radiation flux $u_{\text{H,int}}$. This is calculated as the radiation flux that would originate in an atmosphere with the temperature structure from the upper panel without any external radiation. At the inner boundary $u_{\text{H,int}}$ is fixed, matching the blackbody radiation for the intrinsic, i.e., undisturbed, temperature of the secondary.

For each layer radiation is generated going in- and outwards. The radiation going inwards is reflected at the inner boundary condition and thus cancels out in the derivation of $u_{\text{H,int}}$, whereas the radiation going outwards is summed up and therefore $u_{\text{H,int}}$ increases monotonically outwards by more than three orders of magnitude. The energy lost exceeds the energy delivered from the inner boundary by far and the photosphere would cool down without an external energy source.

The lower panel in Fig. 5.8 shows the external radiation flux $u_{\text{H,ext}}$. To obtain a measure of the influence of the external radiation field a full model including the internal flux and the irradiation is calculated. The difference between the radiation field obtained in this case and the internal radiation flux ($u_{\text{H,int}}$) is $u_{\text{H,ext}}$. This characterises the layers where the incident radiation is *reprocessed* in the atmosphere. $u_{\text{H,ext}}$ is negative, because it is directed inwards. It does not contain *reflected* external irradiation, since this cancels out in the net flux $u_{\text{H,ext}}$. In the thin outer layers of the atmosphere the optical depth is low, so only little flux is absorbed. Around a gas pressure of 10^3 dyn cm^{-2}, much of the external flux is absorbed,

causing a temperature inversion, so deeper layers are cooler again. Between 10^3 dyn cm^{-2} and $2 \cdot 10^3$ dyn cm^{-2} the external radiation flux deceases to $1/e$ of the initial value, thus this can be taken as the depth to where the external radiation penetrates.

The ionisation in the outer layers is not collisionally dominated but the ionisation structure is given by the external radiation field, leading to an 'over-ionisation'. Figure 5.9 shows the dominant stages of ionisation for the ions of C, N, and O. Although the temperature is only 25 000 K at 10^{-2} dyn cm^{-2}, higher stages of ionisation (C IV, N III and O III) prevail compared to the inner, denser layers at the same temperature, but the column mass of these elements is so small that they do not contribute any significant emission lines. Most of the
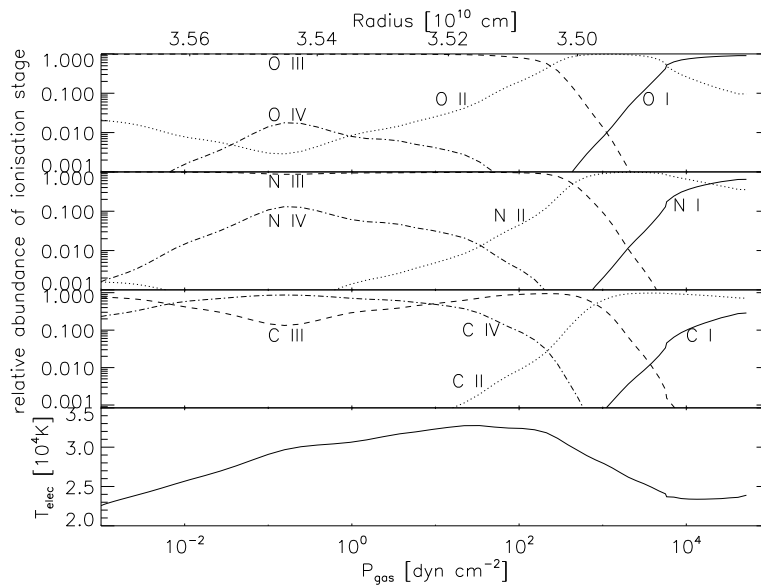

Figure 5.9: The relative abundances of the most prominent ionisation stages for C, N and O. For comparison purposes the lower panel contains the temperature structure.

spectral features above originate around 10^3 dyn cm^{-2}, where most of the incident energy is reprocessed. In this region C II and C III, N II, N III, and O II are most dominant. At deeper layers these ions recombine to neutral atoms, but the density and therefore the optical depth also increases, so that no line emission from atoms is observed. If the primary is either closer or hotter than expected than the stronger irradiation would lead to higher stages of ionisation in the crucial region around 10^3 dyn cm^{-2} and cause more emission lines which are not observed, e.g. O VI.

5.6 Discussion

In our model the secondary is tidally locked in a circular orbit, hence is rotating synchronously, because its calculated $v \sin i$ fits the observation and primary and secondary eclipses are equidistant in the light curve of PB93. The primary cannot be tidally locked, since additional broadening requires a speed-up by a factor of approximately $4 - 5$, which is still a reasonable rotational velocity for a subdwarf with radiative envelope that was spun up by its own contraction. We assume a circular orbit for simplicity, even though it is worth

noting that within the framework of Zahn's theory, the synchronisation timescales are several orders of magnitude smaller than the circularisation timescales (Toledano *et al.* 2007). This ensures a uniform irradiation at a constant distance on the same side of the secondary, which itself is convective at least in layers the irradiation cannot penetrate. Also worth noting is that Zahn (1977, 1989) found the characteristic timescale for synchronisation as a function of a, the major semi-axis of the orbit, to be $\tau_{sync} \sim a^6$ for stars with convective envelopes and $\tau_{sync} \sim a^{8.5}$ for stars with with radiative envelopes, which might explain why the smaller, more compact and still contracting primary has not yet reacted to synchronisation.

5.6.1   Primary component

Without any limb darkening or brightening effects included $T_{\mathrm{eff,\,p}} = 75\,000$ K is in between the results of PB93/BPH94 for the primary. It is in agreement with their error bars, given a fixed separation of 2.46 $R_{\odot}$. We, however, favor a higher value of $80\,000$–$85\,000$ K, due to the effects on the broad emission feature on the secondary (see Fig. 5.7), even though this requires an enrichment of approximately $+1.5$ dex in N on the primary surface. This is a similar result to the light-curve solution by Pustynski and Pustylnik (2005).

In general, He rich sdO stars are also enriched in some metals, especially C and N. This clearly indicates that the surface contains material burned in the C N O cycle as well as products of helium burning (Dreizler and Murdin 2000). Within these nuclear burning processes C is turned into N by proton capture, probably benefited by some effect that mixes protons into deeper layers. Thus the abundance of C falls while the abundance of N increases (^{12}C (p,γ)^{13}N (e$^+$,ν)^{13}C (p,γ)^{14}N). He is turned into C via the triple alpha (3α) reaction, but C is destroyed in the outer parts of He -burning shells by the reaction ^{12}C (α,γ)^{16}O. Hence C is depleted more than N is enriched. The sdO of UU Sge is decreased in He and especially enriched in N and depleted in C and O. This can be understood as stripping the outer envelope layers down to a layer which was enriched in N during the CEE; the H -rich and He -rich layers, where the 3α process which produces C is most efficient, have been removed.

The production of ^{14}N at the cost of C and O in the C N O cycle (de Greve and Cugier 1989) is not unusual in the evolution of AGB stars during their third dredge up phase (see Herwig (2005) for a review). Enriched N and depleted C is also observed in WD+MS binaries as supernovae (SN) Ia progenitors (Langer *et al.* 2000). The depletion of He is most likely due to the CEE, i.e., the stripping of the outer layers.

Note that He is slightly underabundant in UU Sge for all our models. If a high $T_{\mathrm{eff,\,p}}$ is prescribed for the model then the He abundance is fitted closer to solar values.

N v $\lambda 4605$ is in emission for NLTE models with $T_{\mathrm{eff,\,p}} \geq 110\,000$ K. There are no known sdOs with such high temperatures (S. Dreizler, private communication). There is, however, PG1144+005 ($T_{\mathrm{eff}} = 150\,000$ K and $\log g = 6.5$), which is a peculiar PG1159-like star that shows such N v emission lines at $\lambda 4603$ and 4619 Å (Werner and Heber 1991). Therefore this NLTE effect seems reasonable and suggests a lower $T_{\mathrm{eff,\,p}}$ than $100\,000$ K, probably even lower than $90\,000$–$95\,000$ K; therefore our model is contradicting the primary temperature of $120\,000$ K found by Shimansky *et al.* (2008).

There is a problem with the surface gravity derived from He II $\lambda 4686$ Å which suggests a $\log g_{\mathrm{p}} \approx 4.5$, and we require a He depletion of -0.5 dex to fit all other He II absorption lines. Using the mass and radius from PB93 $\log g_{\mathrm{p}}$ of the primary is constrained to 5.2 ± 0.2 as mentioned before. Probably this is due to numerically instabilities in the treatment of the

radiation pressure in the model, since it seems unlikely that the primary is much less massive or has a veil of reaccreted He within its Roche lobe that has not fallen back on the surface yet. At phase 0.5 this problem is solved by adding emissions from the day-side of the secondary and consistent with a $\log g_{\mathrm{p}} = 5.0$ to 5.2. However, at phase 0.0 the night-side, even if set to $T_{\mathrm{eff,s}} = 6000$ K (e.g. as would be due to a horizontal heat flux beyond the terminator), is too weak for the same correction. It is unclear whether the primary is really less compact than expected, or why otherwise this particular He II feature is weaker than expected, since there is no indication of any emission (e.g. by material within the secondary Roche lobe through which radiation is transmitted).

While main sequence O stars are known to exhibit a stellar wind, the atmospheres of most sdO stars can be regarded as hydrostatic. Of course, signatures of a stellar wind can be detected in the most luminous sdOs through P-Cygni profiles in UV resonance lines or through emission lines in the visible, but even in these stars all other lines orginate from quasi-static layers of the atmosphere (Dreizler and Murdin 2000).

We do not include limb darkening in our models, since PB93 find no limb darkening for primary temperatures in excess of $85\,000$ K, analysing the light curve around the ingress and egress from the primary minimum.

5.6.2 Secondary component

Webbink (1988) claimed, inferred from observations of the binary core of planetary nebulae, that the unevolved secondary star has been little disturbed by the CEE and resembles a normal main-sequence star. The night-side temperature of the secondary component, measured by BPH94, however, would normally indicate a spectral type of late A / early F and consequently a mass around ~ 1.6 M$_\odot$ and a radius around ~ 1.5 R$_\odot$, assuming it is on the main sequence. Hence the derived mass of 0.29 M$_\odot$ and radius of 0.53 R$_\odot$ imply that the evolutionary path of this object has been greatly influenced by the sdO star. This mass estimate indicates an M-type dwarf.

It is conceivable that this star has been stripped of its outer layers during the CEE and accreted some other material.

Due to the amount of material accreted and the short time since the CEE phase, the secondary may still be out of thermal equilibrium. The thermal relaxation time-scale of the disturbed outer layers of the secondary, once the common envelope is ejected, is $\sim 10^4$ years, comparable to the estimated age of the PN. This could explain why the secondary is oversized for its mass (PB93) and could mean that the internal structure of the secondary is inhomogeneous, i.e., the accreted material has not mixed in (Prialnik and Livio 1985; Sarna and Ziolkowski 1988). Probably the heating on the day-side of the secondary also contributes to the inflation of the star.

Since the mass ratio $q < 1.0$, i.e. the secondary is less massive than the primary, the system has been detached after the CEE and will be, until gravitational wave radiation and magnetic stellar wind braking brings the secondary in contact with its Roche lobe again (Sarna *et al.* 1996). The secondary may resemble the composition of the primary.

According to Marks and Sarna (1998) the effect of accretion during CEE on the abundances is expected to be very small, the only significant difference being seen in the abundance of N, which is increased by less than one order of magnitude. The secondary of UU Sge, however, displays an enrichment of not only N but also C and probably O in its photosphere compared to $Z_{\mathrm{s}} = +0.5$. It is oversized compared to a zero-age MS star of the same mass

(BPH94). This might be understood as a layer of material accreted from the primary, possibly related to the last layer stripped there. Probably C and N were transferred to the secondary while C was still being transformed to N in the primary. Accreted material may still settle down to deeper layers in the secondary but not yet be mixed in, hence producing an unusual abundance in the currently visible spectrum.

In their calculations of the common envelope phase, Hjellming and Taam (1991) found that the secondary accretes approximately 0.1 $M_\odot$ of red giant envelope material before it expands to fill its Roche lobe. However this estimate is based on calculations by Taam and Bodenheimer (1989) and highly dependent on the assumed efficiency of envelope ejection. Marks and Sarna (1998) point out that once it has filled its Roche lobe, it loses most of the material accreted before the envelope is ejected such that the net gain in mass is approximately $0.01 - 0.06$ $M_\odot$. It is not clear which part of the envelope is predominantly accreted.

PB93 already noticed this similarity in spectra between UU Sge and V477 Lyr and absorption lines from the Balmer series, He II and N V ions while He I lines are absent. They point out that the strength of He II lines suggests that the Balmer lines are contaminated by other members of the He II series, i.e., Hβ + He II $\lambda4859$, Hγ + He II $\lambda4338$ and Hδ + He II $\lambda4098$ Å. However, our observations only contain Hγ.

The strong broad emission feature at 4635–4655 Å seems to be common to sdO+MS pre-CVs and is also the strongest emission between 3950 and 5100 Å. It is remarkably similar in shape to the V477 Lyr observation by Shimansky *et al.* (2008). This confirms the similarity of these two systems, as already pointed out by Ritter (1986) and PB93. There are, however, more smaller emission features visible which indicate that the secondary in V477 Lyr has greater influence on the total spectrum than the one in UU Sge. The broad feature is produced by very strong C and N emission lines in the secondary, as discussed in Sect. 5.5.2, while the rest of the spectrum is better fit by lower C and N abundances.

Emissions lines from a chromosphere are unlikely on the day-side due to the strong external radiation field. Also the contribution from a chromosphere on the night-side, if existent, is not likely to explain the missing emission for He II $\lambda4686$ in the combined spectrum (B. Fuhrmeister, private communication).

5.6.3   Evolution of UU Sge

The evolution of UU Sge is still not completely understood. N is overabundant, indicating that the system reached the AGB. There was most likely no crucial interaction between the two stars until the primary envelope expanded to a size that it engulfed the secondary and started CEE.

This might be explained by an enrichment in C, N and probably O that occurred during the CEE and only effects outer layers of the secondary, which might not yet be in thermal equilibrium. Also the secondary might have accreted C from an outer layer (3α process) while the C N O cycle in the primary was still working to convert C into N, explaining why this element is not found enriched on the primary, too.

Another possibility, although unlikely, is that the hot, oversized companion indicates that there were two AGB phases in the system and that the first was suppressed due to a too high mass-loss rate of the secondary. This would be another explanation for enrichment of heavier elements than He on the secondary, especially why there is C present. However, the secondary is too cold and its mass is too low to support this idea, since there is no proper mechanism known and its spectra look too ordinary. The primary could have gone through

an earlier CEE of course, too, losing its envelope in more steps than just one.

The primary was stripped of its H -rich and He -rich layers during the CEE, exposing a shell of N underneath. Both components display lines with peculiar effects: the He II $\lambda 4686$ absorption suggests a layer of He on top of the N on the primary, and a slightly lower $\log g_{\mathrm{p}}$ or some unexplained emission from the secondary; the broad emission feature on the secondary that reacts unique to abundance changes and that is the strongest emission over the entire wavelength range of the observation.

The broad emission feature is visible also in the other irradiated systems, e.g. the secondary of V477 Lyr (Shimansky *et al.* 2008), which is also $2.0 - 2.5$ times larger than the radius of a zero-age MS star with comparable mass (BPH94). This suggests a non-unique mechanism due to a similar evolution in both systems.

Table 5.4: Final results (see discussion):

	Primary	Secondary
T_{eff}	80 000 to 85 000 K	(6000 to 7000 K)
T_{eq}	n.a.	24 000 to 26 000 K
$\log g$	(4.5), 5.0 to 5.2	(4.45)
ϵ_{He}	-0.2 to -0.4 dex	n.a.
ϵ_{C}	-0.2 dex	$+1.0$ to $+1.5$ dex
ϵ_{N}	$+1.2$ dex and more	$\approx +1.0$ dex
$L = 4\pi\sigma r^2 T_{\mathrm{eff}}^4$	1 to 2 $\cdot 10^{37}$ erg s^{-1}	1 to 3 $\cdot 10^{33}$ erg s^{-1}
$L = 4\pi\sigma r^2 T_{\mathrm{eq}}^4$	n.a.	2 to 5 $\cdot 10^{35}$ erg s^{-1}

Table 5.4 displays the derived parameters of UU Sge from Sect. 5.6.

5.7   Summary

We modelled both components of UU Sge with our state-of-the-art stellar atmosphere code `PHOENIX`, which treats the radiative transfer in an atmosphere self-consistently in the presence of an external radiation field and uses the newest extensive set of opacities currently available. In this respect our work goes beyond previous work.

Our analysis provides the temperature range of the primary and investigates the heating of the secondary's day-side. We find evidence for a large N enrichment on the primary, a depletion of C and O, and an upper limit for Si that is less than $+0.3$ dex solar. The lower He abundance in the sdO originates most likely from the loss of its envelope.

The observed broad emission blend at 4635–4655 Å in the secondary is stronger than the theoretical result by a factor of 3–5, which is indicative of the strong effects of 'over-ionisation' by external radiation in high atmospheric layers for the C N O elements. This might be due to pollution of material accreted from the primary, which has not yet settled down to lower layers in the oversized secondary and explain C and N enrichment.

It is obvious that both stars have been greatly influenced in their evolution by their companion. The highly enriched metals observed in the primary and secondary could indicate that there is no mixing in the outer layers, since any counter mechanism that removes N into deeper layers would greatly decrease its abundance and stars would not produce such peculiar line strengths.

Convection in the day-side of the secondary is suppressed by the irradiation, the heat flux
is dominated by radiation throughout the entire photosphere. Observationally the night-side
appears to be heated by a horizontal flux, resulting in an earlier spectrum then expected
for the secondary mass. Without a horizontal component of convective motion or radiative
transfer (a 3D model), we cannot model the transfer of heat from layers of the irradiated
half-sphere towards the undisturbed night-side, thus we expect that motion beyond the limits
of our model is responsible for the heating of the secondary night-side.

Further analysis of UV and IR spectra could improve the disentangling of primary and sec-
ondary spectra, since the UV is dominated by the sdO, while the companion main source lies
in IR. An interesting line in PG1144+005 is N v $\lambda 4925$ Å (high l, $6 \rightarrow 7$ transition), which is
a strong emission line and could be of considerably strength in UU Sge, too, hence allowing
to confirm the N enrichment independently to the doublet used here.

Another fit to a secondary night-side only spectrum during primary eclipse could help to test
the M-dwarf thesis, find the horizontal heat flux beyond the terminator and possibly allow to
check for C, N and probably O enhancement on the surface of the secondary without the
effect of irradiation.

Chapter 6

Conclusions & Outlook

This thesis explained the advantage of pre-cataclysmic variables (pre-CVs) for studies of close binaries (CBs) and how the common envelope evolution (CEE) works in a basic approach. It described the tools and modifications to the standard stellar atmosphere code `PHOENIX` necessary to include external radiation.

`PHOENIX` has the ability to match synthetic spectra with observations of irradiated objects. Induced emission lines, e.g. from hydrogen, can be easily fitted. In the case of UU Sagittae (UU Sge), which is an extraordinary total eclipsing pre-CV and therefore a great laboratory, there were upgrades required to improve the overall fit, especially in the helium lines:

- external He data to cover a missing absorption line at 4200 Å,

- explicit He stark-broadening profiles (Hubeny and Lanz 2000) within the wavelength range of the observation and

- a correction to the bound-bound transition routine that caused additional emission with the new external model atoms

There are still a couple of unresolved problems that will not be dealt with in the old `Phoenix 15.04` version anymore, but avoided in `Phoenix 3D` by a different approach. Some quirks during the modeling were, e.g. the instable radiation pressure routine that had to be disabled for the primary and secondary in order to converge, the incompatibility of NLTE and convection in the secondary, which only allowed one routine to be enabled with reasonable results and the correcting adjustments in radius, temperature and pressure for the irradiated star that occasionally produced huge and devastating corrections due to big gradients resulting from a changed incoming primary spectrum.

Testing the irradiation mode we find:

- an influence on the structure and spectra of the secondary by:

  - the irradiation incident angles, which also effects NLTE

  - the effective temperature of the primary and

  - the separation from the primary, which is similar to a change in the primary temperature, but also determines possible incident angles if the radii are fixed

- in particular a suppression of the convection zone in the secondary down to layers below $\tau = 1$ for massive irradiation

- the negligible influence of the effective temperature of the secondary on the equilibrium temperature of the heated hemisphere for such situations of massive irradiation

Even though we are using snap shots of UU Sge near primary and secondary eclipse only we can constrain the effective temperature and surface gravity and find a great enrichment in nitrogen. This enrichment must be due to a N-rich shell that had been exposed during the late CEE.

For the secondary we are able to predict the heated day-side temperature structure, including ionization stages and resolve strong abundance deviations in carbon and nitrogen in a peculiar broad emission feature. This implies that the secondary accreted C and N while the fusion on the primary still converted C to N.

This broad emission feature is also the strongest emission in V477 Lyrae, indicating a non-unique evolution mechanism, even though masses and temperatures are slightly different from UU Sge. Any theoretical CEE model should explain these abundance deviations and take into account that the secondary accretes C, N and probably O during the last stage of the CEE.

Our temperature estimates for UU Sge are within error bars of Pollacco and Bell (1993); Bell et al. (1994), what makes them more trustworthy. We also derive an abundance pattern. Note, however, that our work is much more rigorous and based on a real physical model.

6.1   Future works

To have better statistics on the results more planetary nebula nuclei (PNNi), i.e., binaries containing a young subdwarf of type O or B (sdO/sdB) and a companion with a surrounding planetary nebula (PN) should be investigated for their temperature structure and elemental abundances. Especially V477 Lyrae is of some interest because of its similarity to UU Sge. Some other possible candidates are listed in table B.1.

Since the number of known close binary PNNi is very small and some parameters of the known systems are still uncertain, the sample could be widened to include good observable pre-cataclysmic variables (pre-CVs); these are low-mass systems consisting of a hot degenerate dwarf and a low-mass secondary. Such systems are probably also "post-PNN" binaries. Formally, the PN stage can last about $3 \cdot 10^4$ yrs, when due to expansion the emission measure of the PN has dropped below about 10^2 cm^{-6} pc, even if the exciting source remains hot and luminous. The bright phase of a binary post-PNN can last as much as 100 times longer than the PN stage (Iben and Tutukov 1993). Therefore it is more likely to find star systems in this stage, even though there is no PN to clearly distinguish them. And systems like GD245 (Schmidt et al. 1995) are also suited to test the effects of irradiation.

So far we only had 'snapshots' on single spectra. The 1.5D model method is expected to give a better solution for each calculated point on the surface and a better approximation for points close by if one assumes that there are no jumps in the temperature and pressure structure. Our results do not yet include limb darkening or brightening, though with different incident angles this is indirectly included in the '1.5 D patchwork' method (Wawrzyn et al. 2009b), following a suggestion of Brett and Smith (1993). This could help to explain effects on phase resolved spectra as shown in the right panels of figure 4.4 and whether the asymmetry arises from a combination of line Doppler shifts, varying visible heat zones and emission line strengths.

There are still a few unresolved technical problems. On the one hand the radiation pressure in the model disrupts hot sdOs, on the other hand there is evidence that it would solve (or at least reduce) the fitting problem with the He II $\lambda 4686$ Å absorption feature that is characteristic for sdOs. The current NLTE and convection routines do not function properly with each other, so several setups must be used to investigate different questions, depending on which physical effect is likely to have more impact on the result.

In a more distant future the upcoming PHOENIX-3D (Hauschildt and Baron 2006, 2008; Baron and Hauschildt 2007) will get rid of these quirks due to a different handling of the convection routine, a more stable equation-of-state and for the first time it will also be able to include heat fluxes on the secondary surface beyond the terminator to the night-side directly. Any results achieved now will provide a benchmark and help to verify basic results before the full 3D structure will be explored.

Appendix A

Irradiation common block

These are the input parameters for the PHOENIX dqs-file to define the external radiation field (or irradiation) on the atmosphere to calculate. The 'source' is identically with the primary in the case of a close binary system. The parameters are:

- *lwd*: luminosity of the irradiation source = $4\pi R_{\text{source}}^2 * \sigma * T_{\text{source}}^4$ (should not be in use anywhere anymore, but is instead directly calculated by *twd* and *rsource*)

- *twd*: the 'effective' temperature of the source, i.e., $T_{\text{eff, source}}$ [in K]

- *rsource*: the radius of the source [in cm]

- *max_spectrum_points*: the number of wavelength points in the input '.7'-file that holds the source spectrum (can be looked up with any editor)

- *rdng*: (default is .false.) setting this flag .true. reads 'old style' nextgen spectra (only used for compatibility with older models)

- *r2*: the distance from the primary surface to the secondary surface, at angle $\arccos\theta_{\text{domue}}$ [in cm]

- *d2*: the shortest distance from the primary surface to the secondary surface [in cm] (along symmetry axis, i.e., from the closest point of the primary to the substellar point of secondary)

- *d2center*: (default is .false.) setting this flag .true. changes the meaning of *d2*, which becomes the center-to-center distance between the two objects, rather then the distance from the primary to the substellar point. From this the surface-to-surface distance is calculated and used (ignored for plane parallel mode)

- *domue*: index of the angle through which the irradiation hits the secondary (Note that the real angle is taken from the RTE and that there is a limited numbers of incident rays or 'characteristics', i.e., not every angle, available).

  - for the plane-parallel mode there are only 8 incident rays to choose
  - spherical symmetric models have typically ≥ 63 rays (increases with the number of layers)

By setting *domue* = (some integer) the angle on which the incident radiation is received is selected. *domue* = 0 is for isotropic radiation (all incoming rays selected).

- *angirr*: allows to specify the actually $\cos(\theta)$ angle of irradiation, closest *domue* is taken at the end of each iteration. This is an incident ray, hence it is supposed to be inside the intervall [-1,0]! Closest angle found/used will be printed in .out-file.

- *mkhint*: (default is .false.) .true. calculate internal flux and also prints T_{eq} in .out-file (Note, this requires two calls to accit per iteration!)

- *redist*: the redistribution factor[17]

    - 1.0 : (default) no redistribution: uses FULL input flux!
    - 0.5 : incident energy is absorbed, uniformly, over the 'day-side' only
    - 0.25 : incident energy is absorbed, uniformly, over the whole sphere

At the completion of a PHOENIX model, several irradiation values are given in the output file. Note, that an earlier termination, e.g. due to fulfilled convergence criteria, misses the output block. There is no interpolation included for the equilibrium temperature T_{eq}, so *insert_tau_eq_one=1* must be set to display reasonable values! An output example:

```
-------------------------------------------------
>>> Parameters and Output for Irradiated Model <<<
-------------------------------------------------

 PRIMARY: Teff = 85000.0 K   Radius =  0.23664D+11 cm

 SECONDARY: Tint = 3400.0 K   Radius =  0.37062D+11 cm

orbital separation:  1.71220D+11 cm 1.14452D-02 AU

              redistribution factor:   5.0000D-01

     equilibrium temperature (Teq):   2.2818D+04  K
           height of the atmosphere :  2.15241D+09 cm
```

If additional output for debugging is enabled (e.g. using 'laus=6' in dqs-file), an extra block is written once PHOENIX reaches the part where irradiation is initialized. It looks like this:

```
Irradiation model selected. System parameters are:
 primary luminosity= 3.2600D+37erg/s primary Teff= 95000.0K
 primary's radius:   23664000000.0000
 inconsistency detected:  3.260000000000000E+037
                          3.249629018965272E+037
 no adjustments were made!
 binary separation: 1.7122D+11cm
 incident angle index:    0
 isotropic illumination selected!
 max_spectrum_points=      162692
 spectrum input file:
 irrad_spec.7
```

---

[17]As defined in equation 3.21 at the end of chapter 3.3.1.

Appendix B

Known young pre-CVs

Among the known pre-cataclysmic variables (pre-CVs), the group of young systems containing hot O subdwarfs (sdO) is the smallest. According to the most recent catalog by Ritter and Kolb (2003) and the review by Shimansky *et al.* (2006), eight objects of this type have been reliably classified and another five objects are believed to be likely candidates. At present, most of the young pre-CVs have been studied poorly, although they have unique radiation characteristics. The presence of hot subdwarfs in pairs with late-type stars in these systems gives rise to a strong reflection effect with regular light variations with amplitudes from $0^m\!.5$ to $1^m\!.5$. The spectra of young pre-CVs are rich in emission lines of highly ionized elements, indicating a rise in temperature to $T_{\mathrm{eff}} = 30\,000$ K in irradiated plasma regions. Simultaneous studies suggest that the radii and temperature of the secondary component in young pre-CVs are increased compared to those of main sequence (MS) stars, i.e., they have luminosity excesses. The amplitudes of theses excesses reach $(10 - 80)\,L_{\mathrm{bol}}$ of MS stars with the corresponding masses and cannot be explained by a reflection effect (Shimansky *et al.* 2008).

Table B.1 shows parameters of the known young pre-CVs, where:

- *System*: the name of the binary, 'PN' marks clearly detected planetary nebulae

- T_{p} / T_{s}: effective temperature of the primary respectively secondary

- r_{p} / r_{s}: radius of the primary respectively secondary

- M_{p} / M_{s}: mass of the primary respectively secondary

- R: separation of both components

- i: inclination of the system

- $S.$: source of the parameters

Also see Hillwig *et al.* (2000) for a compilation of probable post-common envelope binaries.

Table B.1: Parameters of the known young pre-CVs. Sources: 1) Ferguson *et al.* (1987); Shimanskii *et al.* (2008a); 2) Exter *et al.* (2005); 3) Pollacco and Bell (1993); Bell *et al.* (1994); 4) Exter *et al.* (2003); 5) Shimanskii *et al.* (2004); 6) Pollacco and Bell (1994); Shimansky *et al.* (2008); 7) Landolt and Drilling (1986); Hilditch *et al.* (1996); 8) Sing *et al.* (2003); 9) Aungwerojwit *et al.* (2007); 10) Haefner *et al.* (2004); 11) Ritter and Kolb (2003); Shimanskii *et al.* (2008b).

System name *visible PN?*	T_p [K] $\pm\sigma$	r_p [R$_\odot$] $\pm\sigma$	M_p [M$_\odot$] $\pm\sigma$	T_s [K] $\pm\sigma$	r_s [R$_\odot$] $\pm\sigma$	M_s [M$_\odot$] $\pm\sigma$	R [R$_\odot$] $\pm\sigma$	i [°] $\pm\sigma$	*S.* #
BE Uma	123 000	0.026	0.59	4750	0.94	0.25	6.890	83°	1
	5000	0.002	0.07	150	0.03	0.08	0.14	1°	
TW Crv	105 000		0.57			0.17	1.87	35°	2
	20 000							6°	
UU Sge PN	87 000	0.33	0.63	7300	0.53	0.29	2.45	87°	3
	12 500	0.01	0.06	300	0.02	0.04	0.09	1°	
VW Pyx	85 000								4
	6000								
V664 Cas PN	83 000	0.19	0.57	5400	1.3	1.09	3.37	28°	5
	6000	0.02	0.03	500	0.08	0.07	0.06	2°	
V477 Lyr PN	83 000	0.192	0.56	6100	0.421	0.19	2.31	82°	6
	5000	0.009	0.10	250	0.021	0.02	0.11	1°	
KV Vel PN	77 000	0.157	0.63	4500	0.402	0.23	2.01	60°	7
	3000	0.003	0.03	500	0.005	0.01	0.03	10°	
WD 1136+667	70 000	0.018	0.63	4300	0.54	0.33	3.70	64°	8
	5000	0.002	0.05	300		0.03	0.09	6°	
HS 1857+5144	70 000	0.019	0.60		0.19	0.21		53°	9
NN Ser	57 000	0.019	0.54	2920	0.177	0.15	0.954	85°	10
	3000	0.001	0.05	70	0.01	0.01	0.023	1°	
MT Ser PN	50 000	0.28	0.61		0.22	0.20		72°	11
			0.1			0.04		15°	

Appendix C

Photospheric abundances

All stellar atmosphere models presented in this work use solar photospheric abundances derived by Asplund *et al.* (2005). Since especially in chapter 5 the deviation to solar values are of great interest, one should note that Asplund *et al.* (2005) presented a strongly decreased metallicity compared to earlier works by Anders and Grevesse (1989) or Grevesse and Noels (1995) (unpublished, revised values of Grevesse *et al.* (1992) in Jaschek and Jaschek (1995)). Table C.1 summarizes the values of Asplund *et al.* (2005) and shows the differences compared to the older values by Grevesse and Noels (1995). Ratios are logarithmically scaled with hydrogen set to 12. The list of elements in PHOENIX is nearly complete up to $Z = 83$ except for technetium (^{43}Tc) and promethium (^{61}Pm). Only two more actinoids are available after that. As one can see the tendency is clearly towards lower values, especially for the important elements C , N and O , which are decreased by ~ 0.2 dex. For some abundances are no photospheric values available, so measurements of meteorites are used instead.
The solar photospheric abundance (A_{El}) in respect to hydrogen can be easily calculated from their logarithmically scale by:

$$A_{\mathrm{El}} = [\log \frac{N_{\mathrm{El}}}{N_{\mathrm{H}}} + 12.00]$$ (C.1)

where N is the number density of the element (El) respectively of hydrogen (H).

Name	Sym	Z	2005	1995	Name	Sym	Z	2005	1995
hydrogen	H	1	12.00	±.0	ruthenium	Ru	44	1.84	±.0
helium	He	2	10.93	−.06	rhodium	Rh	45	1.12	±.0
lithium	Li	3	1.05	−.06	palladium	Pd	46	1.69	±.0
beryllium	Be	4	1.38	−.04	silver	Ag	47	0.94	±.0
boron	B	5	2.70	−.18	cadmium	Cd	48	1.77	−.09
carbon	C	6	8.39	−.16	indium	In	49	1.60	−.06
nitrogen	N	7	7.78	−.19	tin	Sn	50	2.00	±.0
oxygen	O	8	8.66	−.21	antimony	Sb	51	1.00	±.0
fluorine	F	9	4.56	±.0	tellurium	Te	52	2.19	−.05
neon	Ne	10	7.84	−.24	iodine	I	53	1.51	±.0
sodium	Na	11	6.17	−.16	xenon	Xe	54	2.27	−.04
magnesium	Mg	12	7.53	−.05	caesium	Cs	55	1.07	−.05
aluminium	Al	13	6.37	−.11	barium	Ba	56	2.17	−.04
silicon	Si	14	7.51	−.04	lanthanum	La	57	1.13	−.09
phosphorus	P	15	5.36	−.09	cerium	Ce	58	1.58	+.03
sulfur	S	16	7.14	−.07	praseodymium	Pr	59	0.71	±.0
chlorine	Cl	17	5.50	±.0	neodymium	Nd	60	1.45	−.05
argon	Ar	18	6.18	−.34	samarium	Sm	62	1.01	+.01
potassium	K	19	5.08	−.04	europium	Eu	63	0.52	+.01
calcium	Ca	20	6.31	−.05	gadolinium	Gd	64	1.12	±.0
scandium	Sc	21	3.05	−.12	terbium	Tb	65	0.28	−.05
titanium	Ti	22	4.90	−.12	dysprosium	Dy	66	1.14	−.01
vanadium	V	23	4.00	±.0	holmium	Ho	67	0.51	+.01
chromium	Cr	24	5.64	−.03	erbium	Er	68	0.93	±.0
manganese	Mn	25	5.39	±.0	thulium	Tm	69	0.00	±.0
iron	Fe	26	7.45	−.05	ytterbium	Yb	70	1.08	±.0
cobalt	Co	27	4.92	±.0	lutetium	Lu	71	0.06	−.06
nickel	Ni	28	6.23	−.02	hafnium	Hf	72	0.88	±.0
copper	Cu	29	4.21	±.0	tantalum	Ta	73	−0.17	−.30
zinc	Zn	30	4.60	±.0	tungsten	W	74	1.11	±.0
gallium	Ga	31	2.88	±.0	rhenium	Re	75	0.23	−.04
germanium	Ge	32	3.58	+.17	osmium	Os	76	1.45	±.0
arsenic	As	33	2.29	−.08	iridium	Ir	77	1.38	+.03
selenium	Se	34	3.33	−.02	platinum	Pt	78	1.64	−.16
bromine	Br	35	2.56	−.07	gold	Au	79	1.01	±.0
krypton	Kr	36	3.28	+.05	mercury	Hg	80	1.13	+.04
rubidium	Rb	37	2.60	±.0	thallium	Tl	81	0.90	±.0
strontium	Sr	38	2.92	−.01	lead	Pb	82	2.00	−.05
yttrium	Y	39	2.21	−.03	bismuth	Bi	83	0.65	−.06
zirconium	Zr	40	2.59	−.01	thorium	Th	90	0.06	−.06
niobium	Nb	41	1.42	±.0	uranium	U	92	−0.52	−.03
molybdenum	Mo	42	1.92	±.0					

Table C.1: Solar photospheric abundances derived by Asplund *et al.* (2005) and the changes compared to older values by Grevesse and Noels (1995).

Appendix D

IDL routine

```
;The basic function to be used is patch_area, this calls a number of internal functions.
;patch_area is at the end of this file and documented in full.
;The internal function are not to be called directly by the user, therefore they are documented only shortly.

;Depending on the angle towards the line of sight some circles of theta_const on the sphere are not fully
;visible, because parts are on the back side. The function phi_limits_geom calculates the values of phi in
;the (theta,phi) coordinate system, which represent the boundaries of the visible area.
function phi_limits_geom, theta
common geom, omega, alphlow, alphhigh
;print, theta
if alphhigh lt abs(omega-theta) or alphlow gt !pi/2.< abs(omega+theta) then return ,[0. ,0.]
if omega eq 0. then begin
  if theta ge alphlow and omega lt alphhigh then return ,[0. ,!pi] else return , [0. ,0.]
endif else begin
  alphalow= abs(omega-theta)> alphlow
  alphahigh= (alphhigh <!pi/2.)<abs(omega+theta)
  temp=(cos(alphalow)-cos(theta)*cos(omega))/(sin(theta)*sin(omega))
  philow=acos((temp<1.))   ;due to numerical accuracy: acos is undefined for, e.g. temp=1.000000000000001
  temp=(cos(alphahigh)-cos(theta)*cos(omega))/(sin(theta)*sin(omega))
  phihigh=acos(temp>(-1.));due to numerical accuracy: acos is undefined for, e.g. temp=-1.000000000000001
  return ,[philow,phihigh]
endelse
end

;If the primary covers part of the secondary not the full theta = const circle is visible.
;This routine calculates the y-pos difference in an x-y coordinate system in the plane of the sky of the
;theta=const circle and the edge of the primary
function edge_of_prim, phi
common geom, omega, alphlow, alphhigh
common edge_of_prim, r_prim ,d,theta ,coverage , theta1 ,theta2
return,[-sin(theta)*sin(phi)+sqrt(r_prim^2.-((-cos(theta)+d)*sin(omega)+sin(theta)*cos(phi)*cos(omega))^2.)]
end

;This function solves edge_of_prim numerically to find the point of intersection of the sky of the theta=const
;circle and the edge of the primary.
function phi_edge_of_prim, theta_
common edge_of_prim, r_prim ,d,theta ,coverage , theta1 ,theta2
theta=theta_
phi=broyden([!pi -0.01], 'edge_of_prim')
if phi eq !pi -0.01 then message , 'Check_numerical_solution_of_edge_of_prim, _because _results _eq _initial _guess _-_
  ↪ suspicious!' ,/inform
;print, 'solution for phi is:', phi
return ,phi
end

;The patch_area is calculated as an 2D integration in a (theta,phi) coordinate system.
;Given a theta the phi limits depend on the geometric visibility (phi_limits_geom) and, possibly, the coverage
;by a primary star (phi_edge_of_prim). The function phi_limits checks if a given circle of theta=const is
;visible at all and, if necessary, calls phi_limits_geom and phi_edge_of_prim to determine the integration
;limits of phi.
function phi_limits , theta_
common edge_of_prim, r_prim ,d,theta ,coverage , theta1 ,theta2
common geom, omega, alphlow, alphhigh
theta=theta_
geom_limit=phi_limits_geom(theta)
if ~coverage then begin  ; primary is neglected as barrier
  return , geom_limit
endif else begin          ; primary potentially covers secondary
  if d*sin(omega) ge 1.+r_prim or omega ge !pi/2. then begin            ;no overlap
    return , geom_limit
  endif else begin
    if d*sin(omega) le r_prim -1. then begin            ; Primary covers secondary completely
      return , [0. ,0.]
    endif else begin     ; overlap of primary in front of secondary
      if theta ge theta1 and theta ge abs(theta2) then return , geom_limit else begin
```

```idl
         if theta le theta1 and theta le abs(theta2) then begin
           if theta2 ge 0. then return,geom_limit else return,[0,0]
         endif else begin
           edge_limit=phi_edge_of_prim(theta)
           ;print, geom_limit, edge_limit, theta, theta1, theta2, format='("philow,phihigh,phi_edge_of_prim,theta
              ↪ ,theta_max,theta_min: ",6f8.4)'
           ;the following lines looks complicated, but is necessary because
           ;geom_limit not only calculates which phi lies on the edge of the primary,
           ;but also takes care of the limits on alpha, which may lead to
           ;geom_limit[0]>edge_limit -> region is invisible
           if edge_limit lt geom_limit[0] then result=[0.,0.] else result=[geom_limit[0],geom_limit[1]<
              ↪ edge_limit]
           print, result
           return, result
         endelse ;theta le theta1 and theta le abs(theta2)
       endelse ;theta ge theta1 and theta ge abs(theta2)
     endelse ; Primary covers secondary completely
   endelse ;if overlap
 endelse ;if ~coverage
end


;area_2 is the projected patch area, given the angles omega, theta, phi.
;It is called int_2d in patch_area
function area_2 ,theta , phi
common geom, omega, alphlow , alphhigh
return ,2.*sin(theta)*(sin(theta)*cos(phi)*sin(omega)+cos(theta)*cos(omega))
end


;--- block of functions for alpha=[0,pi]
;This function returns the area of full circles on the side of the z>0 axis.
function a_fullcircle_dayside ,theta
common geom,omega, alphlow , alphhigh
if omega lt !pi/2. then begin
  theta_low  = 0 > theta[0]
  theta_high = theta[1] < (!pi/2.-omega)
  return, !pi*cos(omega)*((sin(theta_high))^2.-(sin(theta_low))^2.)
endif else begin
  return, 0.
endelse
end
;This function returns the area of full circles on the side of the z<0 axis
function a_fullcircle_nightside ,theta
common geom,omega, alphlow , alphhigh
if omega gt !pi/2. then begin
  theta_low  = (3./2.*!pi-omega) > theta[0]
  theta_high = theta[1] < !pi/2.
  return, !pi*cos(omega)*((sin(theta_high))^2.-(sin(theta_low))^2.)
endif else begin
  return, 0.
endelse
end
;This is the integrant for the a_partialcircle numerical integration.
function integrant_partialcircle ,theta
common geom,omega, alphlow , alphhigh
if omega eq 0 or theta eq 0 then begin
  return, 0
endif else begin
  if theta lt abs(!pi/2.-omega) or theta gt abs(!pi/2.+omega) then message ,'called for theta ,omega not in a
     ↪ partial circle: '+string(theta)+', '+string(omega)
  cotterm=(1./(tan(theta)*tan(omega)) < 1.) > (-1.)  ;the < 1.) > (-1.) is necessary due to numerical errors
     ↪ and, e.g. acos(1.00000001) is not defined
  return, (sin(theta))^2.*sin(omega)*2.*sqrt((1.-cotterm^2.)>0.)+sin(theta)*cos(theta)*cos(omega)*2.*(!pi-acos(
     ↪ cotterm))
endelse
end
; This function returns the visible , projected area of the partially visible circles .
function a_partialcircle ,theta
common geom,omega, alphlow , alphhigh
theta_low  = abs(!pi/2.-omega) > theta[0]
theta_high = theta[1] < abs(!pi/2.+omega)
if theta_low lt theta_high then return, qromb('integrant_partialcircle ',theta_low ,theta_high) else return, 0.
;print, theta_low , theta_high
end


;+
; NAME:
;       PATCH_AREA
;
; PURPOSE:
;       Given a sphere , e.g. a star , with a preferred axis this routine calculates the area of a patch on the
;       sphere , projected onto the plane of the sky. It allows to specify a range of angles to the preferred
;       axis and a range of viewing angles .
;       The original intention is to use it for irradiated secondaries in close binary systems . The preferred
;       axis points in this case towards the center of the primary , the range of angles theta specifies an area
;       of similar irradiation angles (and therefore temperature).
;       It further allows to restrict the calculation to patches on the sphere , which are seen under a
;       specified angle . This can be used for non-isotropic radiation from the secondary .
;       A more detailed description was presented in July 2008 on Cool Stars 15 in St. Andrews and will be
;       published in the upcoming conference proceedings by Wawrzyn et al., 2009.
;
```

```
;
; CALLING SEQUENCE:
;       RESULT=patch_area(omega,theta,[alpha[,r_prim,,r_sec,d_]],covertheta=covertheta)
;
; INPUTS:
;       omega:   angle between line-of-sight and preferred axis of the sphere
;       theta:   range of angles measured towards the specified axis in the form of an array=
;                [lowerbound, upperbound]
;
;
; OPTIONAL INPUTS:
;       alpha:  range of viewing angles in form of an array=[lowerbound, upperbound]
;       If coverage of the secondary by the primary shall be taken into account the following 3 parameters are
;       needed:
;       r_prim: radius of primary
;       r_sec:  radius of secondary
;       d:       distance between centers of primary and secondary
;       the unit of these three parameters is arbitrary, but needs to be consistent, e.g. all in solar radii
;
; OUTPUTS:
;       Projected patch area on unity sphere obeying the given angle restrictions
;
; OPTIONAL OUTPUTS:
;       covertheta: parameter useful for debugging
;                On output covertheta returns the lowest and highest theta angle, that is effected by coverage
;                of the primary
;
; COMMON BLOCKS:
;       GEOM:    Basic input angles (omega, alpha)
;       EDGE_OF_PRIM:   for coverage of secondary by primary this common block contains information to
;                        calculate the integration boundaries
;
; RESTRICTIONS:
;       This routine is meant for spherical objects only, so in the case of VERY close binaries with;
;       deformations it is not applicable.
;       For small regions the IDL numerical solvers produce considerable amount of numerical fluctuations,
;       visible, e.g. in the following example:
;       y=findgen(100)/100.
;       res=y*0.
;       for i=0,99 do res[i]=patch_area(y[i],[0.,!pi],[1.4,!pi/2.],.2,1.,3.)
;       plot, y,res
;
; PROCEDURE:
;       see Wawrzyn et al., upcoming CS15 conference proceedings, 2009
;       Basically this function uses a 2-dim integration in a (theta,phi) coordinate system on the spherical
;       surface.
;       Only if no boundaries on alpha are given one integration is done analytically and only over the
;       remaining dimension there is a numerical integration in order to limit the numerical errors. Therefore
;       the case n_params() splits the routine in distinct parts.
;
; EXAMPLE:
;       RESULT=patch_area(0.3,[0.2,.8],[!pi/4.,!pi/2.])
;
; MODIFICATION HISTORY:
;       Written by:    A.C. Wawrzyn & H.M. Guenther, Dec 2007
;       update, example & comments for CS15 (ACW - Jul 2008)
;       fixed typos & corrected reference (ACW - Jan 2009)
;-

function patch_area, omega_, theta, alpha, r_prim_, r_sec, d_, covertheta=covertheta
common geom, omega, alphlow, alphhigh
common edge_of_prim, r_prim, d, theta_, coverage, theta1, theta2
theta=[min(theta),max(theta)]
if theta[0] lt 0. or theta[1] gt !pi then message, 'This_routine_needs:_0_le_theta_le_!pi'
if omega_ lt 0. and omega_ gt -1e-7 then omega_=0. ;unfortunately necessary due to numerical uncertainties
if omega_ lt 0. or omega_ gt 2.*!pi then message, 'This_routine_needs:_0_le_omega_lt_2*pi'
if omega_ gt !pi then begin omega_=2*!pi-omega_ & message, 'By_symmetry_omega=2*!pi-omega',/informational &
    ↪ endif
case n_params() of
   2: begin
        coverage=0
        omega=omega_
        message, 'Integrating_over_alpha',/informational
        print, 'full_theta_circle_on_dayside:',(a_fullcircle_dayside(theta)>0.)
        print, 'partial:',(a_partialcircle(theta)>0.)
        print, 'full_theta_circle_on_nightside:',(a_fullcircle_nightside(theta)>0.)
        return,(a_fullcircle_dayside(theta)>0.)+(a_partialcircle(theta)>0.)+(a_fullcircle_nightside(theta)>0.)
     end
   3: begin
        coverage=0
        omega=omega_
        alphlow=min(alpha)
        alphhigh=max(alpha)
        if alphlow lt 0. then message, 'angle_to_line_of_sight_must_be_positive!'
        if alphlow gt !pi/2. then message, 'angle_to_line_of_sight_>_pi/2_->surface_not_visible!'
        if alphhigh gt !pi/2. then begin
          message, 'angle_to_line_of_sight_truncated_at_pi/2,_otherwise_not_visible!',/informational
          alphhigh=alphhigh <!pi/2.
        endif
        return, int_2d('area_2',[theta[0],theta[1]],'phi_limits',96,/double)
```

```
            end
       6: begin
           coverage=1
           d=d_/r_sec
           r_prim=r_prim_/r_sec
           omega=omega_
           alphlow=min([alpha[0],alpha[1]])
           alphhigh=max([alpha[0],alpha[1]])
           if alphlow lt 0. then message,'angle_to_line_of_sight_must_be_positive!'
           if alphlow gt !pi/2. then message,'angle_to_line_of_sight_>_pi/2_->surface_not_visible!'
           if alphhigh gt !pi/2. then begin
              message,'angle_to_line_of_sight_truncated_at_pi/2,_otherwise_not_visible!',/informational
              alphhigh=alphhigh <!pi/2.
           endif
           if d le 1.+r_sec then message,'sum_of_radii_larger_than_distance_of_centers!'
           if (d*sin(omega)+r_prim) gt −1. then begin
              if (d*sin(omega)+r_prim) lt 1. then theta1=asin(d*sin(omega)+r_prim)−omega else theta1= !pi/2.−omega ;
                   ↪ blue
           endif else theta1=−!pi/2.−omega
           if (d*sin(omega)−r_prim) gt −1. then begin
              if (d*sin(omega)−r_prim) lt 1. then theta2=asin(d*sin(omega)−r_prim)−omega else theta2= !pi/2.−omega ;
                   ↪ orange
           endif else theta2=−!pi/2.−omega
           covertheta=[theta1,theta2]
           return, int_2d('area_2',[theta[0],theta[1]],'phi_limits',96,/double)
       end
    else: begin
           message,'call_patch_area_as:_IDL>_result=_patch_area(omega,theta[,alpha])',/informational
           message,'with_theta_and_alpha_as_arrays_of_[lower_value,higher_value]',/informational
           return, −1
       end
endcase
end


;+
; NAME:
;        PATCH_AREA_PHYS
;
; PURPOSE:
;        Given a sphere, e.g. a star, with a preferred axis this routine calculates the area of a patch on the
;        sphere, projected onto the plane of the sky. It allows to specify a range of angles to the preferred
;        axis and a range of viewing angles.
;        The original intention is to use it for irradiated secondaries in close binary systems. The preferred
;        axis points in this case towards the center of the primary, the range of angles theta specifies an
;        area of similar irradiation angles (and therefore temperature).
;        It further allows to restrict the calculation to patches on the sphere, which are seen under a
;        specified angle.
;        This can be used for non−isotropic radiation from the secondary.
;        A more detailed description was presented in July 2008 on Cool Stars 15 in St. Andrews and will be
;        published in the upcoming conference proceedings by Wawrzyn et al., 2009.
;
;
; CALLING SEQUENCE:
;        RESULT=patch_area(phase,inclination,theta,[alpha[,r_prim_,r_sec,d_]],covertheta=covertheta)
;
; INPUTS:
;        phase: phase of binary system, range 0..1, with 0=primary eclipsing secondary
;        inclination:   i=0 is pole on, i=!pi/2. is edge−one
;        theta: range of angles measured towards the specified axis in the form of an array=
;                [lowerbound, upperbound]
;
;
; OPTIONAL INPUTS:
;        alpha: range of viewing angles in form of an array=[lowerbound, upperbound]
;        If coverage of the secondary by the primary shall be taken into account the following 3 parameters are
;        needed:
;        r_prim: radius of primary
;        r_sec:  radius of secondary
;        d:         distance between centers of primary and secondary
;        the unit of these three parameters is arbitrary, but needs to be consistent, e.g. all in solar radii
;
; OUTPUTS:
;        Projected patch area on unity sphere obeying the given angle restrictions
;
; OPTIONAL OUTPUTS:
;        covertheta: parameter useful for debugging
;                On output covertheta returns the lowest and highest theta angle, that is effected by coverage
;                of the primary
;
; COMMON BLOCKS:
;        GEOM:   Basic input angles (omega, alpha)
;        EDGE_OF_PRIM:  for coverage of secondary by primary this common block contains information to
;                        calculate the integration boundaries
;
; RESTRICTIONS:
;        see patch_area
;
; PROCEDURE:
;        see Wawrzyn et al., upcoming CS15 conference proceedings, 2009
;        This works like a wrapper for patch_area, converting physical properties of the orbit to the omega
```

```
;          angle.
;
; EXAMPLE:
;          RESULT=patch_area_phys(.2,1.5,[0.2,.8],[!pi/4.,!pi/2.])
;
; MODIFICATION HISTORY:
;          Written by:    A.C. Wawrzyn & H.M. Guenther, Dec 2007
;          update, example & comments for CS15 (ACW - Jul 2008)
;          fixed typos & corrected reference (ACW - Jan 2009)
;-
function patch_area_phys, phase, inclination, theta, alpha, r_prim_, r_sec, d_
case n_params() of
   3:return, patch_area(acos(cos(phase*2.*!pi)*sin(inclination)),theta)
   4:return, patch_area(acos(cos(phase*2.*!pi)*sin(inclination)),theta,alpha)
   7:return, patch_area(acos(cos(phase*2.*!pi)*sin(inclination)),theta,alpha,r_prim_,r_sec,d_)
endcase
end


; ;--- Examples ---
; ; maybe helpful for the construction of special cases and debugging
; y=findgen(100)/100.
; r_prim=.5
; d=3.
; covtheta=make_array(100,2)
; for i=0,99 do begin t=patch_area(y[i],[0.,0.],[0.,!pi/2.],r_prim,1.,d,cover=cover) & covtheta[i,*]=cover &
;        ↪ end
; theta1=covtheta[*,0]
; theta2=covtheta[*,1]
; wset,0
; plot, y,theta1
; oplot,y,abs(theta2),col=4
; part=y*0.
; mid=y*0.
; out=y*0.
; for i=0,99 do part[i]= patch_area(y[i],[abs(theta2[i]),theta1[i]],[0.,!pi/2.],r_prim,1.,d)
; for i=0,99 do mid[i]= patch_area(y[i],[0.,abs(theta2[i])],[0.,!pi/2.],r_prim,1.,d)
; for i=0,99 do out[i]= patch_area(y[i],[theta1[i],!pi],[0.,!pi/2.],r_prim,1.,d)
; wset,1
; plot, y,part+mid+out
; oplot, y,mid
; oplot,y,part,line=1
; oplot,y,out,line=2


; ;plot of constant theta
; y=findgen(100)/100.
; r_prim=.5
; d=3.
; n=8
; results=make_array(100,n)
; for j=0,n-1 do for i=0,99 do results[i,j]= patch_area(y[i],[j*!pi/n,(j+1)*!pi/n],[0.,!pi/2.],r_prim,1.,d)
; plot, y,results[*,0],yr=[0,4]
; for i=1,n-1 do oplot,y,total(results[*,0:i],2)
;
; ;plot of the areas of constant alpha - prim covers large alpha first
; set_plot,'ps'
; device,filename='geomalpha'
; y=findgen(100)/100.
; r_prim=.65
; d=3.
; n=8
; results=make_array(100,n)
; for j=0,n-1 do for i=0,99 do results[i,j]= patch_area(y[i],[0,!pi],[j*!pi/2./n,(j+1)*!pi/2./n],r_prim,1.,d)
; results=results/!pi
; plot, y,results[*,0],yr=[0,1],xtit='Phase',ytit='Partial coverage'
; for i=1,n-1 do oplot,y,total(results[*,0:i],2)
;device,/close
; set_plot,'x'
;
; ; --- Plotting the theta=const lines on sphere
; ; plot, cos(theta)*sin(-omega)+sin(theta)*cos(phi)*cos(-omega),sin(theta)*sin(phi)
; ; oplot,x,sqrt(.25-(x+3.*sin(omega))^2.),col=6
```

Bibliography

Abell, G. O., *Properties of Some Old Planetary Nebulae*, Astrophysical Journal **144**, 259–+ (1966).

Afşar, M. and Ibanoğlu, C. (2004), Photometric Observations of the Binary Nuclei of Three Abell Planetary Nebulae, in *Asymmetrical Planetary Nebulae III: Winds, Structure and the Thunderbird*, edited by Meixner, M., Kastner, J. H., Balick, B., and Soker, N., volume 313 of *Astronomical Society of the Pacific Conference Series*, pages 525–+.

Alexander, M. E., Chau, W. Y., and Henriksen, R. N., *Orbital evolution of a singly condensed, close binary, by mass loss from the primary and by accretion drag on the condensed member*, Astrophysical Journal **204**, 879–888 (1976).

Allard, F., Hauschildt, P. H., Alexander, D. R., Tamanai, A., and Schweitzer, A., *The Limiting Effects of Dust in Brown Dwarf Model Atmospheres*, Astrophysical Journal **556**, 357–372 (2001).

Anders, E. and Grevesse, N., *Abundances of the elements - Meteoritic and solar*, Geochimica Cosmochimica Acta **53**, 197–214 (1989).

Asplund, M., Grevesse, N., and Sauval, A. J. (2005), The Solar Chemical Composition, in *ASP Conf. Ser. 336: Cosmic Abundances as Records of Stellar Evolution and Nucleosynthesis*, pages 25–+.

Auer, L. H., *The stellar atmospheres problem.*, Journal of Quantitative Spectroscopy and Radiative Transfer **11**, 573–587 (1971).

Aufdenberg, J. P., *Line-blanketed Spherically Extended Model Atmospheres of Hot Luminous Stars with and without Winds*, PASP **113**, 119–120 (2001).

Aungwerojwit, A., Gänsicke, B. T., Rodríguez-Gil, P., Hagen, H.-J., Giannakis, O., Papadimitriou, C., Allende Prieto, C., and Engels, D., *HS 1857+5144: a hot and young pre-cataclysmic variable*, Astronomy and Astrophysics **469**, 297–305 (2007).

Barber, R. J., Tennyson, J., Harris, G. J., and Tolchenov, R. N., *A high-accuracy computed water line list*, MNRAS **368**, 1087–1094 (2006).

Barman, T. S. (2002), *Irradiated model atmospheres for extrasolar planets and secondary stars of pre-cataclysmic variables*, PhD thesis, University of Georgia.

Barman, T. S., Hauschildt, P. H., and Allard, F., *Model Atmospheres for Irradiated Stars in Precataclysmic Variables*, Astrophysical Journal **614**, 338–348 (2004).

Barman, T. S., Hauschildt, P. H., and Allard, F., *Phase-Dependent Properties of Extrasolar Planet Atmospheres*, *Astrophysical Journal* **632**, 1132–1139 (2005).

Baron, E. and Hauschildt, P. H., *A 3D radiative transfer framework. II. Line transfer problems*, *Astronomy and Astrophysics* **468**, 255–261 (2007).

Beer, M. E., Dray, L. M., King, A. R., and Wynn, G. A., *An alternative to common envelope evolution*, *MNRAS* **375**, 1000–1008 (2007).

Beer, M. E. and Podsiadlowski, P., *A general three-dimensional fluid dynamics code for stars in binary systems*, *MNRAS* **335**, 358–368 (2002).

Bell, R. A., *The calibration of narrow band photometry - I. Cambridge observations of G and K giants.*, *MNRAS* **148**, 25–52 (1970).

Bell, R. A., *The calculation of flux constant line-blanketed model atmospheres for solar type stars.*, *MNRAS* **164**, 197–210 (1973).

Bell, S. A., Pollacco, D. L., and Hilditch, R. W., *Direct Optical Observations of the Secondary Component of UU Sagittae*, *MNRAS* **270**, 449–+ (1994).

Bernath, P. (2006), Metal Hydrides in Astronomy, in *Astrochemistry - From Laboratory Studies to Astronomical Observations*, edited by Kaiser, R. I., Bernath, P., Osamura, Y., Petrie, S., and Mebel, A. M., volume 855 of *American Institute of Physics Conference Series*, pages 143–148.

Bernath, P. (2007), Laboratory Data for Cool Star Modelling, in *Why Galaxies Care About AGB Stars: Their Importance as Actors and Probes*, edited by Kerschbaum, F., Charbonnel, C., and Wing, R. F., volume 378 of *Astronomical Society of the Pacific Conference Series*, pages 71–+.

Böhm-Vitense, E. (1989), *Introduction to Stellar Astrophysics*, Introduction to Stellar Astrophysics, by Erika Böhm-Vitense, pp. 256. ISBN 0521348692. Cambridge, UK: Cambridge University Press, August 1989.

Bond, H. E., *Objects common to the Catalogue of Galactic Planetary Nebulae and the General Catalogue of Variable Stars.*, *PASP* **88**, 192–194 (1976).

Bond, H. E., Liller, W., and Mannery, E. J., *UU Sagittae - Eclipsing nucleus of the planetary nebula Abell 63*, *Astrophysical Journal* **223**, 252–+ (1978).

Borysow, A. and Frommhold, L., *Collision-induced rototranslational absorption spectra of N2-N2 pairs for temperatures from 50 to 300 K*, *Astrophysical Journal* **311**, 1043–1057 (1986a).

Borysow, A. and Frommhold, L., *Theoretical collision-induced rototranslational absorption spectra for modeling Titan's atmosphere - H2-N2 pairs*, *Astrophysical Journal* **303**, 495–510 (1986b).

Borysow, A. and Frommhold, L., *Theoretical collision-induced rototranslational absorption spectra for the outer planets - H2-CH4 pairs*, *Astrophysical Journal* **304**, 849–865 (1986c).

Borysow, A. and Frommhold, L., *Collision-induced rototranslational absorption spectra of CH4-CH4 pairs at temperatures from 50 to 300 K*, Astrophysical Journal **318**, 940–943 (1987a).

Borysow, A. and Frommhold, L., *Collision-induced Rototranslational Absorption Spectra of N 2–N 2 Pairs for Temperatures from 50 to 300 K: Erratum*, Astrophysical Journal **320**, 437–+ (1987b).

Borysow, A., Jorgensen, U. G., and Zheng, C., *Model atmospheres of cool, low-metallicity stars: the importance of collision-induced absorption.*, Astronomy and Astrophysics **324**, 185–195 (1997).

Borysow, A. and Tang, C., *Far Infrared CIA Spectra of $N_2 - CH_4$ Pairs for Modeling of Titan's Atmosphere*, Icarus **105**, 175–183 (1993).

Brett, J. M. and Smith, R. C., *A model atmosphere investigation of the effects of irradiation on the secondary star in a dwarf nova.*, MNRAS **264**, 641–+ (1993).

Budding, E. (1981), Observations and Analysis of Uu-Sagittae, in *Photometric and Spectroscopic Binary Systems*, edited by Carling, E. B. and Kopal, Z., pages 405–+.

Budding, E. and Kopal, Z., *Photovisual light curve and photometric elements of the eclipsing nucleus of the planetary nebula Abell 63*, Ap&SS **73**, 83–100 (1980).

Cannon, C. J., *Frequency-Quadrature Perturbations in Radiative-Transfer Theory*, Astrophysical Journal **185**, 621–630 (1973).

Chase, M. W. J., Davies, C. A., Downey, J. R. J., Frurip, D. J., McDonald, R. A., and Syverud, A. N., *JANAF Thermochemical Tables*, J. Phys. Ref. Data **14**, Suppl. No. 1 (1985).

Chau, W. Y., Henriksen, R. N., and Alexander, M. E. (1974), Demise of a binary system., in *Bulletin of the American Astronomical Society*, volume 6 of *Bulletin of the American Astronomical Society*, pages 488–+.

Chen, A., O'Donoghue, D., Stobie, R. S., Kilkenny, D., Roberts, G., and van Wyk, F., *EC11575-1845: a new close binary with a large reflection effect discovered by the Edinburgh-Cape Survey*, MNRAS **275**, 100–114 (1995).

Claret, A. and Giménez, A. (2001), Physical processes in close binary systems, in *Binary Stars: Selected Topics on Observations and Physical Processes*, edited by Lázaro, F. C. and Arévalo, M. J., volume 563 of *Lecture Notes in Physics, Berlin Springer Verlag*, pages 1–47.

de Greve, J. P. and Cugier, H., *Evolution of the surface abundance of carbon in mass-exchanging binaries*, Astronomy and Astrophysics **211**, 356–360 (1989).

de Kool, M. and Ritter, H., *On the formation rate and space density of close white dwarf main sequence star binaries*, Astronomy and Astrophysics **267**, 397–409 (1993).

Dreizler, S. and Murdin, P., *sdO Stars*, Encyclopedia of Astronomy and Astrophysics (2000).

Eddington, A. S., *The reflection effect in eclipsing variables*, *MNRAS* **86**, 320–327 (1926).

Eggleton, P. P., *Approximations to the radii of Roche lobes*, *Astrophysical Journal* **268**, 368–+ (1983).

Engels, D., *AGB and post-AGB stars .*, *Memorie della Societa Astronomica Italiana* **76**, 441–+ (2005).

Exter, K. M., Pollacco, D. L., and Bell, S. A., *The planetary nebula K 1-2 and its binary central star VW Pyx*, *MNRAS* **341**, 1349–1359 (2003).

Exter, K. M., Pollacco, D. L., Maxted, P. F. L., Napiwotzki, R., and Bell, S. A., *A study of two post-common envelope binary systems*, *MNRAS* **359**, 315–327 (2005).

Ferguson, D. H., Liebert, J., Cutri, R., Green, R. F., Willner, S. P., Steiner, J. E., and Tokarz, S., *BE Ursae Majoris - A detached binary with a unique reprocessing spectrum*, *Astrophysical Journal* **316**, 399–410 (1987).

Goorvitch, D., *Infrared CO line for the X 1 Sigma(+) state*, *Astrophysical Journal, Supplement* **95**, 535–552 (1994).

Goorvitch, D. and Chackerian, C., *Calculation of (12)C(16)O and (13)C(16)O X(1)Sigma(+) rovibrational intensities for V less than or equal to 20 and J less than or equal to 150*, *Astrophysical Journal, Supplement* **91**, 483–489 (1994a).

Goorvitch, D. and Chackerian, C., *Rovibrational intensities of the minor isotopes of the CO X ^{1}Sigma $^+$ state for V less than or equal to 20 and J less than or equal to 150*, *Astrophysical Journal, Supplement* **92**, 311–321 (1994b).

Grevesse, N., Noels, A., and Sauval, A. J. (1992), Photospheric abundances, in *ESA SP-348: Coronal Streamers, Coronal Loops, and Coronal and Solar Wind Composition*, pages 305–308.

Grossmann, L., *Condensation in the primitive solar nebula*, *Geochim. Cosmochim. Acta* **36**, 597–619 (1972).

Gruszka, M. and Borysow, A., *Roto-Translational Collision-Induced Absorption of CO_2 for the Atmosphere of Venus at Frequencies from 0 to 250 cm^-1, at Temperatures from 200 to 800 K*, *Icarus* **129**, 172–177 (1997).

Gustafsson, B., Bell, R. A., Eriksson, K., and Nordlund, A., *A grid of model atmospheres for metal-deficient giant stars. I*, *Astronomy and Astrophysics* **42**, 407–432 (1975).

Gustafsson, B., Edvardsson, B., Eriksson, K., Jørgensen, U. G., Nordlund, Å., and Plez, B., *A grid of MARCS model atmospheres for late-type stars. I. Methods and general properties*, *Astronomy and Astrophysics* **486**, 951–970 (2008).

Haefner, R., Fiedler, A., Butler, K., and Barwig, H., *Refined system parameters for the pre-cataclysmic binary NN Serpentis*, *Astronomy and Astrophysics* **428**, 181–190 (2004).

Hauschildt, P. H., *A fast operator perturbation method for the solution of the special relativistic equation of radiative transfer in spherical symmetry*, *Journal of Quantitative Spectroscopy and Radiative Transfer* **47**, 433–453 (1992).

Hauschildt, P. H. and Baron, E., *Numerical solution of the expanding stellar atmosphere problem*, Journal of Computational and Applied Mathematics **109**, 41–63 (1999a).

Hauschildt, P. H. and Baron, E., *Numerical solution of the expanding stellar atmosphere problem*, J. Comput. Appl. Math. **109**, 41–63 (1999b).

Hauschildt, P. H. and Baron, E., *A 3D radiative transfer framework. I. Non-local operator splitting and continuum scattering problems*, Astronomy and Astrophysics **451**, 273–284 (2006).

Hauschildt, P. H. and Baron, E., *A 3D radiative transfer framework. III. Periodic boundary conditions*, Astronomy and Astrophysics **490**, 873–877 (2008).

Helling, C., Dehn, M., Woitke, P., and Hauschildt, P. H., *Consistent Simulations of Substellar Atmospheres and Nonequilibrium Dust Cloud Formation*, Astrophysical Journal, Letters **675**, L105–L108 (2008a).

Helling, C., Dehn, M., Woitke, P., and Hauschildt, P. H., *Erratum: "Consistent Simulations of Substellar Atmospheres and Nonequilibrium Dust Cloud Formation" (ApJ, 675, L105 [2008])*, Astrophysical Journal, Letters **677**, L157–L157 (2008b).

Helling, C., Woitke, P., and Thi, W.-F., *Dust in brown dwarfs and extra-solar planets. I. Chemical composition and spectral appearance of quasi-static cloud layers*, Astronomy and Astrophysics **485**, 547–560 (2008c).

Herschel, M. and Banks, J., *On the Parallax of the Fixed Stars. By Mr. Herschel, F. R. S.; Communicated by Sir Joseph Banks, Bart, P. R. S.*, Philosophical Transactions Series I **72**, 82–111 (1782).

Herschel, M. and Watson, D., *Catalogue of Double Stars. By Mr. Herschel, F. R. S. Communicated by Dr. Watson, Jun.*, Philosophical Transactions Series I **72**, 112–162 (1782).

Herschel, W., *Catalogue of Double Stars. By William Herschel, Esq. F. R. S.*, Philosophical Transactions Series I **75**, 40–126 (1785).

Herschel, W., *Catalogue of 500 New Nebulae, Nebulous Stars, Planetary Nebulae, and Clusters of Stars; With Remarks on the Construction of the Heavens*, Philosophical Transactions Series I **92**, 477–528 (1802).

Herwig, F., *Evolution of Asymptotic Giant Branch Stars*, ARA&A **43**, 435–479 (2005).

Hilditch, R. W., Harries, T. J., and Hill, G., *On the reflection effect in three sdOB binary stars.*, MNRAS **279**, 1380–1392 (1996).

Hillwig, T. C., Honeycutt, R. K., and Robertson, J. W., *Post-Common-Envelope Binary Stars and the Precataclysmic Binary PG 1114+187*, AJ **120**, 1113–1119 (2000).

Hjellming, M. S. and Taam, R. E., *The response of main-sequence stars within a common envelope*, Astrophysical Journal **370**, 709–716 (1991).

Hoffleit, D., *New Variable Stars in Aquila*, Harvard College Observatory Bulletin **887**, 9–13 (1932).

Hubeny, I., *A computer program for calculating non-LTE model stellar atmospheres*, *Computer Physics Communications* **52**, 103–132 (1988).

Hubeny, I. and Lanz, T., *Special Line Profiles*, *http://nova.astro.umd.edu/Synspec43/synspec-stark.html* (2000).

Husson, N., Bonnet, B., Scott, N. A., and Chedin, A., *Management and Study of Spectroscopic Information-The GEISA program*, *Journal of Quantitative Spectroscopy and Radiative Transfer* **48**, 509–518 (1992).

Iben, I. and Tutukov, A. V. (1989), Binary stars and planetary nebulae., in *Planetary Nebulae*, edited by Torres-Peimbert, S., volume 131 of *IAU Symposium*, pages 505–522.

Iben, I. J. and Livio, M., *Common envelopes in binary star evolution*, *PASP* **105**, 1373–1406 (1993).

Iben, I. J. and Tutukov, A. V., *Formation and Evolution of Binary Planetary Nebula Nuclei and Related Objects*, *Astrophysical Journal* **418**, 343–+ (1993).

Jaschek, C. and Jaschek, M. (1995), *The behavior of chemical elements in stars*, Cambridge; New York: Cambridge University Press, 1995.

Jorgensen, U. G., *Effects of TiO in stellar atmospheres*, *Astronomy and Astrophysics* **284**, 179–186 (1994).

Kopal, Z. (1959), *Close binary systems*, The International Astrophysics Series, London: Chapman Hall, 1959.

Kurucz, R., *Atomic data for opacity calculations.*, *Atomic data for opacity calculations. Kurucz CD-ROM No. 1. Cambridge, Mass.: Smithsonian Astrophysical Observatory, 1993.* **1** (1993a).

Kurucz, R., *Diatomic Molecular Data for Opacity Calculations.*, *Diatomic Molecular Data for Opacity Calculations. Kurucz CD-ROM No. 15. Cambridge, Mass.: Smithsonian Astrophysical Observatory, 1993.* **15** (1993b).

Kurucz, R., *Atomic Data for Fe and Ni.*, *Atomic Data for Fe and Ni. Kurucz CD-ROM No. 22. Cambridge, Mass.: Smithsonian Astrophysical Observatory, 1994.* **22** (1994).

Kurucz, R. and Bell, B., *Atomic Line Data*, *Atomic Line Data (R.L. Kurucz and B. Bell) Kurucz CD-ROM No. 23. Cambridge, Mass.: Smithsonian Astrophysical Observatory, 1995.* **23** (1995a).

Kurucz, R. and Bell, B., *Atomic line list*, *http://kurucz.havard.edu/atoms.html* (2006).

Kurucz, R. L. (1996), Status of the ATLAS 12 Opacity Sampling Program and of New Programs for Rosseland and for Distribution Function Opacity, in *M.A.S.S., Model Atmospheres and Spectrum Synthesis*, edited by Adelman, S. J., Kupka, F., and Weiss, W. W., volume 108 of *Astronomical Society of the Pacific Conference Series*, pages 160–+.

Kurucz, R. L. and Bell, B. (1995b), *Atomic line list*, Kurucz CD-ROM, Cambridge, MA: Smithsonian Astrophysical Observatory, —c1995, April 15, 1995.

Landolt, A. U. and Drilling, J. S., *Multicolor photometry of the binary central star LSS 2018*, *AJ* **91**, 1372–1375 (1986).

Langer, N., Deutschmann, A., Wellstein, S., and Höflich, P., *The evolution of main sequence star + white dwarf binary systems towards Type Ia supernovae*, Astronomy and Astrophysics **362**, 1046–1064 (2000).

Langhoff, S. R., *Theoretical Study of the Spectroscopy of TiO*, Astrophysical Journal **481**, 1007–+ (1997).

Livio, M. (1996), Common Envelope Evolution, in *The Origins, Evolution, and Destinies of Binary Stars in Clusters*, edited by Milone, E. F. and Mermilliod, J.-C., volume 90 of *Astronomical Society of the Pacific Conference Series*, pages 291–+.

Lucy, L. B., *A Temperature-Correction Procedure*, *SAO Special Report* **167**, 93–+ (1964).

Marks, P. B. and Sarna, M. J., *The chemical evolution of the secondary stars in close binaries, arising from common-envelope evolution and nova outbursts*, MNRAS **301**, 699–720 (1998).

Marsh, T. R., *Detached white-dwarf close-binary stars - CV's extended family*, New Astronomy Review **44**, 119–124 (2000).

Mathisen, R., *Photo cross sections for stellar atmosphere calculations - compilation of references and data, Inst. of Theoret. Astrophys. Univ. of Oslo, Publ. Series No. 1*, Astronomy and Astrophysics (1984).

Merrill, P. W., Deutsch, A. J., and Keenan, P. C., *Absorption Spectra of M-Type Mira Variables.*, Astrophysical Journal **136**, 21–+ (1962).

Mihalas, D. (1970), *Stellar atmospheres*, Series of Books in Astronomy and Astrophysics, San Francisco: Freeman, —c1970.

Mihalas, D. (1978), *Stellar atmospheres /2nd edition/*, San Francisco, W. H. Freeman and Co., 1978. 650 p.

Miller, J. S., Krzeminski, W., and Priedhorsky, W., *UU Sagittae*, *IAU Circ.* **2974**, 2–+ (1976).

Miller, S., Tennyson, J., Jones, H., and Longmore, A. (1994), Computation of Frequencies and Linestrengths for Triatomic Molecules of Astronomical Interest, in *Molecular Opacities in the Stellar Environment*, edited by Thejll, P. and Jorgensen, U., I.A.U. Colloquium 146, Niels Bohr Institute and Nordita press, Copenhagen.

Moehler, S., Landsman, W., and Napiwotzki, R., *Hot UV bright stars in globular clusters*, Astronomy and Astrophysics **335**, 510–516 (1998).

Napier, W. M., *The Photometric Reflection Effect in Close Binaries*, *Ap&SS* **2**, 61–+ (1968).

Nelemans, G. and Tout, C. A., *Reconstructing the evolution of white dwarf binaries: further evidence for an alternative algorithm for the outcome of the common-envelope phase in close binaries*, MNRAS **356**, 753–764 (2005).

Newton, I. (1687), *Philosophiæ Naturalis Principia Mathematica*, London : Dawson, 1687.

Nordlund, A. and Vaz, L. P. R., *The reflection effect in model stellar atmospheres. II - The bolometric reflection albedo in non-grey atmospheres with convection*, Astronomy and Astrophysics **228**, 231–237 (1990).

Olson, G. L. and Kunasz, P. B., *Short characteristic solution of the non-LTE transfer problem by operator perturbation. I. The one-dimensional planar slab.*, Journal of Quantitative Spectroscopy and Radiative Transfer **38**, 325–336 (1987).

Orosz, J. A. and Hauschildt, P. H., *The use of the NextGen model atmospheres for cool giants in a light curve synthesis code*, Astronomy and Astrophysics **364**, 265–281 (2000).

Paczyński, B., *Evolutionary Processes in Close Binary Systems*, ARA&A **9**, 183–+ (1971).

Paczynski, B. (1976), Common Envelope Binaries, in *Structure and Evolution of Close Binary Systems*, edited by Eggleton, P., Mitton, S., and Whelan, J., volume 73 of *IAU Symposium*, pages 75–+.

Partridge, H. and Schwenke, D. W., *The determination of an accurate isotope dependent potential energy surface for water from extensive ab initio calculations and experimental data*, Journal of Chemical Physics **106** (1997).

Phillips, J. G. and Davis, S. P., *On the carrier of the band at 700 nanometers in the iron hydride spectrum*, Astrophysical Journal **409**, 860–868 (1993).

Plez, B., *A new TiO line list*, Astronomy and Astrophysics **337**, 495–500 (1998).

Pollacco, D. L. and Bell, S. A., *New light on UU Sagittae*, MNRAS **262**, 377–391 (1993).

Pollacco, D. L. and Bell, S. A., *A preliminary analysis of the planetary nebula central star V477 Lyrae*, MNRAS **267**, 452–464 (1994).

Prialnik, D. and Livio, M., *The outcome of accretion on to a fully convective star Expansion or contraction?*, MNRAS **216**, 37–52 (1985).

Pringle, J. E. and Wade, R. A. (1985), *Interacting binary stars*, Interacting Binary Stars.

Pustynski, V.-V. and Pustylnik, I. (2005), A New Computer Code for Analyzing the Light Curves of Eclipsing Pre-Cataclysmic Binaries (PCBs): Application to UU Sge and V477 Lyr, in *14th European Workshop on White Dwarfs*, edited by Koester, D. and Moehler, S., volume 334 of *Astronomical Society of the Pacific Conference Series*, pages 639–+.

Rasio, F. A. and Livio, M., *On the Formation and Evolution of Common Envelope Systems*, Astrophysical Journal **471**, 366–+ (1996).

Refsdal, S., Roth, M. L., and Weigert, A., *On the binary system AS Eri.*, Astronomy and Astrophysics **36**, 113–122 (1974).

Ritter, H., *Precataclysmic binaries*, Astronomy and Astrophysics **169**, 139–148 (1986).

Ritter, H. and Kolb, U., *Catalogue of cataclysmic binaries, low-mass X-ray binaries and related objects (Seventh edition)*, Astronomy and Astrophysics **404**, 301–303 (2003).

Rothman, L., Jacquemart, D., and et al., *The HITRAN 2004 molecular spectroscopic database*, *Journal of Quantitiative Spectroscopy and Radiative Trasfer* **96**, 139–204 (2005).

Rothman, L. S., Gamache, R. R., Tipping, R. H., Rinsland, C. P., Smith, M. A. H., Benner, D. C., Devi, V. M., Flaud, J.-M., Camy-Peyret, C., and Perrin, A., *The HITRAN molecular data base - Editions of 1991 and 1992*, *Journal of Quantitative Spectroscopy and Radiative Transfer* **48**, 469–507 (1992).

Rybicki, G. B. and Hummer, D. G., *An accelerated lambda iteration method for multilevel radiative transfer. I - Non-overlapping lines with background continuum*, *Astronomy and Astrophysics* **245**, 171–181 (1991).

Samuelson, R. E., Nath, N. R., and Borysow, A., *Gaseous abundances and methane supersaturation in Titan's troposphere*, *Planet. Space Sci.* **45**, 959–980 (1997).

Sandquist, E. L., Taam, R. E., Chen, X., Bodenheimer, P., and Burkert, A., *Double Core Evolution. X. Through the Envelope Ejection Phase*, *Astrophysical Journal* **500**, 909–+ (1998).

Sarna, M. J., Marks, P. B., and Connon Smith, R., *Evolutionary scenarios for double degenerate systems*, *MNRAS* **279**, 88–94 (1996).

Sarna, M. J. and Ziolkowski, J., *Effect of rapid mass accretion onto the low-mass main sequence stars. II*, *Acta Astronomica* **38**, 89–106 (1988).

Schmidt, G. D., Smith, P. S., Harvey, D. A., and Grauer, A. D., *The Precataclysmic Variable GD 245*, *AJ* **110**, 398–+ (1995).

Schryber, H., , S., and Tennyson, J., *Computed Infra Red Absorption Properties of Hot Water Vapor*, *Journal of Quantitative Spectroscopy and Radiative Transfer* **53**, 373 (1995).

Schweitzer, A. (1995), Modellatmosphären für M-Zwerge, Master's thesis, Univ. Heidelberg (1995).

Schweitzer, A. (1999), *Spectra of M dwarfs in non-LTE and with low metallicities*, PhD thesis, Landessternwarte Heidelberg/Königstuhl (1999).

Schweitzer, A., Hauschildt, P. H., Allard, F., and Basri, G., *Analysis of Keck high-resolution spectra of VB 10*, *MNRAS* **283**, 821–829 (1996).

Schwenke, D. W. (1998), Opacity of TiO from a coupled electronic state calculation parametrized by AB initio and experimental data, in *Chemistry and Physics of Molecules and Grains in Space. Faraday Discussions No. 109*, pages 321–+.

Shimanskii, V. V., Borisov, N. V., Pozdnyakova, S. A., Bikmaev, I. F., Vlasyuk, V. V., Sakhibullin, N. A., and Spiridonova, O. I., *Fundamental parameters of BE UMa revised*, *Astronomy Reports* **52**, 558–575 (2008a).

Shimanskii, V. V., Borisov, N. V., Sakhibullin, N. A., and Sheveleva, D. V., *MT Ser, a binary blue subdwarf*, *Astronomy Reports* **52**, 479–486 (2008b).

Shimanskii, V. V., Borisov, N. V., Sakhibullin, N. A., and Surkov, A. E., *The Nature of the Unique Precataclysmic Variable V664 Cas with Two-Peaked Balmer Lines in Its Spectrum*, *Astronomy Reports* **48**, 563–576 (2004).

Shimansky, V., Sakhibullin, N. A., Bikmaev, I., Ritter, H., Suleimanov, V., Borisov, N., and Galeev, A., *The new pre-cataclysmic binary PG 2200+085*, *Astronomy and Astrophysics* **456**, 1069–1075 (2006).

Shimansky, V. V., Pozdnyakova, S. A., Borisov, N. V., Bikmaev, I. F., Galeev, A. I., Sakhibullin, N. A., and Spiridonova, O. I., *Analysis of Fundamental Parameters for V477 Lyr*, *Astronomy Letters* **34**, 423–437 (2008).

Sing, D. K., Holberg, J. B., Barstow, M. A., Burleigh, M., Good, S., Oswalt, T., Howell, S., and Brinkworth, C. (2003), HS1136+6646: A Hot DAO.5+K6V Young Post-CE Pre-CV Binary, in *NATO ASIB Proc. 105: White Dwarfs*, edited by de Martino, D., Silvotti, R., Solheim, J.-E., and Kalytis, R., pages 349–+.

Soberman, G. E., Phinney, E. S., and van den Heuvel, E. P. J., *Stability criteria for mass transfer in binary stellar evolution.*, *Astronomy and Astrophysics* **327**, 620–635 (1997).

Sparks, W. M. and Stecher, T. P., *Supernova: The Result of the Death Spiral of a White Dwarf into a Red Giant*, *Astrophysical Journal* **188**, 149–+ (1974).

Taam, R. E. and Bodenheimer, P., *Double-core evolution. III - The evolution of a 5 solar mass red giant with a 1 solar mass companion*, *Astrophysical Journal* **337**, 849–857 (1989).

Taam, R. E. and Ricker, P. M., *Common Envelope Evolution*, *ArXiv Astrophysics e-prints* (2006).

Taam, R. E. and Sandquist, E. L., *Common Envelope Evolution of Massive Binary Stars*, *ARA&A* **38**, 113–141 (2000).

Thomas, H.-C., *Consequences of mass transfer in close binary systems*, *ARA&A* **15**, 127–151 (1977).

Toledano, O., Moreno, E., Koenigsberger, G., Detmers, R., and Langer, N., *Tides in asynchronous binary systems*, *Astronomy and Astrophysics* **461**, 1057–1063 (2007).

Tsuji, T. (1995), The Bottom of the Main Sequence - and Beyond, in *Proceedings of the ESO Workshop Held in Garching, Germany, 10-12 August 1994, XVII, 309 pp.. Springer-Verlag Berlin Heidelberg New York. Also ESO Astrophysics Symposia (European Southern Observatory)*, edited by Tinney, C.

Tsuji, T., Ohnaka, K., and Aoki, W., *Dust formation in stellar photospheres: a case of very low mass stars and a possible resolution on the effective temperature scale of M dwarfs.*, *Astronomy and Astrophysics* **305**, L1+ (1996a).

Tsuji, T., Ohnaka, K., Aoki, W., and Nakajima, T., *Evolution of dusty photospheres through red to brown dwarfs: how dust forms in very low mass objects.*, *Astronomy and Astrophysics* **308**, L29–L32 (1996b).

van Winckel, H., *Post-Agb Stars*, *ARA&A* **41**, 391–427 (2003).

Vanbeveren, D., De Loore, C., and Van Rensbergen, W., *Massive stars*, *A&A Rev.* **9**, 63–152 (1998).

Vaz, L. P. R. and Nordlund, A., *The reflection effect in model stellar atmospheres. I - Grey atmospheres with convection*, *Astronomy and Astrophysics* **147**, 281–299 (1985).

Verner, D. A. and Yakovlev, D. G., *Analytic FITS for partial photoionization cross sections.*, *A&AS* **109**, 125–133 (1995).

Walton, N. A., Walsh, J. R., and Pottasch, S. R., *Imaging and Spectroscopy of ABELL:63 Uu-Sagittae*, *Astronomy and Astrophysics* **275**, 256–+ (1993).

Warner, B. (1995), *Cataclysmic variable stars*, Cambridge Astrophysics Series, Cambridge, New York: Cambridge University Press, —c1995.

Wawrzyn, A. C., Barman, T. S., Günther, H. M., Hauschildt, P. H., and Exter, K. M., *Structure and spectra of irradiated secondaries in close binaries - A model calculation of the pre-cataclysmic variable UU Sagittae*, *submitted to Astronomy & Astrophysics* (2009a).

Wawrzyn, A. C., Günther, H. M., Barman, T. S., and Hauschildt, P. H. (2009b), Geometry of irradiated stars, in *American Institute of Physics Conference Series*, volume 1094 of *American Institute of Physics Conference Series*, pages 973–976.

Webbink, R. F., *Evolution of helium white dwarfs in close binaries*, *MNRAS* **171**, 555–568 (1975a).

Webbink, R. F., *PSR 1913 +/- 16: Endpoints of Speculation. A Critical Discussion of Possible Companions and Progenitors*, *Astronomy and Astrophysics* **41**, 1–+ (1975b).

Webbink, R. F. (1988), Late stages of close binary systems - clues to common envelope evolution., in *Colloquium on Critical Observations Versus Physical Models for Close Binary Systems, p. 403 - 446*, pages 403–446.

Webbink, R. F., *Common Envelope Evolution Redux*, *Short-Period Binary Stars: Observations, Analyses, and Results* , 233–+ (2008).

Weck, P., Stancil, P., and Kirby, K., *Theoretical study of the rovibrationally resolved transitions of CaH*, *Journal of Chemical Physics* **118** (2003).

Werner, K. and Heber, U., *On the evolutionary link between white dwarfs and central stars of planetary nebulae - NLTE analysis of PG 1144 + 005*, *Astronomy and Astrophysics* **247**, 476–486 (1991).

Wilson, R. E., *Accuracy and efficiency in the binary star reflection effect*, *Astrophysical Journal* **356**, 613–622 (1990).

Wilson, R. H., *Binary Stars and Cosmology*, *Irish Astronomical Journal* **12**, 206–+ (1976).

Wood, D. B., *A reflection model for eclipsing binary stars*, *MNRAS* **164**, 53–+ (1973).

Zahn, J.-P., *Tidal friction in close binary stars*, *Astronomy and Astrophysics* **57**, 383–394 (1977).

Zahn, J.-P., *Tidal evolution of close binary stars. I - Revisiting the theory of the equilibrium tide*, *Astronomy and Astrophysics* **220**, 112–116 (1989).

Acknowledgements

I would like to thank:

Figure D.1: 'thick=300' IDL Art (14 Jan 2009)